EXPERIMENTAL STUDY ON ETG TURBULENCE INDUCED PLASMA TRANSPORT IN LARGE VOLUME PLASMA DEVICE

By

PRABHAKAR SRIVASTAV
PHYS06201304006

Institute for Plasma Research, Gandhinagar

A thesis submitted to the
Board of studies in Physical Sciences

In partial fulfillment of requirements

for the Degree of

DOCTOR OF PHILOSOPHY

of

HOMI BHABHA NATIONAL INSTITUTE

March 2019

Homi Bhabha National Institute[1]

Recommendations of the Viva Voce Committee

As members of the Viva Voce Committee, we certify that we have read the dissertation prepared by Prabhakar Srivastav entitled "Experimental Study on ETG Turbulence Induced Plasma Transport in Large Volume Plasma Device" and recommend that it may be accepted as fulfilling the thesis requirement for the award of Degree of Doctor of Philosophy.

Chairman – Prof. S. Mukherjee	12.6.19
Guide – Dr. L. M. Awasthi	12.6.2019
Examiner - Dr. Som Kumar Sharma	12-6-2019
Member 1- Dr. Daniel Raju	12/6/19
Member 2- Dr. M. Bandhopadhyay	12.6.19.
Member 3- Dr. G. Ravi	12/06/2019
Member 4- Prof. Raghvendra Singh	12/06/2019
Technology Adviser – Mr. P. K. Srivastav	12/06/2019

Final approval and acceptance of this thesis is contingent upon the candidate's submission of the final copies of the thesis to HBNI.

I hereby certify that I have read this thesis prepared under my/~~our~~ direction and recommend that it may be accepted as fulfilling the thesis requirement.

Date: 12-06-2019

Place: IPR, Gandhinagar

Signature: 12.06.2019

Guide Dr L.M. Awasthi

[1] This page is to be included only for final submission after successful completion of viva voce.

STATEMENT BY AUTHOR

This dissertation has been submitted in partial fulfilment of requirements for an advanced degree at Homi Bhabha National Institute (HBNI) and is deposited in the Library to be made available to borrowers under rules of the HBNI.

Brief quotations from the dissertation are allowable without special permission, provided that accurate acknowledgement of source is made. Request for permission for extended quotation from or reproduction of this manuscript in whole or in part may be granted by the Competent Authority of HBNI when in his or her judgment the proposed use of the material is in the interest of scholarship. In all other instances, however, permission must be obtained from the author.

Prabhakar Srivastav

Prabhakar Srivastav

DECLARATION

I, hereby declare that the investigation presented in the thesis has been carried out by me. The work is original and has not been submitted earlier as a whole or in part for a degree/diploma at this or any other Institution/ University.

Prabhakar Srivastav

Prabhakar Srivastav

List of Publications arising from the thesis

Journal papers:

1. "Electron Temperature Gradient Turbulence Induced Energy Flux In The Large Volume Plasma Device", **Prabhakar Srivastav**, Rameswar Singh, L. M. Awasthi, A. K. Sanyasi, P. K. Srivastava, R. Sugandhi, and R. Singh, Phys. Plasmas **26**, 052303 (2019).
2. "Observation of Electromagnetic Fluctuation Induced Particle Transport In ETG Dominated Large Laboratory Plasma", **Prabhakar Srivastav**, Rameswar Singh, L. M. Awasthi, A. K. Sanyasi, P. K. Srivastava, R. Sugandhi, and R. Singh, Plasma Phys. Control. Fusion **61**, 055010 (2019).
3. "Electro-Mechanical Probe Positioning System for Large Volume Plasma Device", A. K. Sanyasi, R. Sugandhi**,** P. K. Srivastava, **Prabhakar Srivastav**, and L. M. Awasthi, Rev. Sci. Instrum. **89**, 055113 (2018).
4. "Observation of Radially Inward Turbulent Particle Flux in ETG Dominated Plasma of LVPD", **Prabhakar Srivastav**, Rameswar Singh, L. M. Awasthi, A. K. Sanyasi, P. K. Srivastava, R. Sugandhi, R. Singh, and P. K. Kaw, Phys. Plasmas **24**, 112115 (2017).
5. "Open Loop Control of Filament Heating Power Supply for Large Volume Plasma Device", R. Sugandhi, P. K. Srivastava, A. K. Sanyasi, **Prabhakar Srivastav**, L. M. Awasthi, and S. K. Mattoo**,** Fusion Engineering and Design **115**, 49 (2017).
6. "Process Automation System for Integration and Operation of Large Volume Plasma Device", R. Sugandhi, P. K. Srivastava, A. K, Sanyasi, **Prabhakar**

Srivastav, L. M. Awasthi, and S. K. Mattoo, Fusion Engineering and Design **112**, 804 (2016).

Conference papers:

1. "Demonstration of loss cone induced Quasi-Longitudinal (QL) Whistler in Large Laboratory Plasma of LVPD", A. K. Sanyasi, L. M. Awasthi, **Prabhakar Srivastav**, P. K. Srivastava, R. Sugandhi, S. K. Mattoo, D. Sharma, R. Singh, R. Paikaray, and P. K. Kaw, Proceedings of the EPS Conference on Plasma Physics **45**, P2.4008 (2017).
2. "Implementation of object oriented software engineering on LabVIEW graphical design framework for data acquisition in Large Volume Plasma Device", R. Sugandhi, P. K. Srivastava, **Prabhakar Srivastav**, A. K. Sanyasi, L. M. Awasthi, V. Parmar, K. Makadia, I. Patel, and S. Shah, Proceeding of the International Conference on Cloud Computing, Data Science & Engineering- Confluence **7**, 798-803 (2017).

Conferences:

International:

1. "Temperature Fluctuation Measurement in Electron Temperature Gradient (ETG) turbulent plasma of Large Volume Plasma Device (LVPD)", **Prabhakar Srivastav**, Rameswar Singh, L. M. Awasthi, A. K. Sanyasi, P. K. Srivastava, R. Sugandhi, and R. Singh, 2nd Asia-Pacific Conference on Plasma Physics (AAPPS-DPP2018), 12-17 Nov 2018 at Kanazawa, Japan. (**Oral presentation**).
2. "Exploring Role of Reynolds and Maxwell Stress towards shear layer formation in ETG turbulence dominated Large Laboratory Plasma", **Prabhakar Srivastav**,

Rameswar Singh, L. M. Awasthi, A. K. Sanyasi, P. K. Srivastava, R. Sugandhi, and R. Singh, 60th Annual Meeting of the APS Division of Plasma Physics, 5-9 Nov 2018 at Portland, Oregon, USA. (**Oral presentation**).

3. "Electron Temperature Gradient (ETG) Turbulence Induced Particle Transport in Finite Beta Laboratory Plasma", **Prabhakar Srivastav**, Rameswar Singh, L. M. Awasthi, A. K. Sanyasi, P. K. Srivastava, R. Sugandhi, and R. Singh, 47th European Physical Society Conference on Plasma Physics, 2-6 Jul 2018, at Prague, Czech Republic. (**Poster presentation**).
4. "Electron Temperature Gradient (ETG) Turbulence Induced Particle Transport Due to Finite Electromagnetic Fluctuations", **Prabhakar Srivastav**, Rameswar Singh, L. M. Awasthi , A. K. Sanyasi, P. K. Srivastava, R. Sugandhi, and R. Singh, 28th Symposium on Plasma Physics and Technology, 18-21 Jun 2018 at Czech Technical University in Prague, Czech Republic. (**Poster presentation**).
5. "Study of turbulent particle transport in ETG dominated plasma of LVPD", **Prabhakar Srivastav**, Rameswar Singh, L. M. Awasthi, A. K. Sanyasi, P. K. Srivastava, R. Sugandhi, R. Singh, and P. K. Kaw, International conference of Phenomena in ionized gases, 7-14 Jul 2017, Lisbon, Purtugal. (**Poster presentation**).
6. "Study of Fluctuation Induced Particle Flux in the background of ETG plasma in LVPD", **Prabhakar Srivastav**, L. M. Awasthi, A. K. Sanyasi, P. K. Srivastava, R. Jha, R. Singh, and P. K. Kaw, 10th Asia Plasma and Fusion Association (APFA) Conference, 14-18 Dec 2015 at Institute for Plasma Research, Gandhinagar, India. (**Poster presentation**).

National:

1. "Study of Particle Transport due to Electromagnetic Fluctuations in ETG Suitable Plasma of LVPD", **Prabhakar Srivastav**, Rameswar Singh, L. M. Awasthi, A. K. Sanyasi, P. K. Srivastava, R. Sugandhi, R. Singh and P. K. Kaw, 32nd National conference on Plasma Science and Technology, 7-10 Nov 2017 at Institute for Plasma Research, Gandhinagar, India. (**Poster presented and awarded with Best Poster award**).
2. "Measurement of Magnetic Fluctuation in LVPD "Comparison of result using numerical and inline integration technique", **Prabhakar Srivastav**, L. M. Awasthi, A. K. Sanyasi, P. K. Srivastava and R. Sugandhi, 5th PSSI-Plasma Scholar Colloquium, 27-28 Aug 2016 at Ravenshaw University, Cuttack, India. (**Poster presentation**).
3. "Temperature Fluctuation in LVPD: A Comparison of Triple and Two Probe Methods", **Prabhakar Srivastav**, A. K. Sanyasi, P. K. Srivastava, Nikunj Bhavsar, L. M. Awasthi, and R. Jha, 30th National conference on Plasma Science and Technology, 01-05 Dec 2015 at Saha Institute of Nuclear Physics, (SINP), Kolkata. (**Poster presentation**)
4. "Fluctuation Induced Particle Flux in the background of ETG plasma: Possible case of Intermittency" , **Prabhakar Srivastava**, L. M. Awasthi, A. K. Sanyasi, P. K. Srivastava, R. Jha, and S. K. Mattoo, 29th National conference on Plasma Science and Technology, 08-11 Dec 2014 at Mahatma Gandhi University, Kottayam, Kerala. (**Poster presentation**).

Others:

1. "Observation of Temperature Gradient Driven Electrostatic Ion Acoustic Instability in a Cross-field diffused Plasma", A. K. Sanyasi, **Prabhakar Srivastav**, P. K. Srivastava, R. Sugandhi and L.M. Awasthi (submitted in Phys. Plasmas).

Prabhakar Srivastav

Prabhakar Srivastav

Dedicated

To

My Parents

ACKNOWLEDGMENTS

It gives me immense pleasure to become a Ph.D. graduate from the Institute for Plasma Research, Gandhinagar, India. This thesis would not have been completed without the support and guidance of many people, whom I would like to thank from the bottom of my heart. I would like to thank each and everyone, who has been involved directly or indirectly in the research activities carried out as a part of my dissertation.

I sincerely thank Dr. Lalit Mohan Awasthi with a deep sense of gratitude for serving as thesis adviser and chief motivator during my Ph.D. His guidance has been instrumental in developing research and scientific skills throughout my Ph.D. He scrutinized all my experimental activities, starting from techniques used to report the observations. It has truly been a privilege to work with him.

Especially, I express my gratitude to my first Ph.D. doctoral committee chairman late Prof. P. K. Kaw for his great knowledge in plasma physics and defining the work for this thesis. I thank all the 'Doctoral Committee' members for following up the step by step progress made during my thesis work. I thank specially to my doctoral committee chairman Prof. S. Mukherjee for his active participation in motivating me to complete my thesis and for his constant support during this crucial phase of Ph.D. I am very much thankful to Prof. Raghvendra Singh for his kind support and help towards improving my understanding of this subject and for his support as a doctoral committee member for my thesis. I am grateful to Dr. Mainak Bandopadhyay for his useful support and for carrying out thorough scrutiny of my official applications and helping me through discussions on the way of presenting the work. I am equally thankful to Dr. D. Raju and Dr. G. Ravi, the other two doctoral

committee members for their help and guidance in reviewing my whole work, critical comments and their encouragement to learn additional techniques. I am greatly indebted to Dr. Rameswar Singh for his active participation in my thesis as a scientific collaborator. I learned many analytical and numerical techniques from him and had very fruitful physics discussions with him. I would also like to thank Mr. Pankaj Srivastav, as my technical advisor and for his constant help and guidance towards the development of many electronic systems for diagnostics used. I give my special thanks to Mr. A. K. Sanyasi for his help in experiments, for useful discussions and for his guidance all throughout these years. I sincerely thank Dr. Ritesh Sugandhi for his useful help in the successful operation of the newly procured data acquisition system.

I would also like to thank Prof. S. K. Mattoo, Prof. Y.C. Saxena, Prof. A. Sen and Prof. Amita Das for their special lectures. These lectures have introduced me to the advances of plasma physics covering the domains of theoretical, simulation and experimental realization of plasma physics. I am also grateful to other faculty members Dr. R. Ganesh, Dr. S. Sengupta, Dr. M. Ramasubramanian, Dr. R Goswami, Dr. M. Kundu, Dr. A. K. Chattopadhyay, Dr. V. P. Anitha, Dr. R. Kaur, and others, who have taught me basic plasma physics, experimental, computational techniques and other disciplines of plasma physics during the pre- Ph.D. course work. My special thanks to Dr. Pintu Bandyopadhyay, as a senior cum faculty for motivating me for completing the thesis work.

I would also like to thanks my colleagues Kalpesh, Daxesh, Nikunj, Puspendra, Yogesh, Riya, Gurpreet, Dharmik, from LVPD who have worked with me in short durations in LVPD Lab during my thesis work. I am thankful to Dr. Prince Alex for helping me in proofreading of my thesis. I sincerely thank Lavkesh, Umesh and Meenakshee for their active participation in clarifying my doubts regarding measurement techniques and physics interpretation. I also express my thanks to several other colleagues of LVPD and BETA laboratory who interacted and helped me either directly or indirectly.

I am greatly thankful to my seniors and friends in the hostel for their unconditional support and company. My warm regards to Aswin, Soumen, Sayak, Aditya, Sanat, Kshitish, Deepak, Ujjwal, Manjit, Gurudatt, Vikram Sagar, Satya, Rameswar, Sushil, Pravesh, Vikram Dharodi, Veda Prakash, Rana, Sandeep Rimza, Dushyant, Vara, Bhibhu, Neeraj, Roopendra, Chandrashekhar, Mangilal, Vidhi, Akanksha, Deepa, Meghraj, Harish, Samir, Narayan, Sonu, Debraj, Umesh, Ratan, Amit, Surabhi, Bhumika. I am especially grateful to Roopendra da, Deepa ma'am, Narayan Da and Umesh bhaiya for their helpful advice, discussion, and suggestions during my thesis tenure. I am very much thankful for my batchmates Alam, Atul, Jervis, Deepak, Chetan, Sagar, Sandeep, Harshita, Pallavi, and Meenakshee making this journey so fabulous and enjoyable. My special thanks go to Pallavi and Meenakshee to stand with me all the time. I heartily thanks to Sagar for being here as a close friend to listen to me. I am also very much thankful to all my juniors, Shivam, Avanish, Rupak, Arun, Neeraj, Garima, Srimanta, Devshree, Nidhi, Ayushi, Swapanali, Pawandeep, Satadal, Pradeep, Debrup, Sanjeev, Tanmay, and other scholars and TTPs for taking me to grow with you all together in IPR hostel, a delightful natural ambient inside the campus.

I am thankful to all in the Library, Computer center, Administration and very importantly all workshop members for their timely help and support in the time of my need.

I was fortunate to have Mr. Gaurav Jaiswal and Mr. Anand Pandey as big brothers and Mr. Lalit Shukla as a friend in Ahmedabad. I spent many happy moments with them and forgot my work stress during my stay with them.

Lastly but not least, I would like to thank extremely important people in my life i.e., my parents. I am greatly indebted to my parents, especially to my mother, for their unconditional love, support, motivation and everything in my life. They are the reason for whatever I am today. I would like to thank my younger sisters Priyamavada and Punita for their unconditional love and support.

CONTENTS

SYNOPSIS

I. Introduction

Plasma transport remains a core problem for magnetically confined fusion plasmas and hence allows uninterrupted attempts in the domain of theoretical, computational and experimental investigations for better understanding of the physical phenomena responsible for it. The small scale turbulence plays a major role in determining the global confinement properties of fusion plasmas [1-2]. The confinement properties degrade because of high outward particle and heat flux, observed to be several magnitudes higher than the classical or neoclassical flux. The anomalous flux is attributed to both electromagnetic and electrostatic turbulent fluctuations. Confined systems are naturally inhomogeneous which acts as source of free energy to drive the system and are unstable to slightest of the perturbations over a desperate range of scales, from electron, ion up to system scale [1,3-5].

Large scale perturbations are easy to probe in fusion devices and tremendous progress has been made on ion temperature gradient driven micro-turbulent mode and MHD modes but electron scale fluctuations, which follows scaling of $k_{\perp}\rho_e \leq 1$ are difficult to probe due to extremely small size. These fluctuations are considered as important source of heat loss during H-mode confinement [6-7]. Thus understanding physics of anomalous electron transport across the confining magnetic field assumes significance. While ultimately measurements in high temperature fusion plasmas in toroidal geometry must be undertaken, it is desirable to have a hierarchy of experiments for comparison with the goal of isolating important physical effects in the simplest possible geometry. Linear devices like Columbia Linear Machine (CLM) [8], Large Volume Plasma Device (LVPD) [9], and Q_T-Upgrade [10] have taken initiative in addressing some of the physical issues which are difficult to study in complex, high temperature, toroidal devices.

Electron Larmor radius scale fluctuations ($\rho_e \sim \mu m$) in the range of $k_{\perp} \rho_e \leq 1$ due to electron temperature gradient (ETG) in high magnetic field (~ 2 T) of tokamaks are hard to probe, though some progress has been made in National Spherical Torus Experiment (NSTX) [11] and Tore Supra [12]. However, detailed characterization of the turbulence in these devices for various plasma parameters and analyzing properties like correlations, wave number- frequency spectra is still unresolved. The basic plasma devices provide a simplified geometry, a good realization of turbulence and control of experimental parameters but they suffer from the very process by which plasma is produced in them. They produce moderate density plasma at lower magnetic fields and thereby bring the scale length of the ETG instability to the measureable limits of conventional probes. In LVPD, ETG suitable plasma is produced by configuring a highly transparent (~ 82%) variable aspect ratio, rectangular solenoid, named as Electron Energy Filter (EEF). It fits across the cross-section of LVPD in such a way that it divides the whole plasma into three regions of source, filter and target plasmas. The extremely localized perpendicular magnetic field of EEF removes energetic electrons all across the plasma in the target side and also enable a control over radial scale length of electron temperature gradient. The source region is where plasma is produced by filament heating, the EEF region, provides a strong transverse magnetic field over a radial extent of 100 cm (± 50 cm) to stop the energetic electrons traversing from source to target region and the target region is where plasma appears after diffusing through the filter magnetic field [13-14].

The ETG is a small scale turbulence associated with magnetized plasmas having a wavelength and frequency ordering ($k_\perp \rho_e \le 1 << k_\perp \rho_i, \Omega_i < \omega << \Omega_e$), where $k_\perp$ is the perpendicular wave vector, ρ_e, ρ_i are Larmor radii of electron and ion, respectively, and Ω_i, Ω_e and ω are the ion, electron gyro-frequencies and the mode frequency respectively. It's a fast growing mode having frequency and growth rate satisfying threshold condition for the mode, $\eta_e = L_{ne} / L_{Te,} > 2/3$ where $L_{ne}^{-1} = -(d \ln n_e / dx)$ and $L_{Te}^{-1} = -(d \ln T_e / dx)$ are the density and electron temperature gradient scale lengths. The observed instability in LVPD resides in lower hybrid range of frequency and has electromagnetic nature. Several signatures of the observed turbulence are found consistent with the theoretical predictions made for finite beta ETG modes [9, 15].

Fluctuations induced electrostatic (ES) particle flux is measured in ETG dominated plasma of LVPD and various statistical characteristics of it are explored [16]. We carried out detailed investigations on identifying the nature of electrostatic particle flux. The equilibrium electron density and temperature profiles are also measured which shows centrally peaked profiles. Unlike in tokamaks where the particle fuelling is done at the edge, the plasma source in LVPD comprises of heated tungsten filaments arranged in the periphery of a rectangle, coaxial to the device located at one axial end. Since the axial plasma diffusion is much faster than the transverse diffusion, the plasma formed at one axial end spreads rapidly along the field lines and hence the effective particle source can be thought to be axially elongated and slightly inside the radial edge. This implies, central density would build up only if there is an inward particle transport i.e., a particle pinch [17].

The electromagnetic fluctuations (EM) driven radial flux is still not completely explored. Its measurement has been reported from many devices, namely, the tokamak [18], the stellarator and reversed field pinch [19], etc. but despite this, particle transport due to electron scale EM fluctuations remain largely unaddressed. The streaming of charged particles parallel to the fluctuating magnetic field is considered as a powerful transport mechanism, particularly if field lines wander stochastically in space. The significance of magnetic fluctuations in the edge of various toroidal devices suggests that they are very significant in contributing to transport in different device configuration regimes like reversed field pinches, high beta tokamaks, and tokamaks in L-H transition [20]. In the past, direct measurement of magnetic fluctuation induced particle flux indeed has been reported but not much progress was made for the core plasma where the temperature is high due to the inability of measurement tools. In the recent time, Ding et al. [21], have demonstrated measurement of magnetic field fluctuation induced particle transport from the core plasma of Madison RFP device [22]. The reported particle transport exceeds the expected particle diffusion when ambipolarity exists but comes in good agreement with the expected values when ambipolarity is not there. However, Stoneking et al. [23], Rembel et al. [22], and Shen et al. [24] have reported that particle loss induced by magnetic field fluctuations is ambipolar in the edge plasma.

In high beta plasma of LVPD, the magnetic field fluctuations couples with the ETG mode instability to form what is dubbed as the whistler-ETG mode. In magnetized plasma, the EM flux in ETG background is expected to be zero as per the conventional ETG mode theory where it is assumed that the electron current fluctuation $\delta J_{\parallel,e}$ is the total current fluctuation, $\delta J_{\parallel}$. Then the radial electron particle flux can be written as $\Gamma_{em} = \frac{1}{eB} < \delta J_{\parallel e} \delta B_x > = 0$, where $\delta J_{\parallel e}$ and δB_x are parallel electron current and magnetic field fluctuations. However, we do observe a small but finite EM flux in the LVPD. Obviously, this means that the assumption $\delta J_{\parallel e} = \delta J_{\parallel}$ (where $\delta J_{\parallel}$ is the total parallel current) is broken in reality and consequence of leads to finite flux. This provides a detailed measurement of EM particle flux across the radius of the LVPD for the first time and provides a general theory of the EM particle flux in ETG turbulence in a straight homogeneous magnetic geometry which explains well the experimental observations. A finite EM radial flux is shown to result from the sluggish and passive parallel ion velocity fluctuations resulting from the parallel force experienced by ions due to ETG fluctuations.

Lastly, in the presence of ETG turbulence, thermal heat flux is measured. Specially designed triple Langmuir probe for real-time measurement of temperature fluctuations in pulsed plasma of LVPD is developed [25-26]. The estimated thermal flux is compared with the numerically obtained values, by using the formulation derived for slab ETG turbulence. A theoretical expression is formulated for heat flux due to ETG scale fluctuation to verify our experimental measurement of heat flux. The experimental heat flux is calculated with correlated measurement of potential and electron temperature fluctuation present in experiments. Since the observed ETG fluctuations are characterized as ES and EM in nature and it leads to respective heat flux generation. So, theoretical estimates is provided for both, ES and EM fluctuations. The turbulent heat flux can be written as $q_{cond} = n_o < \tilde{T}_e \tilde{v}_r >= -\sum_k \frac{k_y}{B} n_o |\tilde{T}_{e,k}||\tilde{\phi}_k| sin\theta_{T_e\phi}$, where $\theta_{T_e\phi} = \theta_{T_e} - \theta_{\phi}$. This expression suggests that the heat flux depends on the level of fluctuations and phase relation between temperature and potential fluctuations as is originated from finite temperature and potential fluctuations in ETG turbulence dominated plasma. The role of temperature fluctuations in the measurement of conductive flux is estimated. The phase angle between temperature and potential fluctuations also exhibits a close agreement with theoretical predictions obtained from ETG model equations. We have successfully presented that in ETG dominated LVPD plasma, even though, observed particle flux is negative and which leads to negative convective heat flux ($T_e < \tilde{n} \tilde{v}_r >$) but conductive heat flux ($n_o < \tilde{T}_e \tilde{v}_r >$) remains positive and is comparatively higher than the convective heat flux. This supports thermodynamically, entropy production which is positive definite [27]. The net flux observed in LVPD due to ETG induced turbulence is outward.

Based upon the above outline, this thesis reports on the experimental demonstration of ETG turbulence induced particle and thermal fluxes in a laboratory device. The motivation for this work comes from the background of microturbulence induced anomalous transport problem encountered in fusion plasmas. The contents of the thesis are summarized in the following text.

II. Contents of the thesis

Chapter 2: Experimental setup and diagnostic system

In this chapter, the emphasis is on the developmental work carried out towards the automation of device, on experimental tools and diagnostics development for carrying out investigations on ETG induced plasma transport. The major contributions are namely, the development of (1) triple Langmuir probe diagnostics and its floating power supply, (2) developing computer-based control of linear probe drive for better spatial resolution, (3) establishment of PXI base data acquisition system with better bit resolution, (4) development of specially designed probe diagnostics for particle, energy and parallel electron and ion current measurements besides developing several MATLAB routines for carrying out data analysis. Microwave interferometry diagnostic for chord average density measurements is another important development carried out in LVPD during this time. It works as a residential diagnostics in the device for depicting the state of wall conditioning after each opening and provides on hand information on plasma density. While revisiting the performance of Electron Energy Filter (EEF) and identification of ETG, it was observed that energetic electrons emitted from filamentary source remain constrained within the source and the EEF region. The EEF divides LVPD plasma into three regions of source, EEF and target plasmas. It exerts not only control on the electron temperature because of the preferential transport of cold electrons in the target region but also introduces significant gradient in electron temperature by adjusting current density along the length of EEF. The plasma in the source and target region for different EEF activation currents is produced. Various equilibrium plasma profiles suitable for carrying out ETG study by varying extent of charging length of EEF cross-section are established. A brief description on LVPD device including its auxiliary systems namely, pumping system, magnet coil system, plasma source, power supply, and diagnostic system is given below.

- The LVPD is a double walled, water-cooled cylindrical vacuum chamber**.** It gets evacuated to a base pressure of ~1 × 10^{-6} mbar. The radial and axial confinement are provided by ten garlanded magnet coils and by a pair of cusped SS304 plates mounted at two extreme axial ends of the device. The plasma is produced using a large multi-filamentary plasma source, called Low Energy Electron Source (LEES). The LEES contains hairpin shaped Tungsten filaments, mounted symmetrically on a rectangular periphery (130 cm × 90 cm) on to the filament holder cusped SS304 plate. The filament and discharge power supplies are used in combination for producing pulsed Argon plasma in LVPD.
- The plasma in most of the linear devices is contaminated by the presence of ionizing hot and non-thermal electrons emitted by the hot filaments. Their simultaneous presence confuses the interpretation of the exciting turbulence, as each one of them could be independent drivers for the excitation of events. In order to scavenge the energetic electrons, a varying aspect ratio solenoid of rectangular cross-section with maximum size (190 cm × 4 cm) at the axis of LVPD and minimum size of (4 cm × 4 cm) near the walls is configured. It produces a uniform pulsed transverse magnetic field of 105 G when fully energized by a current of 2 kA. It comprises of 19 identical parallel resistive paths distributed over the cross-section of LVPD.
- The cylindrical, compensated Langmuir probes are used to measure plasma density (n_0), electron temperature (T_e), and floating potential (ϕ_f) and their fluctuations. The center-tapped emissive probe is used to determine the plasma potential (ϕ_p). The diamagnetic flux and magnetic fluctuations are measured by bifilar B- dot probe. The real-time temperature fluctuations are obtained by using a specially designed compensated triple probe.
- A clear signature of scavenging of energetic electrons is observed from I-V characteristic of Langmuir probe for EEF present and absent plasma scenarios. All experimental investigations right from revisiting the ETG turbulence to the measurement of particle and energy fluxes are carried out in the target region, which is free of energetic electrons.

Chapter 3: Experimental study of particle transport due to electrostatic (ES) fluctuations

In this chapter, we present results on the investigation of particle transport due to ETG turbulence, estimated by correlated fluctuations in density and potential. Experimentally obtained density-potential cross-correlation, power spectra, and frequency-wavenumber ordering confirm that the observed turbulence is driven by electron temperature gradient. A brief summary of this chapter is described as follows.

- Experimentally observed fluctuation driven ES particle flux is found negative i.e., directed radially inward and is of the order of $\Gamma_{es} \sim -10^{18} m^{-2} s^{-1}$. We have correlated it with particle pinch problem of tokamaks. The plasma density maximizes in the core region when EEF is ON which is not the case when EEF is OFF thus indicating that the inward particle flux resulting from ETG fluctuations plays a significant role in it. Net particle flux is finite and it results as the phase difference, $\theta_{\delta n, \delta\phi}$, deviates from 180° for ETG dominated plasma.
- The observed cross phase angle and flux have been compared with theoretical estimates and an agreement within 20% accuracy between them are found radially.

Chapter 4: Experimental study of Particle Transport due to electromagnetic (EM) fluctuations

In this chapter, in finite plasma beta of LVPD, EM particle flux is measured with specially designed array of probes. It contains a pair of directional probes for parallel electron and ion current and a 3-axis B-dot probe for the magnetic fluctuation measurements. We found that EM flux has non-ambipolar nature. In contrast to prediction for fusion plasma where EM flux is predicted as zero, LVPD exhibits a finite value in open field lines scenario. A brief summary of this chapter is described as follows.

- A quasi-linear theory is proposed to explain the observed flux which convinces that the non-ambipolarity is due to divergence of Maxwell stress $\frac{\partial}{\partial x} < \delta B_x \delta B_y >$ and another correlation$< \delta B_y \frac{\partial}{\partial z} \delta B_z >$. The pseudo ion flux similar to ion flux in morphology had the ions been magnetized. This is because the parallel ion dynamics is little affected by the degree of magnetization of ions. The physical electromagnetic ion flux in ETG turbulence is zero because no radial ion drift fluctuation due to un-magnetization of ions. Then the overall quasi-neutrality is maintained by the parallel fluxes.

- In LVPD, the quasi-linear estimates of the EM pseudo ion flux due to parallel ion current fluctuation compares well with the measured flux and hence the role of sluggish ion motion assumes significance.

Chapter 5: Experimental study of total turbulent heat transport

This chapter discusses heat flux measurement originated from finite temperature, potential and density fluctuations in ETG turbulence dominated plasma. Both conductive and convective fluxes are considered for estimating total heat flux. A specially designed floating TLP is developed for this purpose. The summary of this chapter is described as follows.

- The TLP assembly is capable of measuring simultaneously electron temperature, floating potential and plasma density fluctuations. The heat flux is measured and is found positive, opposite to the observed particle flux.
- Using ETG model equations, theoretical expression is derived for the estimation of heat flux due to ES and EM fluctuations. The phase angle between electron temperature and potential fluctuations shows good agreement with the theoretical predictions derived from ETG model equations.

Chapter 6: Conclusion and future scope

In summary, we have successfully demonstrated the role of ETG turbulence in particle and heat transport induced by correlated, small scale ($k_{\perp}\rho_e \leq 1$) fluctuations in plasma density, potential and electron temperature. The major conclusions of the thesis are as follows.

- ETG scale fluctuations are revisited and ES fluctuation induced particle flux was measured. Noticeably, we observed radially inward particle flux. It was found consistent with theoretical predications when role of ion non-adiabatic response in ETG model equations is considered. Even, phase angle between the density and potential fluctuations agrees well with theory. In LVPD, finite plasma beta

($\beta = nT_e/(B^2/2\mu_o)$, density and potential fluctuations are strongly coupled. Hence role of magnetic fluctuations in particle flux estimations is considered. Specially designed probe array is configured for the measurement of EM flux. A new theoretical model for W-ETG by taking into account the sluggish motion of ions in parallel direction is developed. The observed EM particle flux is found in agreement with the estimated flux.

- For energy flux measurement, high frequency, floating TLP diagnostics is developed for real time measurement of T_e, ϕ_f, ϕ_p and their respective fluctuations. The measured heat flux is found radially outward satisfying theoretical predications from ETG model equations.
- Future work primarily aimed for understanding features like identifying threshold of ETG turbulence in laboratory plasma, generation of long lived structure and how ETG turbulence saturates? Further, it can be expanded to measurement of long scale modes namely, zonal field (small scale dynamo or zonal current), ES streamer, magnetic streamer, zonal flows and role of magnetic shear in nonlinear structures in background of short scale ETG turbulence in LVPD plasma.

References

[1] E. J. Doyle *et al.*, "Chapter 2: Plasma confinement and transport", *Nucl. Fusion*, vol. 47, no. 6, pp. S18–S127, 2007.

[2] K. H. Burrell *et al.*, "Confinement physics of H-mode discharges in DIII-D", *Plasma Phys. Control. Fusion*, vol. 31, no. 10, pp. 1649–1664, 1989.

[3] J. W. Connor, "Transport in tokamaks: Theoretical models and comparison with experimental results", *Plasma Phys. Control. Fusion*, vol. 37, no. 3, pp. 119–133, 1995.

[4] S. M. Kaye *et al.*, "Confinement and local transport in the National Spherical Torus Experiment (NSTX)", *Nucl. Fusion*, vol. 47, no. 7, pp. 499–509, 2007.

[5] W. Horton, B. Hu, J. Q. Dong, and P. Zhu, "Turbulent electron thermal transport in tokamaks", *New J. Phys.*, vol. 5, pp. 14.1-14.34, 2003.

[6] J. D. Callen *et al.*, “Analysis of pedestal plasma transport”, *Nucl. Fusion*, vol. 50, no. 6, pp. 064004, 2010.

[7] F. Castejon et al., “3D effect on transport and plasma control in the TJ-II stellarator”, *Nucl. Fusion*, vol. 57, no. 10, pp. 102022, 2017.

[8] X. Wei, V. Sokolov, and A. K. Sen, “Experimental production and identification of electron temperature gradient modes”, *Phys. Plasmas*, vol. 17, no. 4, pp. 1–6, 2010.

[9] S. K. Mattoo, S. K. Singh, L. M. Awasthi, R. Singh, and P. K. Kaw, “Experimental observation of electron-temperature-gradient turbulence in a laboratory plasma”, *Phys. Rev. Lett.*, vol. 108, no. 25, pp. 1–5, 2012.

[10] C. Moon, T. Kaneko, and R. Hatakeyama, “Dynamics of nonlinear coupling between electron-temperature-gradient mode and drift-wave mode in linear magnetized plasmas”, *Phys. Rev. Lett.*, vol. 111, no. 11, pp. 1–4, 2013.

[11] E. Mazzucato *et al.*, “Study of turbulent fluctuations driven by the electron temperature gradient in the National spherical torus experiment”, *Nucl. Fusion*, vol. 49, no. 5, p. 055001, 2009.

[12] W. Horton *et al.*, “Temperature gradient driven electron transport in NSTX and Tore Supra”, *Nucl. Fusion*, vol. 45, no. 8, pp. 976–985, 2005

[13] S. K. Mattoo *et al.*, “A large volume plasma device”, *Rev. Sci. Instrum.*, vol. 72, no. 10, pp. 3864-3872, 2001.

[14] S. K. Singh *et al.*, “Performance of large electron energy filter in large volume plasma device”, *Rev. Sci. Instrum.*, vol. 85, no. 3, pp. 033507, 2014.

[15] S. K. Singh, L. M. Awasthi, R. Singh, P. K. Kaw, R. Jha, and S. K. Mattoo, “Theory of coupled whistler-electron temperature gradient mode in high beta plasma: Application to linear plasma device”, *Phys. Plasmas*, vol. 18, no. 10, pp.

102109, 2011.

[16] P. Srivastav *et al.*, “Observation of radially inward turbulent particle flux in ETG dominated plasma of LVPD”, *Phys. Plasmas*, vol. 24, no. 11, pp. 112115, 2017.

[17] X. Garbet *et al.*, “Physics of transport in tokamaks”, *Plasma Phys. Control. Fusion*, vol. 46, no. 12 B, pp. B557–B574, 2004.

[18] B. A. Carreras *et al.*, “Transport effects induced by resistive ballooning modes and comparison with high-βp ISX-B tokamak confinement”, *Phys. Rev. Lett.*, vol. 50, no. 7, pp. 503–506, 1983.

[19] H. Hutchinson, M. Malacarne, P. Noonan, and D. Brotherton-Ratcliffe, “The structure of magnetic fluctuations in the HBTX-1A reversed field pinch”, *Nucl. Fusion*, vol. 24, no. 1, pp. 59, 1984.

[20] K. H. Burrell *et al.*, “Physics of the L-mode to H-mode transition in tokamaks”, *Plasma Phys. Control. Fusion*, vol. 34, no. 13, pp. 1859-1869, 1992.

[21] W. X. Ding *et al.*, “Nonambipolar magnetic-fluctuation-induced particle transport and plasma flow in the MST reversed-field pinch”, *Phys. Rev. Lett.*, vol. 99, no. 5, pp. 1–4, 2007.

[22] T. D. Rempel *et al.*, “Turbulent transport in the Madison Symmetric Torus reversed-field pinch”, *Phys. Fluids B*, vol. 4, no. 7, pp. 2136–2141, 1992.

[23] M. R. Stoneking, “Particle transport due to magnetic fluctuations”, *Phys. Rev. Lett.*, vol. 73, no. 4, pp. 549–553, 1994.

[24] W. Shen, R. N. Dexter, S. C. Prager, and and S. C. P. W. Shen, R. N. Dexter, “Current-Density Fluctuations and Ambipolarity of Transport”, *Phys. Rev. Lett.*, vol. 68, no. 9, pp. 1319-1322, 1992.

[25] S. L. Chen and T. Sekiguchi, “Instantaneous direct-display system of plasma parameters by means of triple probe”, *J. Appl. Phys.*, vol. 36, no. 8, pp. 2363-

2375, 1965.

[26] V. Sokolov and A. K. Sen, “Measurements of electron thermal transport due to electron temperature gradient modes in a basic experiment”, *Phys. Rev. Lett.*, vol. 107, no. 15, pp. 1-4, 2011.

[27] H. Sugama, M. Okamoto, W. Horton, and M. Wakatani, “Transport processes and entropy production in toroidal plasmas with gyrokinetic electromagnetic turbulence”, *Phys. Plasmas*, vol. 3, no. 6, pp. 2379-2394, 1996.

LIST OF FIGURES

LIST OF TABLES

Chapter 1
Introduction

The thesis provides the experimental observation on turbulent plasma transport due to fluctuations in the presence of electron temperature gradient (ETG) turbulence in a straight magnetic field scenario of Large Volume Plasma Device (LVPD). The thesis includes major developmental and experimental efforts to quantify the particle and heat losses induced by ETG turbulence. A theoretical study is also provided to validate the experimental observations. In this chapter, we present the motivation for this study, followed by a brief description of plasma transport which highlights the content of the thesis.

1.1. Overview and motivation

Plasma, commonly called as the fourth state of matter, deals with the complex interaction of many charged particles with external or self-generated electromagnetic fields. This has implications in a wide variety of applications, ranging, from advanced lighting devices and surface treatments for semiconductor applications to a larger role of taming nuclear fusion as an energy source for humanity. Among the various techniques of achieving nuclear fusion in laboratory plasma, magnetic confinement stands most popular as on today. This scheme makes use of a strong magnetic field to confine hot nuclei of hydrogen isotope to achieve condition for fusion [1]. The condition for sustainable fusion reactions is mostly determined by the plasma density, temperature and confinement time and has dependency on plasma transport.

Plasma transport determines the mean profile and the confinement properties of the system. In magnetic confinement fusion research, for example in tokamaks, one of the most important and burning issues is an improvement of energy and particle confinement time for controlled thermonuclear reaction [2,3]. The confinement properties degrade because of high outward particle and heat flux which is observed to be several magnitudes higher than the classical or neoclassical transport predication which depends on the collisionality and magnetic field configuration. Plasma transport continues to remain a core problem for magnetically confined fusion plasmas [3–6] and hence motivates continued efforts in the domain of theoretical, computational and experimental investigations for a better understanding of the physical phenomena responsible for it. A new type of plasma transport, named as turbulent transport is predicated to understand the experimentally observed plasma losses which are due to the presence of fluctuations excited in the plasma system.

Turbulent transport is a ubiquitous phenomenon prevalent in a laboratory, space and astrophysical systems [2,7–9]. This anomalous flux is attributed to turbulent fluctuations due to various instabilities inherent in the system. Confined systems are naturally inhomogeneous which act as a source of free energy to drive the system and are unstable to slightest of the perturbations over a disparate range of scales, from electron, ion up to system scale. These fluctuations can have electrostatic and or electromagnetic nature [10–17] which contributes to the electrostatic flux, $\Gamma_{es} = <\delta n_e \delta v_x>$) and electromagnetic particle flux, $<\Gamma_{em} = 1/qB <\delta J_{||}, q\delta B_x>$, where δn_e , δv_x ,$\delta J_{||q}$, δB_x are the fluctuations in density, velocity, parallel currents and radial magnetic field, respectively and q represents the charge. The net turbulent particle flux is thus made up from the sum of electrostatic and electromagnetic fluctuations,

$\Gamma = \Gamma_{es}^{q} + \Gamma_{em}^{q}$, where Γ_{es} and Γ_{em} represents the electrostatic and electromagnetic flux components.

Large scale perturbations (order of ion larmor radius) are easy to probe in fusion devices and tremendous progress has been made on ion temperature gradient driven micro-turbulent mode and MHD modes. The electron Larmor radius scale fluctuations ($\rho_e \sim \mu\text{m}$) in the range of $k_\perp \rho_e \sim 1$ due to electron temperature gradient (ETG) in high magnetic field ($\sim 2\ \text{T}$) of tokamaks are hard to probe despite of progress made in National Spherical Torus Experiment (NSTX) [18,19] and Tore Supra [20] machines. The ETG is a small scale turbulence associated with magnetized plasmas having a wavelength and frequency ordering ($k_\perp \rho_e \le 1 << k_\perp \rho_i, \Omega_i < \omega << \Omega_e$), where $k_\perp$ is the perpendicular wave vector, ρ_e, ρ_i are Larmor radii of electron and ion, respectively, and Ω_{ci}, Ω_{ce}, ω are the ion, electron gyro-frequencies and the mode frequency respectively. It's a fast growing mode having frequency and growth rate defined as $\omega_r = (1/2)[\eta_e \omega_{*e} k_z^2 c_e^2 / \tau_e]^{1/3}$ and $\gamma_{ETG} = (\sqrt{3}/2)[\eta_e \omega_{*e} k_z^2 c_e^2 / \tau_e]^{1/3}$ [21,22], where k_z is the parallel wave vector of the mode, c_e is the thermal velocity of electrons, $\omega_{*e} = k_\theta v_{*e} = k_\theta (\rho_e c_e / L_{ne})$ is the electron diamagnetic drift frequency and satisfy threshold condition for the mode, $\eta_e = L_{ne} / L_{Te,} > 2/3$ where $L_{ne}^{-1} = -(d \ln n_e / dx)$ and $L_{Te}^{-1} = -(d \ln T_e / dx)$ are the density and electron temperature gradient scale lengths. While ultimately measurements in high temperature fusion plasmas in toroidal geometry must be undertaken, it is desirable to have a hierarchy of experiments for comparison with the goal of isolating important physical effects in simplest possible geometry devices. Linear devices like Columbia Linear Machine (CLM) [23], Large Volume Plasma Device (LVPD) [24], and Q_T-Upgrade [25] have taken initiative in addressing some of the physical issues which are difficult to study in complex, high temperature, toroidal devices. The advantage these devices carry unlike their high temperature counterparts is their ease of operation and control of parameters. It is now observed that it is possible to scale up the size of the ETG mode in a simpler setting of straight magnetic field line geometry. Recently, ETG turbulence was established in the target region of Large Volume Plasma Device with electron gyro scale length typically of the order of few millimetres by utilizing the cross field diffusion across the strong magnetic field. Large Volume Plasma Device (LVPD) is a cylindrical device (length = 3 m and diameter = 2 m) produces pulse filamentary plasma for basic wave studies [26].

To study ETG turbulence phenomena in LVPD, a 2 m diameter electron energy filter (EEF) is conceptualized [27]. The EEF is a varying aspect ratio rectangular solenoid of extended radial extent and limited axial extent. The EEF is configured to secure the following objectives namely, (1) removing the presence of remnant primary ionizing energetic electrons and the non-thermal electrons, (2) introducing a radial gradient in plasma electron temperature without greatly affecting the radial profile of plasma density, and (3) providing a control on the scale length of gradient in electron temperature.

Introduction of EEF divides LVPD plasma into three distinct regions of Source, EEF and Target plasmas. Source region covers the plasma volume between the cathode and the first surface of EEF, the EEF region covers the region between its two surfaces while the target plasma region extends from EEF second surface to the end plate. The EEF region provides a strong transverse magnetic field over a radial extent of 100 cm (± 50 cm) to stop the energetic electrons traversing from source to target region. The target plasma has no detectable energetic electrons and the radial gradients in the electron temperature can be established with scale length between 50 and 600 cm by controlling EEF magnetic field. Observations reveal that the role of the EEF magnetic field is manifested by the energy dependence of transverse electron transport and enhanced transport caused by the plasma turbulence in the EEF.

Unambiguous, identification of ETG turbulence is successfully demonstrated in the core region of target plasma ($x \leq 50$ cm and for z = (20 - 150) cm from the second surface of EEF) [24,28]. The work on ETG turbulence suggests two possible responsible mechanisms for slab configuration for different plasma beta regimes. In low plasma beta condition viz., $\beta \leq 0.1$ the slab ETG mode is primarily driven by parallel compression of electron motion along the magnetic field. The compression effect in electron parallel motion will generate temperature and density perturbations. The density perturbation is out of phase to potential perturbation via ion Boltzmann shielding effect. The potential perturbation creates $E \times B$ drift, which brings cold electrons in a compressed region and thus lowers the pressure. The lower pressure attracts more electrons, further increasing the compression. This positive feedback loop leads to instability. While in high beta plasma, $\beta \geq 0.1$, ETG mode becomes unstable similar to toroidal ETG by whistler wave and coupling of it to ETG play an important role in making mode unstable [22].

Fluctuations induced electrostatic particle flux is measured and its comparison is made. The radial electrostatic flux appears due to the correlation between density, $\tilde{n}$ and perpendicular electric field fluctuations, $\tilde{E}_{\perp}$ i.e., $\Gamma_{es} = < \tilde{n}\tilde{E}_{\perp} > /B$. It is observed that electrostatic turbulent particle flux is radially inward in the core region of target plasma and has purely thermo-diffusive nature. It is also found that the thermo-dynamical entropy of the system is reduced due to the inward particle flux. This suggests that the heat flux and other dissipations together must overcome the entropy of the system. The equilibrium electron density and temperature profiles shows centrally peaked profiles. How? Unlike in tokamaks where the particle fuelling is done at the edge, the filamentary plasma source in LVPD, located at its one axial end has filaments arranged in the periphery of a rectangle, coaxial to the device. This implies that central density would build up only if there is an inward particle transport i.e., a particle pinch.

In the finite beta plasma of LVPD, finite magnetic fluctuations are observed. The radial electromagnetic flux is measured and found finite in straight field lines of LVPD, contrary to the predicted zero value of flux by ETG model equations for toroidal plasma. The EM flux develops from the correlation between parallel current, $\delta J_{\parallel,q}$ of charge species, $q \approx e, i$ and radial magnetic field fluctuation, δB_x. Available literature suggests that significant advancement in developing an understanding is achieved as far as electrostatic flux contribution is concerned [10–12,29,30] but the electromagnetic fluctuations driven radial flux is still not completely explored. Although, the electromagnetic particle flux has been reported from many devices, namely, the tokamaks [31,32] , the stellerator [16] and reversed field pinch [33–35] etc. but despite this, electromagnetic electron scale fluctuations induced particle transport remain largely unaddressed. While the effect of the electromagnetic fluctuations on particle transport still remain unaddressed, the streaming of charged particles parallel to fluctuating magnetic field is considered as a powerful transport mechanism, particularly if field lines wander stochastically in space [36,37] . The significance of magnetic fluctuations in the edge of various toroidal devices suggest that they are very significant in contributing to transport in different device configuration regimes like reversed field pinches [38] , high beta tokamaks [39], and tokamaks in L-H transition [40].

The magnetic fluctuations can be driven by different instabilities present in the plasma due to inhomogeneity in plasma parameters. Basic understanding of magnetic fluctuation induced particle transport processes attains great interest and becomes potentially critical to plasma density control and understanding fast particle losses in future plasmas like ITER. These energetic particles are present in magnetic fusion devices due to external plasma heating and eventually due to fusion born α- particles. It is necessary that these superthermal particles are well confined while they transfer their energy to the background plasma [41]. As reported, magnetic fluctuations induced plasma transport can be large even if the fluctuation amplitude is extremely small [35]. The excited magnetic field fluctuations in high-temperature machines have their origin lies with instabilities excited during non-inductive heating and current drive by energetic particles. Even, they get excited by global tearing instabilities that often underlie the sawtooth oscillation associated with magnetic reconnection and lead to plasma relaxation. The stochastic magnetic field is deliberately imposed in tokamak plasmas by using external coils to mitigate the edge-localized modes excited electromagnetic particle flux [42]. However, transport due to magnetic fluctuations has been mainly studied indirectly by measuring runaway electron flux to a limiter. Such experiments are useful for probing the magnetic fluctuations but do not provide a local measurement of particle transport resulting from the magnetic field. In the past, direct measurement of magnetic fluctuation induced particle flux indeed has been reported but has been limited to the edge region of fusion devices using probes [34,35]. However, not much progress was made for the core plasma where the temperature is high due to the inability of measurement tools.

In recent time, Ding et al. [33], have demonstrated measurement of magnetic field fluctuation induced particle transport from the core plasma of Madison RFP device. The presence of stochastic magnetic field supports non-ambipolar transport since electrons stream rapidly along field lines. In such a situation, they report that measured electron flux is responsible for the rapid particle transport and it modifies the equilibrium density [17]. They also reported that the measured particle transport exceeds the expected particle diffusion when ambipolarity is maintained because of the slowing down of electron to ion diffusion but it agrees well with the expected values when ambipolarity is absent. In a theoretical sense, non-ambipolarity can exist only when it is balanced by an opposing non-ambipolar flux in order to maintain plasma quasi-neutrality. However, Stoneking et al. [35], Rempel et al. [34], and Shen et al. [42] have reported that particle loss induced by magnetic field fluctuations remains ambipolar in the edge plasma.

In the finite plasma beta (β ~ 0.01 - 0.4) of LVPD, the magnetic field fluctuations couple with the ETG mode instability to form what is dubbed as a whistler-ETG mode. In LVPD, Singh et al. [22], have shown that when electromagnetic effects are included, the ion-electron interchange symmetry breaks down. This is because the magnetic perturbations alter the electron dynamics; as a result, the parallel dynamics of ions and electron are no longer symmetric. The coupling of Whistler and ETG mode becomes important when the beta of plasma is high (i.e., β ~0.01-0.4) but W-ETG mode again becomes unstable like ETG only when the electron temperature gradient crosses a threshold value, $\eta_e > 2/3$. As mentioned before for magnetized plasma, the electromagnetic flux in ETG background is expected to be zero as per the conventional ETG mode theory. The assumption was that the electron current fluctuation $\delta J_{\parallel,e}$ only contributes to the total current fluctuation, $\delta J_{\parallel}$. The radial electron particle flux thus can be written as [43],

$$\Gamma_{em} = \frac{1}{eB} < \delta J_{\parallel e} \delta B_x > = \frac{1}{eB} < \delta J_{\parallel} \delta B_r > = \frac{1}{eB} < \nabla_{\perp}^2 A_{\parallel} \frac{\partial}{\partial y} A_{\parallel} >$$
$$= Real(\sum_{\vec{k}} i k_{\perp}^2 \, k_y \mid A_{\parallel} \mid^2) = 0 \tag{1}$$

where, k_y, $k_{\perp}$ are wave vectors in radial and perpendicular directions $and\ A_{\parallel}$ is vector potential respectively. Clearly, this vanishes because the summand is odd in poloidal wave number, k_y.

Noticeably, we do observe finite electromagnetic flux in LVPD. Obviously, this means that the assumption $\delta J_{\parallel e} = \delta J_{\parallel}$ is broken in reality and consequently leads to a finite flux. This is important to note here that detailed measurement of electromagnetic particle flux across the radius of the LVPD has been undertaken for the first time. Also, a general theory of the electromagnetic particle flux in ETG turbulence in a straight homogeneous magnetic geometry is developed to explain experimental observations.

A finite electromagnetic radial flux is shown to result from the sluggish and passive parallel ion velocity fluctuations resulting from the parallel force experienced by ions due to ETG fluctuations. The motion is sluggish because the ion velocity scales as $\frac{m_e}{m_i} v_{\parallel e}$ and passive because this small mass ratio for Argon plasma barely effect the linear features of the ETG mode. Lack of magnetization of ions fails to produce a fluctuating radial drift of ions, which leads to no turbulent ion flux thus making the flux non-ambipolar. The electron flux is made of pieces resulting from parallel ion current fluctuations and magnetic stresses. The piece of flux resulting from ion current fluctuations is exactly similar to electromagnetic ion flux had the ions been magnetized like the ITG turbulence. Due to this morphological similarity, it is dubbed here as pseudo ion flux. Quasilinear estimate is obtained for the pseudo ion flux which agrees well with the experimental measurement.

In high confinement (H-mode) scenario, due to the strong $E \times B$ shearing in the internal transport barrier, ion heat transport becomes neoclassical. However electron thermal transport still remain anomalous because the $E \times B$ shearing is probably still not strong enough to suppress the electron scale turbulence [44]. This is the reason why focus has been shifted to the understanding of physics of anomalous electron heat transport across the confining magnetic field, envisaging its implications for ITER and advanced tokamak discharges [2,45,46].

Extensive work has been reported in the past on measurements of micro-instabilities driven turbulence because of their possible role in causing energy transport in fusion devices [5,47–50]. Outcome from these investigations suggest that transport due to the Electron Temperature Gradient (ETG) driven turbulence, which is considered presently a major source of anomalous electron heat transport in fusion devices is still not properly understood. In the presence of ETG turbulence, total energy flux is measured and electron thermal heat conductivity is derived from the temperature fluctuations. For this purpose, a specially designed triple Langmuir probe for real-time measurement of temperature fluctuations in pulsed plasma of LVPD is developed. The estimated thermal flux is compared with the numerically obtained values from the derived formulation for slab ETG turbulence.

1.2 Objective and outline of the thesis

In Large Volume Plasma Device (LVPD), the plasma is dressed up by making use of a large electron energy filter (EEF), which produces strong transverse magnetic field in device. The EEF divides LVPD plasma into three regions namely Source, EEF and Target plasmas. Target plasma of LVPD shows the instability excited due to presence of electron temperature gradient (ETG). We have demonstrated in LVPD that the threshold condition for the ETG mode, i.e. $\eta_e = L_{ne} / L_{Te,} > 2/3$ where $L_{ne}^{-1} = -(d \ln n_e / dx)$ and $L_{Te}^{-1} = -(d \ln T_e / dx)$ are the density and electron temperature gradient scale lengths are satisfied the plasma background condition for this instability and observed fluctuations are characterised by wavelength ordering, $k_\perp \rho_e \le 1 << k_\perp \rho_i$ and frequency ordering, $\Omega_i < \omega << \Omega_e$, where $k_\perp$ is the perpendicular wave vector, ρ_e, ρ_i are Larmor radii of electron and ion, respectively, and $\Omega_{ci,,}$ Ω_{ce} and ω are the ion, electron gyro frequencies, confirms its presence in LVPD. Investigation reveals that the observed instability in LVPD resides in lower hybrid range of frequency and exhibits electromagnetic nature. The presence of such fluctuations are observed in most of the fusion devices and found an important role in electron heat transport. Several signatures of the observed turbulence are consistent with the theoretical predictions made for finite beta ETG modes for LVPD plasma [24].

This thesis addresses the plasma turbulent transport problem due to electron scales fluctuations in LVPD (a linear plasma device) which is excited by presence of electron temperature gradient (ETG). The problem of plasma transport is envisaged over the years as a major plasma loss problem in magnetically confined fusion plasma devices. As no clear understanding on experimentally observed plasma transport phenomena, of electron scales exists hence it has invited uninterrupted attempts in the domain of theoretical, computational and experimental investigations for better understanding of the physical phenomena responsible for it. It is predicted that small scale turbulence plays a major role in determining the global confinement properties of fusion plasmas. But due to its small scale (~ μm) not possible to explore in most of fusion devices. The motivation for this work comes from the background of micro-turbulence induced anomalous transport problem encountered in fusion plasmas.

Based upon the above outline, this thesis reports on the experimental demonstration of ETG turbulence induced particle and thermal fluxes. The contents of the thesis are summarized as follows.

In Chapter 2, details on experimental setup and diagnostic system are provided. In this chapter, the emphasis is on the developmental work carried out towards the automation of device, on experimental tools and on development of diagnostics for carrying out investigations on ETG induced plasma transport. The major contributions are namely, 1) development of triple Langmuir probe diagnostics for real-time temperature fluctuations measurement in pulsed plasma and its floating power supply, 2) development of computer based control of linear probe drive for better spatial resolution, 3) establishment of PXI based data acquisition system with better bit resolution and sampling rate, 4) development of specially designed probe diagnostics for particle, energy and parallel electron and ion current measurements besides developing several MATLAB routines for carrying out data analysis. Microwave interferometry diagnostic for chord averaged density measurements is another important development carried out in LVPD during this time. It works as a residential diagnostic in the device for depicting state of wall conditioning after each vacuum break LVPD suffers and provides hands-on information on plasma density. A revisit to the performance of Electron Energy Filter (EEF) for the identification of ETG in target plasma of LVPD is carried out. A brief description of LVPD device including its auxiliary systems namely, pumping system, confinement system, plasma source, power supplies, and diagnostic system is also provided.

In Chapter 3, experimental study of particle transport due to electrostatic fluctuations is provided. In this chapter, we present results on the investigation of particle transport due to ETG turbulence, estimated by correlated density and potential fluctuations respectively. Experimentally obtained density- potential cross-correlation, power spectra and frequency-wave number ordering confirms that the observed turbulence is driven by electron temperature gradient. The experimentally observed fluctuation driven ES particle flux is found negative i.e., directed radially inward. We correlated it with particle pinch problem of tokamaks. The plasma density maximizes in the core region when EEF is ON which is not the case when EEF is OFF thus indicating that the inward particle flux resulting from ETG fluctuations plays a significant role in it. Net particle flux is finite and it results because the phase difference, $\theta_{\delta n,\delta\phi}$ deviates from 180^0 in ETG dominated plasma. The observed cross phase angle and flux have been compared with theoretical estimates and an agreement is found within 20% accuracy for all radial locations.

In Chapter 4, details on experimental study of particle transport due to electromagnetic (EM) fluctuations are described. In finite plasma beta of LVPD, EM particle flux is measured with specially designed array of probes. The array contains a pair of directional probes for parallel electron and ion current and a 3-axis B-dot probe for the measurement of magnetic field fluctuations. We have found that observed EM flux in LVPD is non-ambipolar in nature and exhibits a finite EM flux for its open field like scenario, in contradiction to the prediction by slab ETG model equations where EM flux is predicted as zero. A quasilinear theory is proposed to explain the observed finite flux. This theory also suggests that the non-ambipolarity of EM flux may be balanced by the sum of the divergence of Maxwell stress $\frac{\partial}{\partial x} < \delta B_x \delta B_y >$ and $< \delta B_y \frac{\partial}{\partial z} \delta B_z >$. The pseudo ion flux is similar to ion flux in morphology, had the ions been magnetized. It was demonstrated that quasi-linear estimates of the EM pseudo ion flux due to parallel ion current fluctuation compares well with the measured flux and hence the role of sluggish ion motion assumed significance.

In Chapter 5, experimental studies on plasma energy transport due to electrostatic (ES) and electromagnetic (EM) fluctuations are reported. This chapter discusses heat flux measurement originated from finite temperature, potential and density fluctuations in ETG turbulence dominated plasma. Both conductive and convective fluxes are considered for estimating total heat flux. A specially designed floating TLP is developed for this purpose. The TLP assembly is capable of measuring simultaneously electron temperature, floating potential and plasma density fluctuations. The heat flux is measured and is found positive, opposite to the observed particle flux. Also, using ETG model equations, theoretical expression is derived for the estimation of heat flux due to ES and EM fluctuations. The phase angle between electron temperature and potential fluctuations shows a good agreement with the theoretical predictions derived from the ETG model equations.

Finally, in Chapter 6, we consolidated our work enumerating on the major tasks that can be undertaken for further research in this field.

Chapter 2
Experimental setup and diagnostics

The large volume plasma device (LVPD) experimental system, imbeds several features, adding enough versatility to enable it to address wide variety of physical problems relevant to Magnetospheric and fusion plasmas. The motivation of the device was to understand various phenomena related to electromagnetic structures, waves, plasma turbulence of small and large scales, significant for fusion plasmas etc. [51]. The major features of it are namely, (1) large area, stable, multi filamentary plasma source, (2) radial and axial confinement systems, (3) LabVIEW interfaced pulsed power supply systems (turn off time ~ 10 μs), (4) a large solenoid, called electron energy filter (EEF), installed for the purpose of making plasma devoid of energetic electrons and for profile modifications to suit ETG turbulence studies, (5) plasma diagnostics like Langmuir probes, Double probe, Triple Langmuir probe, Microwave interferometry, B-dot probe, Centre Tapped Emissive Probe, Directional probes etc., (6) LabVIEW interfaced, motorised, linear motion probe drives with large travel length capability and (7) a 40-channel, PXI based data acquisition system with high sampling rate and large record length for carrying out ETG plasma transport studies.

The device produces a boundary free plasma due to its large size (*length* = 3 m and *diameter* = 2 m), a typical photograph of device is shown in Figure 2.1 . It is capable of accommodating electromagnetic wave for basic study in boundary free plasma condition. Its voluminous size, despite accommodating Electron Energy Filter (EEF) like solenoid in it leaves apart sufficiently large volume available for carrying out investigations of electron temperature gradient induced ETG turbulence, presently considered as a major source of plasma transport in fusion relevant machines in boundary free plasma. Uniformity of magnetic field over large dimension (1.5 m × 2.5 m) and availability of multiple access ports (94 nos.) to plasma for visual and intrusive measurements provides liberty for detailed plasma investigations.

Figure 2.1 Photograph of Large Volume Plasma Device (LVPD)

The description of various subsystems in the device is as follows. The device details and confinement system is described in section 2.1. In section 2.2, the power supply system used in LVPD is described with details on the newly coupled filament power supply. The plasma source and plasma production are described in section 2.3. The large solenoid, called EEF is installed at the axial center of LVPD and is used for profile modification to carrying out Electron Temperature Gradient (ETG) driven turbulence and induced transport studies in target plasma of LVPD. Details on this are described in section 2.4. The diagnostics used for carrying out ETG induced transport studies are detailed in section 2.5. The LabVIEW interfaced Linear Probe Drive (LPD) system developed for carrying out measurements, devoid of errors introduced due to manual intervention in probe movement over a large radial distance of LVPD is described in section 2.6. Finally, the chapter will close with section 2.7, where description on signal conditioning and data acquisition system is provided.

2.1 Device description

The experimental setup primarily includes a vacuum chamber and confinement system.

2.1.1 Experimental chamber

The schematic of the LVPD device with its support structure is shown in Figure 2.2. This is a water cooled, double walled, the cylindrical device made up of two Stainless Steel (SS-304) chambers, each of dimension (L = 1.5 m, ϕ = 2 m). It has dish-shaped SS hemispherical and motorized end covers. The two halves and the end covers are provided double Viton O-ring sealing. The two halves are bolted together permanently but are electrically isolated whereas dish ends are hydraulically clamped with remote operation facility. The access to the vessel is provided by 94 ports, spread all over the device surface. The disc ends are mounted on a movable platform [26].

The vessel is pumped down to a base pressure of $1.6 \times 10^{-6}\, mbar$ by a pumping system made up of a pair of the root (1775 m^3/h)– rotary ($175 m^3/h$) and Diffstak (03 nos., 1700 l/m each)- rotary (03 nos., 41.5 m^3/h each) combinations.

The conventional gauges (pirani, penning, ionization gauge and automatic pressure controllers are used for monitoring and controlling filled gas pressure in the chamber. A water cooling system capable of delivering about 600 LPM is used to cool vacuum vessel, magnet coil system and cathode assembly. It maintains a temperature between 60 -100 °C .

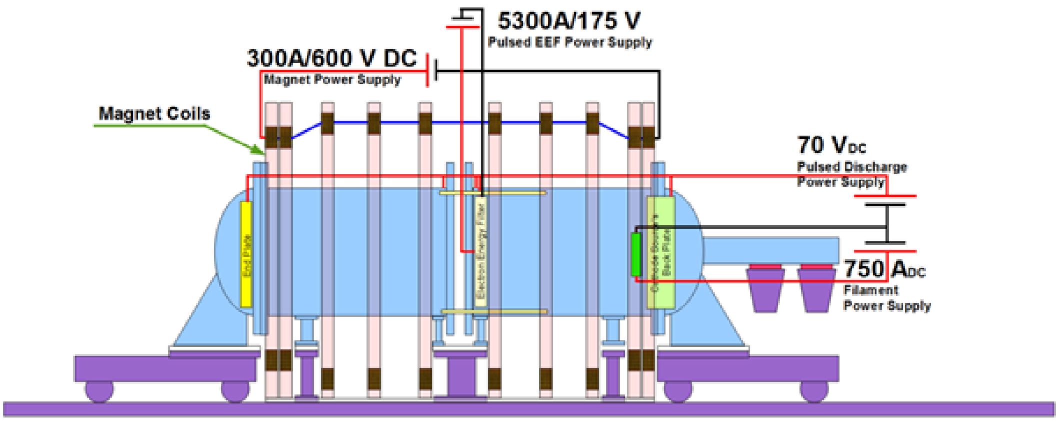

Figure 2.2. Schematic of the Large Volume Plasma Device (LVPD)

The plasma source is in the right side of chamber as shown in Figure 2.2. Magnet system (Magnetic field ≤ 150 G) consists of 10 circular coils are used for radial confinement.

2.1.2 Plasma confinement system

The plasma confinement system consists of (1) radial confinement system and (2) axial confinement system.

2.1.2.1 Radial Confinement

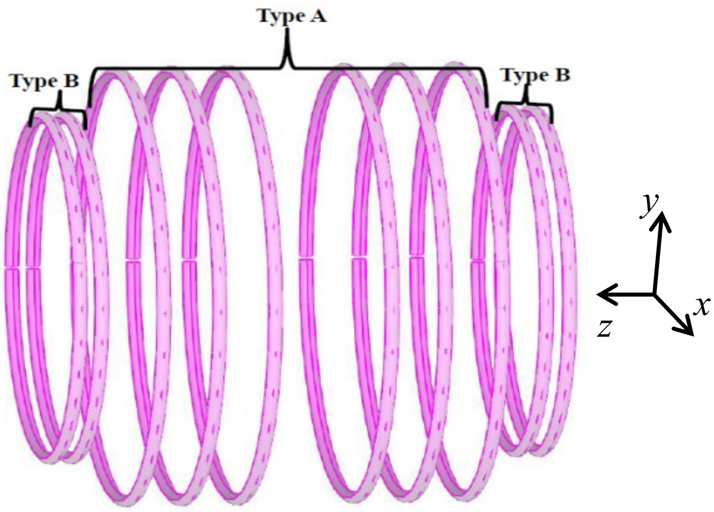

Figure 2.3. Schematic of 10 set of coils garlanded on LVPD to provide radial confinement to the plasma produced.

The radial confinement of plasma in LVPD is provided by a set of 10 coils, divided into two set of coils of type A and B. Out of these, type A are 6 coils in numbers with dimension (ID = 2900 mm, OD = 2975 mm) and type B are 4 coils of dimension (ID = 2300 mm, OD = 2375 mm). The coil locations are optimized to produce uniform magnetic field of 150 G in the device, for the maximum current of 300 A [26]. The axial and radial magnetic field profiles are plotted in Figure 2.4.

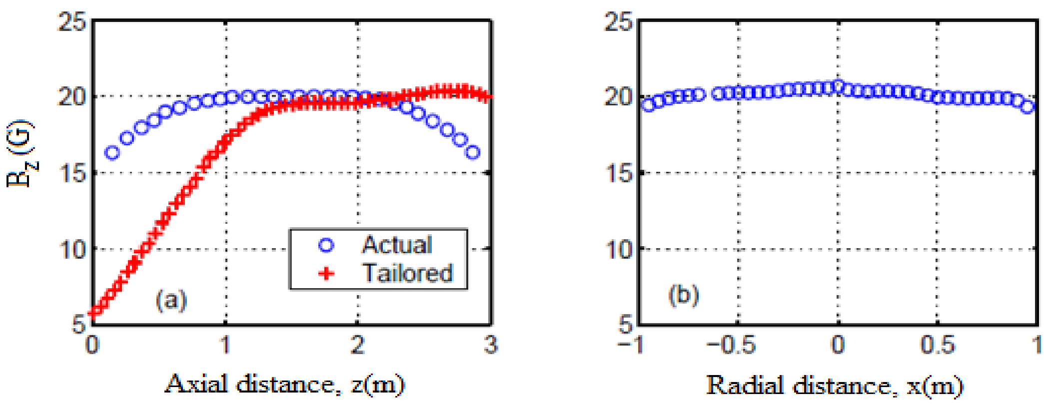

Figure 2.4. (a) Axial profile of magnetic field produced by garlanded coils. The curve in blue color shows the uniform field which can modify to produce a tailored field

(red color) by individually controlling the individual coil currents and (b) Radial profile of axial magnetic field for uniformity validation. These magnetic field profiles are obtained for 20 A of current fed to the coil system.

We have added an additional feature of shunt across each coil for producing desired magnetic field profile. This has allowed us to make a tailored magnetic field profile in source side for better uniformity and helps in diminishing the effect of filamentation on plasma density in LVPD. The used tailored field is shown in Figure 2.4 (a).

2.1.2.2 Axial Confinement

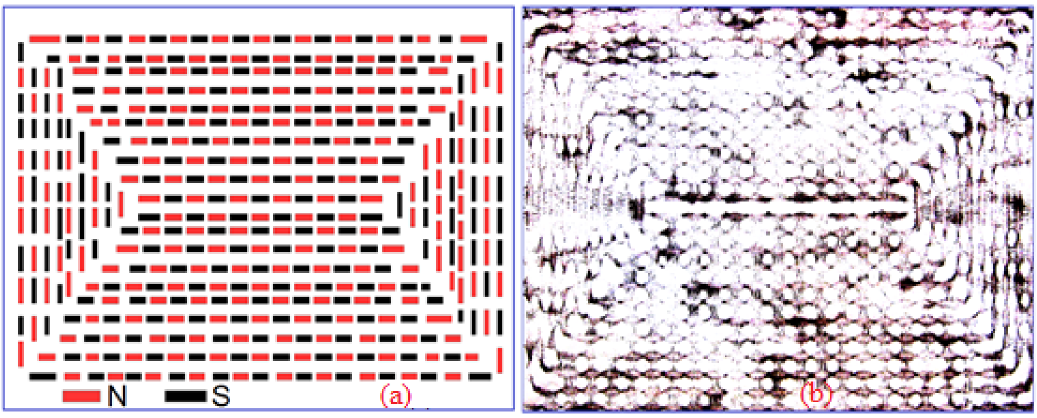

Figure 2.5. (a) Magnets in line cusp configuration in rear plate of cathode and (b) the obtained field pattern by using iron fillings.

In open field line configuration, most of the plasma loss is observed along the field lines in both forward and reverse directions of cathode. In LVPD this is contained by developing a cusp field over metal plates by using permanent magnets of $4\ kG$. In the rear side of cathode, as shown in Figure 2.5, line cusp geometry is used. In Figure 2.6, the end plate with broken line cusp magnetic field and its magnetic field pattern is shown.

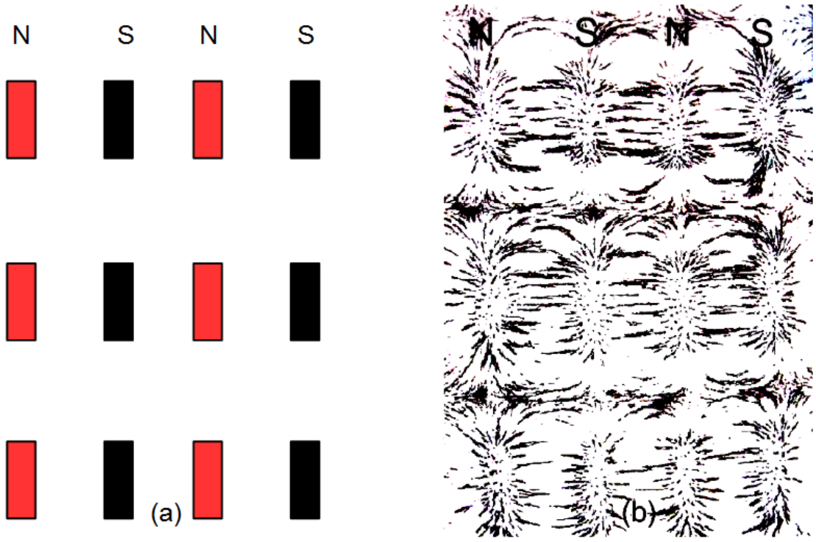

Figure 2.6. (a) Schematics of the broken line cusp arrangement in the front side plate of cathode for axial confinement of plasma and (b) magnetic field pattern using iron fillings.

2.2 Power supply system

The power supply system used in LVPD comprises a set of four power supplies namely, 1) the magnet power supply, 2) the discharge power supply, 3) the EEF power supply and 4) the filament power supply. The details about the magnet, discharge and EEF power supplies are described in other references [26,52,53], the 10kA/20V filament power supply is installed during this thesis work. The magnet power supply is a 300A/600V, controlled 12 pulse AC/DC thyristorised convertor power supply. The power supply which can be operated in constant current or voltage mode has inbuilt interlocks for protection for water, pressure and temperature. It offers an extremely low ripple percentage at full load for voltage (0.5% peak to peak) and for current (0.1% peak to peak) respectively. The discharge power supply in LVPD was built in house and has an inbuilt feature of fast turnoff ($\leq$ 20 μs) especially incorporated for carrying out active whistler wave investigations in afterglow plasma free of energetic electrons. This utilizes parallel combination of 08 numbers of IGBT switches with equal current sharing arrangement and has a capability of delivering 4 kA of current with fast current disruption capacity of 20 μs. This supply can be operated for 9.2 ms for LVPD discharges. In similar lines, EEF power supply is configured for a current delivery rating of 5.2 kA /100 V by using a set of 10 IGBT switches. It is operated for pulse duration of 12ms.

The filament power supply is a 3-phase high current DC power supply rated for 20 V and 10 kA operation. It has a 24 pulse rectifier driven by fast and precise firing of thyristors and regulation better than 1% of the full scale value. Internal power supply components have air circuit breaker for connection to the grid and thereafter two phase shifted transformer in star-delta connection.

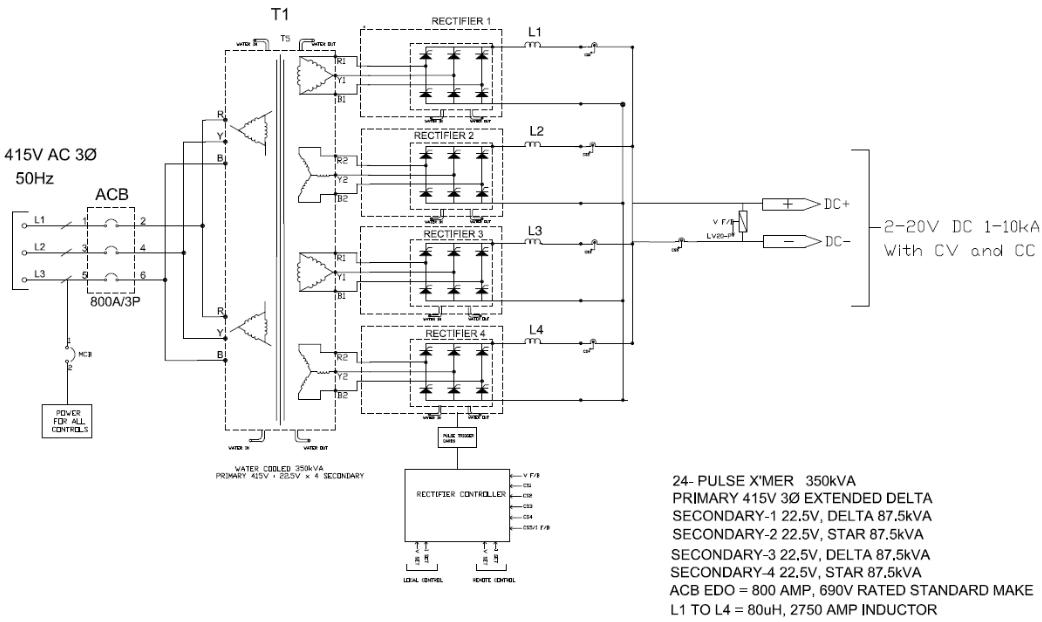

Figure 2.7. Electrical schematics of the 10kA/20V filament power supply.

The primary current of star configuration is at the deviation of ±7.5º with reference to the input supply. The primary is forced air cooled and secondary is water cooled. Rectifier circuit consists of 24 thyristors for power regulation along with 4 freewheeling diode for protection of individual stacks. Four numbers of water cooled DC chokes work as current combiner. The regulated output is feed to the filamentary cathode using suitable power transmission bars. The electrical scheme is represented by Figure 2.7**.** The control hardware developed for its operations follows the schema given in Figure 2.8**.**

The control system schema is based on semi-autonomous control implemented by two interacting controller boards. The first controller board is inside the power supply (named as Local power supply controller (LPSC)), which handles (a) local sensors and transducers, (b) power components and (c) thyristor firing circuit. In remote operation mode, it interacts with PC using Modbus communication on RS485 serial bus. The LPSC is intelligent enough to shut down power supply automatically in case of any internal fault and also interlocked with the external trigger. The detail design of the control system is described in reference [54] and schematically represented in Figure 2.8.

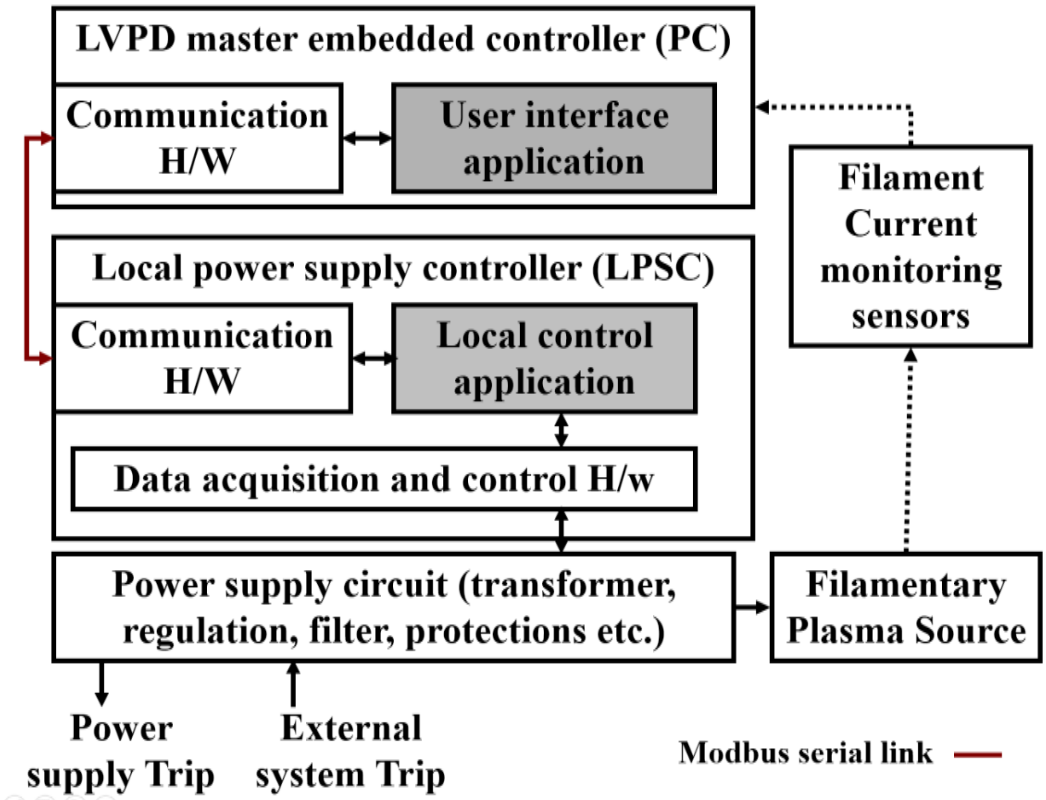

Figure 2.8. Control hardware of filament power supply used in LVPD.

The power supply operates in pulsed and continuous mode. In the pulsed mode, pre-programmed pulsed operation in constant current (CC) or constant voltage (CV) can be achieved. In continuous operation mode, the interactive control of the current and voltages is facilitated. The pre-programmed profiles for heating of filaments are required because of the temperature dependent characteristic of tungsten filaments. These profiles are controlled using LPSC and remotely using developed GUI of software interface on PC. The operation of power supply in CC mode in PC is shown in Figure 2.8. The software facilitates status display of current and voltage data using and alarm signals. It also provides facility to configure set points and controls interactively. The interface is standardized on Modbus to facilitate its easy integration. The Modbus control registers are specific to the power supply but handled using generic communication protocol. The software is developed on LabVIEW 2014 using NI Modbus library.

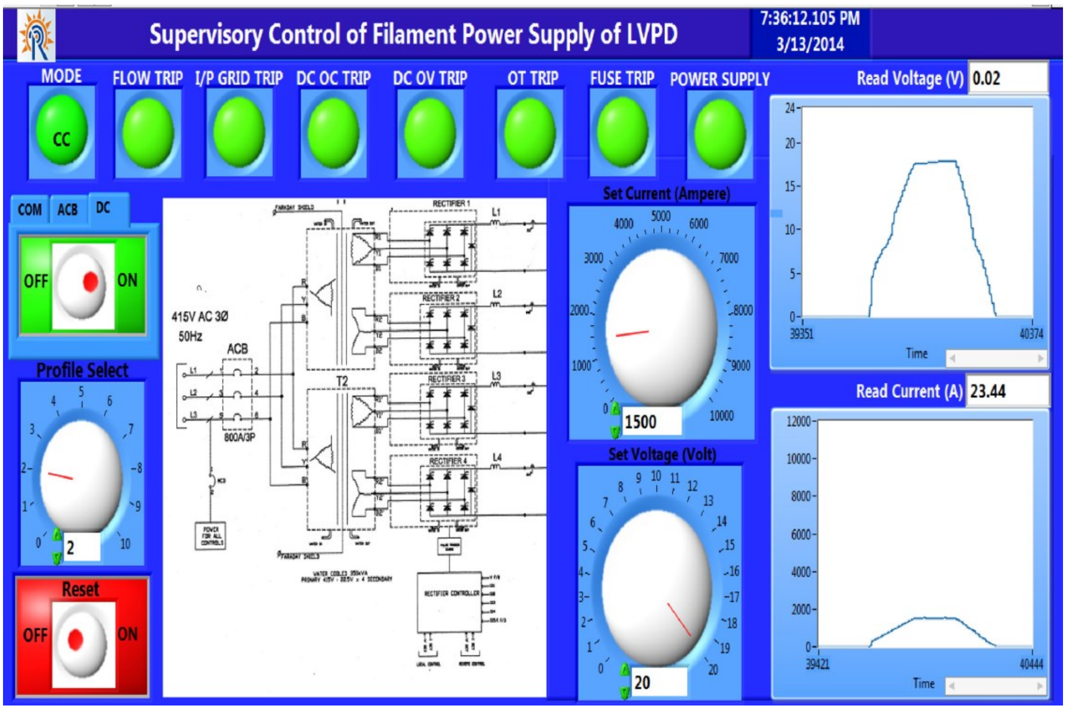

Figure 2.9: Graphical user interface for interactive control of filament power supply.

The full load testing of power supply is carried out on dummy load for 10kA. The control system implementation provides safe and flexible operation of the power supply with the existing plasma source.

2.3 Plasma source and plasma production

The plasma source in LVPD is a multi-filamentary plasma source, made up of 36 tungsten filaments. These filaments are arranged inside a multi-cusp rectangular box of dimension (L = 1600 mm, H = 800 mm and W = 200 mm) and are distributed on the periphery of a rectangular backplate of dimension (1300 mm × 900 mm). The cusped box is made up of ETP grade copper and is water cooled. The primary electrons and plasma confinement in the plasma source is supported by continuous magnetic line cusp made up of Samarium-Cobalt magnets of surface magnetic field of $4kG$. The filaments are fabricated of tungsten wires in V- shaped geometry having dimension(ϕ = 0.5 mm, L = 16 cm)respectively. The filaments are screw tightened to molybdenum current feed through powered by current carrying isolated copper bus bars having cross-section (50 mm × 10 mm) and are mounted behind the cusped plate of anode box. The source assembly is mounted on the movable dish end dome of LVPD.

Pulsed Argon plasma ($\Delta t = 9.2\ ms$) is produced in LVPD at a neutral pressure of 4.0×10^{-4} mbar by primary ionising electrons through electron impact ionization. The filaments are heated to a temperature of approximately 2500 K by passing a current of 750 A at maximum voltage drop of 15 V. The filament power supply is rated for 10 kA/ 20 V. A discharge voltage of -70 V is applied between the negative terminal of the filaments and the anode (device). The system, power and electronic signal grounds are independently configured and are branched to a unified ground. The plasma source is capable of producing a uniform plasma column of density, $n_e \approx 3.0\times10^{17}$ m^{-3}, electron temperature, $T_e \approx 3 - 5$ eV with a radial uniformity up to $80cm$ at an uniform axial magnetic field of 6.2 G in LVPD. The schematic showing the filament assembly is shown in Figure 2.10.

The plasma discharge current, total power consumption and water cooling requirements are estimated in the following subsections. The emission current density is estimated from the Richardson equation, $J_c = A_c T^2 \exp^{\left(\frac{E_w}{KT}\right)}$ in A/cm^2, where A_c = material dependent constant, T = emission temperature, K = Boltzmann constant and $E_w(for W) = 4.5\ eV$. For LVPD, at T = 2500^{0}K, Tungsten yields a current density of $J_c = 3.2\ A/cm^2$ and A_c = 1.2 × 10^6 Am^{-2}K^{-2} is considered for the calculation of the emission current density.

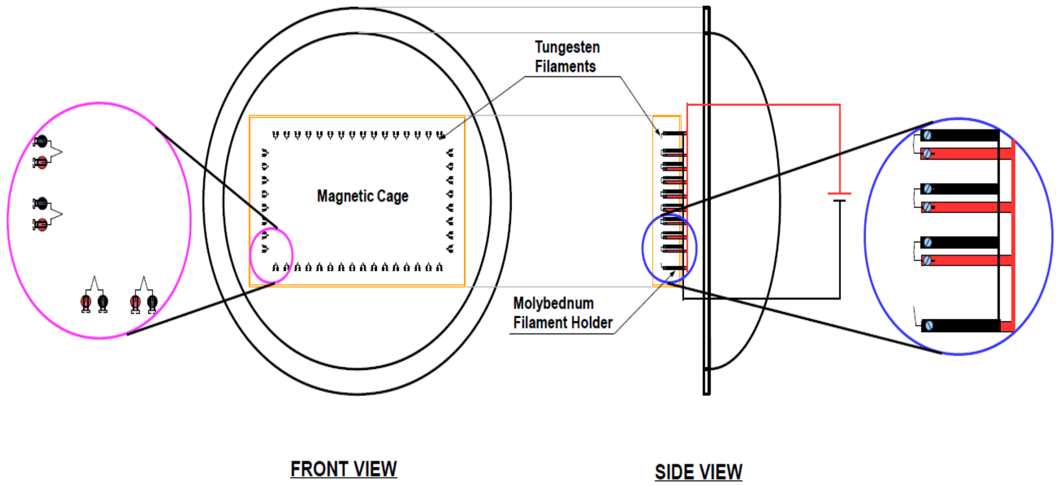

Figure 2.10. The schematic showing the front and side view of the cathode in the filaments holding enclosure. The filaments and their electrical connections are shown separately for clarity. The shape to the filament is given for better emission.

The total surface area of 36 filaments is calculated to be $S^{eff}_{filament} = 6.22 \times 10^{-3}$ m^2, the net current in case of ideal conditions can be drawn from the filament system is $I_{emission} = J_C \times S^{eff}_{filament}$ = 200 A This value agrees well to the experimentally obtained plasma discharge current of $I_d \approx 180 Amp$ at an applied discharge voltage of 70 VDC. For the calculation of the predicated discharge current from the source, the work of Stirling et al., [55] has been adopted. The discharge current calculations are carried out by balancing the production of the energetic electrons and loss rate of the ions. In steady state, $\frac{dn_i}{dt} = 0$, hence it can be written as $n_p n_n < \sigma_i \upsilon_e >= n_i / \tau$, where n_p is the density of primary ionising electrons. n_n is the neutral density, σ_i is the ionization cross section, ϑ_e is the velocity of the primary ionising electrons, n_i is the ion density and τ is the confinement time respectively.

The plasma volume (V_l), total emission area of the filaments ($A_{filament}$), primary electron loss length (L_{loss}), and mean free path λ_{mfp} is considered for the calculation. After incorporating the terms, the final form of the equation can be written as, $I_d = n_i e V_l / X\tau$, where $X = L_{loss} / \lambda_{mfp}$, and $\lambda_{mfp} = 1 / n_n \sigma_i$. Substituting the values for total plasma volume of LVPD, $V_l \sim 9\ m^3$, ion density, $n_i \sim 3\ \times 10^{17} m^{-3}$, electronic charge, $e = 1.6\ \times 10^{-19}$, approximated mean free path, $\lambda_{mfp} \sim 1m$, primary electron loss length, $L_{loss} \sim 2.5$ m and confinement time, $\tau \sim 1\ \times 10^{-3} s$, the estimated discharge current obtained is $I_d \sim 216$ A.

The power consumption in the source function is estimated by Stefan – Boltzmann Law considering the emission temperature of $2500°K$. The net radiated power estimated as$\sim$ $10.5\ kW$. This has been compared with the actual total power consumption which comes out as ~ 10.2 kW. This agrees well with the net power balance in the source function.

Out of the total heat capacity of 200 kW of power supply, 90kW is being utilized. Half of the heat flux is considered to be falling on to the back plate surface area ($A_{LEES} = 2.2m^2$). The rise in temperature on the back plate is calculated using equation, $\Delta T = q(J) / (C_p \times m)$ where, ΔT is the rise in temperature, $q(J)$ is the incident heat flux in Joules, C_p is the specific heat of the copper ($0.39\ J/Kg.{}^{\circ}K$), and m is the total mass of the copper plate ($32\ Kg$). It was estimated that for a heating operation of $30\ s$, with $45\ kW$ of incidence heat load, the temperature of the plate rises to $110\ °C$ from its initial temperature. This rise in temperature is well within the allowable limit for safe operation of the magnets. The rise in the surface temperature is estimated without any cooling effect taken into consideration whereas the back plates are water cooled with brazed copper tubes.

Calculations are carried out for dissipation of effective heat load by keeping a maximum allowable temperature rise of $\Delta T = 30\ °C$. The heat flux dissipation is balanced by the displaced mass of water (mass flow rate) through cooling lines and is given by $Q = -kA_{LEES}(dT/dx)$, where Q is the total heat load, k is the thermal conductivity of the material. A_{LEES} is the effective surface area of the LEES, dT is the change in temperature and dx is the thickness of the material. For a heat load of 45 KW, $k \approx 400 W/mK$, $A_{LEES} \approx 2.2 m^2$, and $dx = 1.2X10^{-3} m$, dT is estimated to be $\approx 0.05°K$. The mass flow rate required for effective heat removal through water ($C_{p,w} \approx 4.18 \frac{J}{g.°C}$) channel is calculated as $\approx 11 ltr/m$. The effective water flow rate provided to the LEES through cooling channels is approximately $30 ltr/m$.

2.4 Electron Energy Filter (EEF)

The electron energy filter (EEF), installed in LVPD is designed for the purpose of scavenging the energetic electrons present in the plasma and to exert a control on the gradient scale length of electron temperature [27]**.** The design of EEF is based upon the previous works [56–58] ,discussing that multi-pole cusped magnetic field can be used to filter out energetic electrons. By using EEF, a plasma region devoid of non-thermal and primary ionizing electrons which is essential for carrying out ETG driven plasma turbulence and transport is established. The EEF is a highly transparent($\sim 82\%$), large aspect ratio solenoid, mounted at axial centre of device, produces a localized transverse magnetic field of 150G over the entire extent of LVPD($\sim 2m$) [59].

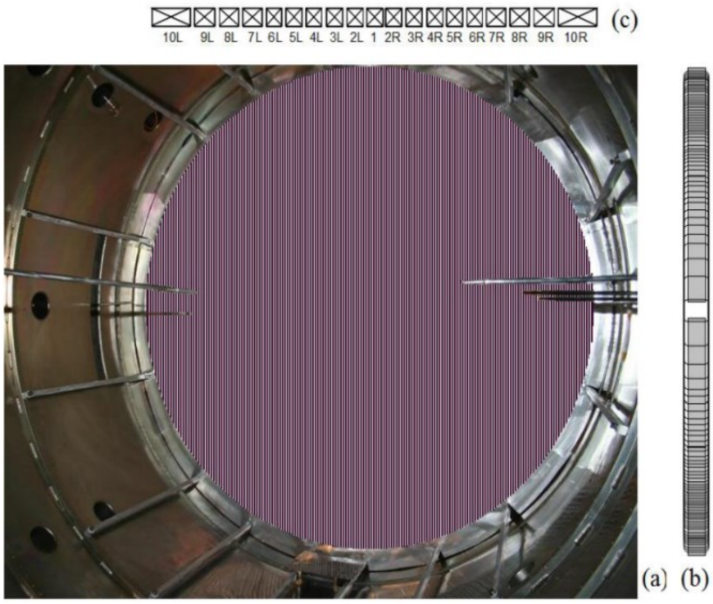

Figure 2.11. (a) EEF photograph installed in LVPD, (b) the side view of EEF cross section and (c) the top view of respective coils showing extent of coils.

The EEF solenoid is made up of 19 sets of coils and are made up of 155 numbers of Teflon coated silverized copper wire of cross section ~ 2 mm^2 (with radial separation of 12mm and axial separation between its two plates~ 40mm). All 19 coils are placed serially and are connected in parallel.

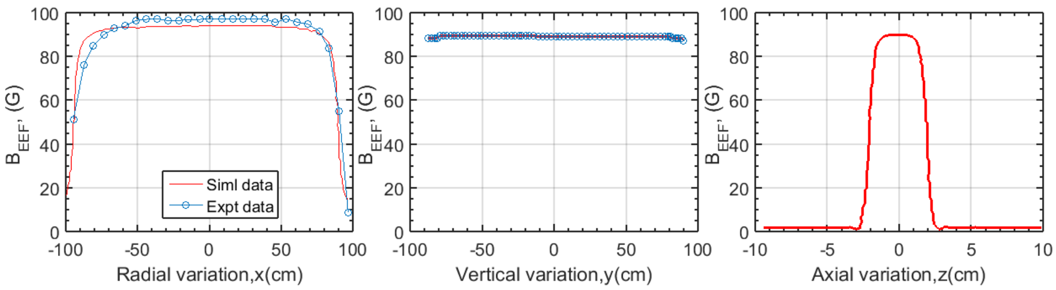

Figure 2.12. Field profile of EEF magnetic field (a) B_{EEF} along the radial variation (x-axis),(b) B_{EEF} along the vertical (y-axis) direction and (c) B_{EEF} along the axial direction (z-axis).

The uniformity of magnetic field produced by EEF coil is shown in Figure 2.12. The magnetic field components along the axis of EEF are measured and are simulated by the magnetic field code [60]. It is observed that B_{EEF} is uniform along the x and y axis of the device. Axial magnetic field is strongly localized to $-2\ cm$ to 2 cm and is measured along the device axis. This ensures that the plasma dynamics far from the EEF will not suffer because of near EEF strong magnetic field.

2.5 Plasma diagnostics

In this thesis work, plasma parameters, like plasma density (n_e), electron temperature (T_e), floating potential (ϕ_f) and plasma potential (ϕ_p) are measured by using cylindrical Langmuir probe. Conventional emissive probes are also used to measure the plasma potential. Directed electron and ion fluxes are measured using directional probes. The magnetic fluctuations are measured using B-dot probe. The density and potential fluctuations are measured with Langmuir probe and temperature fluctuations are measured by newly developed triple Langmuir probe and its results on fluctuations are compared with two probe technique. A non-invasive diagnostic of

Microwave interferometry is developed as resident diagnostics for the measurement of chord averaged plasma density for knowing the exact state of plasma density. The detailed description on these diagnostics is given later in this section.

2.5.1 Single Langmuir Probe (SLP)

The Langmuir probe (LP) diagnostics has been in use since it was first introduced by Irvin Langmuir in 1960 for the measurement of basic plasma parameters. The LP is a small conducting electrode of any shape (sphere, cylinder or planer) immersed in plasma and it allows local measurement of plasma parameters. It should have dimension larger than the Debye length (λ_D). The typical electrical circuit of LP is shown in Figure 2.13(a) and the Langmuir probe current voltage characteristics are shown in Figure 2.13(b).

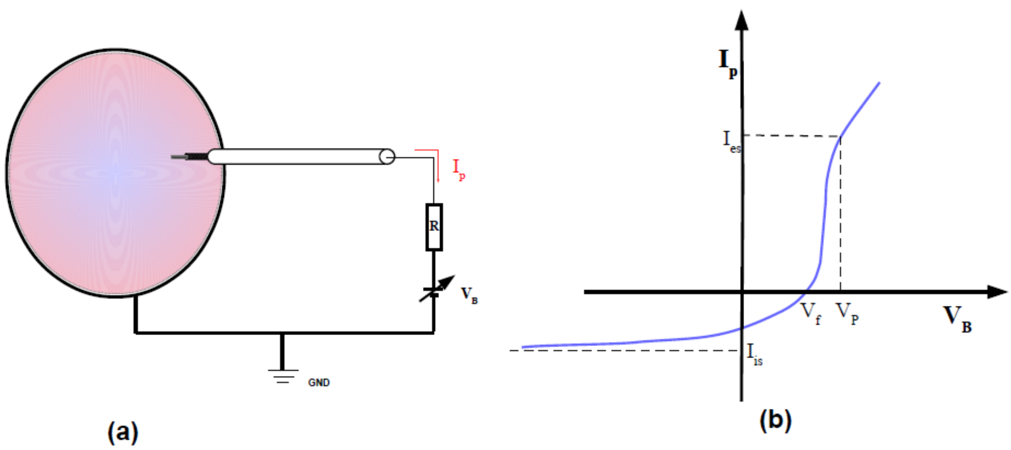

Figure 2.13. (a) Schematics of electrical connection for Langmuir probe diagnostic and (b) typical I/V characteristics of Langmuir probe.

The ideal Langmuir probe I/V characteristic can be modelled by the following probe current, $I_B(V_B) = I_{es}e^{(V_B - V_P)/k\,Te} - I_{is}$, where $I_B(V_B)$ is the probe current at biased potential of V_B, I_{es} is the electron current at the plasma potential $V_B = V_P$ and is defined as, $I_{es} = \frac{1}{4} e n_e A_{eff} V_e$, where $V_e = \sqrt{\frac{T_e}{2\pi m_e}}$, electron average velocity, e, m_e and A_{eff} are electronic charge, electron mass and effective probe area, respectively.

The typical plasma parameters of electron temperature, plasma density, plasma potential and floating potentials can be obtained like this. The electron temperature can be obtained in the following manner. The plasma parameters inferred with the Langmuir probe procedure are not sensitive to extrapolation of ion saturation current, since for $V_B > V_f$, $I_{is} \ll I_e$ hence we follow the linear extrapolation of I_{is} to get electron part of the probe characteristics $I_e(V_B) = I_B(V_B) - I_{is}$ for $V_B > V_f$. On taking the natural log of the Langmuir probe equation, we get

$\ln I_e = \ln I_{es} + \frac{eV_B}{kT_e} - \frac{eV_p}{kT_e}$, this implies $\ln\left(\frac{I_e}{I_{es}}\right) = \frac{e}{kT_e} V_B - \frac{eV_p}{kT_e}$ which can be compared to a straight line equation, $Y = mX + C$, where $Y = \ln\frac{I_e}{I_{es}}$; $X = V_B$ $C = \frac{eV_p}{kT_e}$ and slope $m = \frac{e}{kT_e}$. The temperature can be determined from inverse of the slope from linear region of logarithmic plot for electron current, which can be written as $T_e = \left[\frac{d\ln I_e}{dV}\right]^{-1}$.

The plasma density is calculated from the ion saturation current, which is extrapolated from conventional Langmuir probe characteristics. The expression for plasma density can be obtained from the ion saturation current by using the expression, $I_{is} = 0.6\, n_i e\, c_s A_{eff}$, which implies $n_i = \frac{I_{is}}{0.6 e c_s A_{eff}}$, where e , c_s and A_{eff} are electronic charge, Bohm velocity and effective probe area, respectively. The

Bohm velocity is defined by $c_s = \sqrt{\frac{T_e}{M_i}}$ where T_e is electron temperature and M_i is ion mass.

Theoretically, plasma potential is defined as the potential where electron probe current get saturated but this is generally not observed in most of the experimental Langmuir I/V characteristics. The typical plasma potential can be obtained from the intersection of two lines in the logarithmic plot of electron current as shown in Figure 2.14 (b). The intersection point is obtained by expanding the straight line on the linear region of $\ln I_e$ and saturated part of the curve. The more precisely plasma potential, $V_p$can be determined by differentiating $I_e(V_B)$ corresponding to maximum of dI_B/dV or where $\frac{d^2 I_B}{dV^2} = 0$.

The floating potential on the other hand is determined by the voltage at probe where it draws no net current. In general, where I/V characteristic of Langmuir probe shows zero current is defined as floating potential of plasma i.e., $I_B(V_B = V_f)$=0. This gives $I_{es} \exp \frac{e(V_f - V_p)}{kTe} - I_{is} = 0$; $\frac{e(V_f - V_p)}{kTe} = \ln \frac{I_{is}}{I_{es}}$ and $V_f = V_p + \frac{kT_e}{e} \ln \frac{I_{is}}{I_{es}}$, where$V_f$ is the floating potential, V_p, the plasma potential, T_e, the electron temperature and I_{is} is the ion saturation current. The ion and electron saturation currents are expressed as $I_{is} = 0.6\, n_i e c_s A_{eff}$ and $I_{es} = n_e V_{e,the} e\, A_{eff}$ where $C_s = \sqrt{\frac{T_e}{M_i}}$ and $V_{the} = \sqrt{\frac{8kT_e}{\pi m_e}}$ respectively.

On substitution, we obtain the expression of floating potential in terms of plasma potential and electron temperature for Argon plasma as $V_f = V_p - 5.5\, T_e$. For LVPD plasma, we measured the floating potential by using high impedance unbiased Langmuir probe.

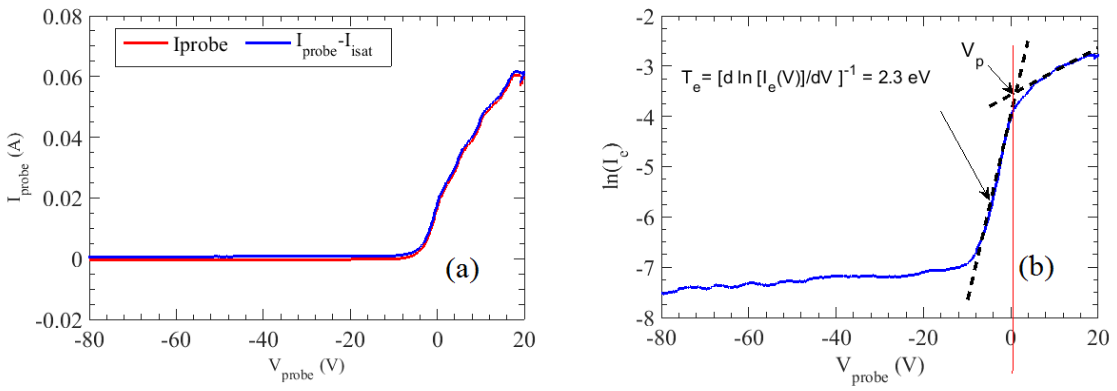

Figure 2.14. (a) shows the probe bias characteristic for probe and electron current and (b) the measured electron temperature for LVPD plasma in target region at x = 0 cm.

2.5.2 Double Langmuir Probe (DLP)

It consists of a pair of probes of equal area, which are mutually biased. The current drawn by an equal area double Langmuir probe immersed in a homogeneous plasma and biased to a voltage V is given by [61] , $I = \alpha A_{eff} en\left(\frac{2kT_e}{m_i}\right)^{1/2} \tanh\frac{e(V+V_d)}{2kT_e}$, where A is the area of the probe, V_d is the potential difference arising within the plasma and α is of order unit (values of 0.4-1.0) as reported by others [62].

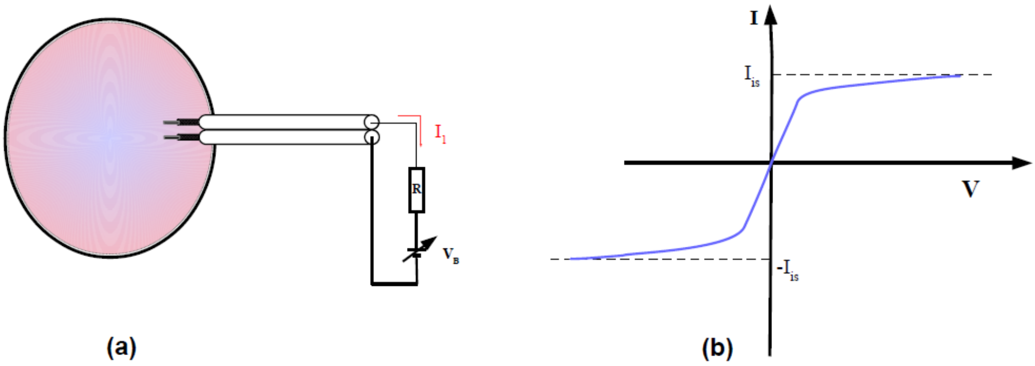

Figure 2.15. (a) Schematic of DP configuration, and (b) the typical I-V characteristic for DP measurements.

In this technique, the probe current is limited to ion saturation current and requirement of the knowledge of floating potential is not needed. The expression of electron temperature is given by

$$I_{sat}(V \to \infty) = \alpha A_{eff} n\, e \sqrt{\frac{2kT_e}{M_i}} \quad \& \; \frac{\partial I}{\partial V} = 0;$$

$$I(V \to 0)=0 \quad \& \; \frac{\partial I}{\partial V} = \alpha A_{eff} n\, e \sqrt{\frac{2kT_e}{M_i}} \frac{e}{2kT_e}$$

The electron temperature is estimated by using the bias voltage at intersection point of the slopes in the two regions by $T_e = \frac{I_{sat}(V\to\infty)}{2\left(\frac{\partial I}{\partial V}\right)_{V\to 0}}$

In this thesis, the DP diagnostic is used to validate the measurement of triple probe diagnostics by ensuring the floating condition of power supply for I/V measurement and by ensuring the symmetric DP I/V profiles for any pair of Langmuir probes in triple probe assembly.

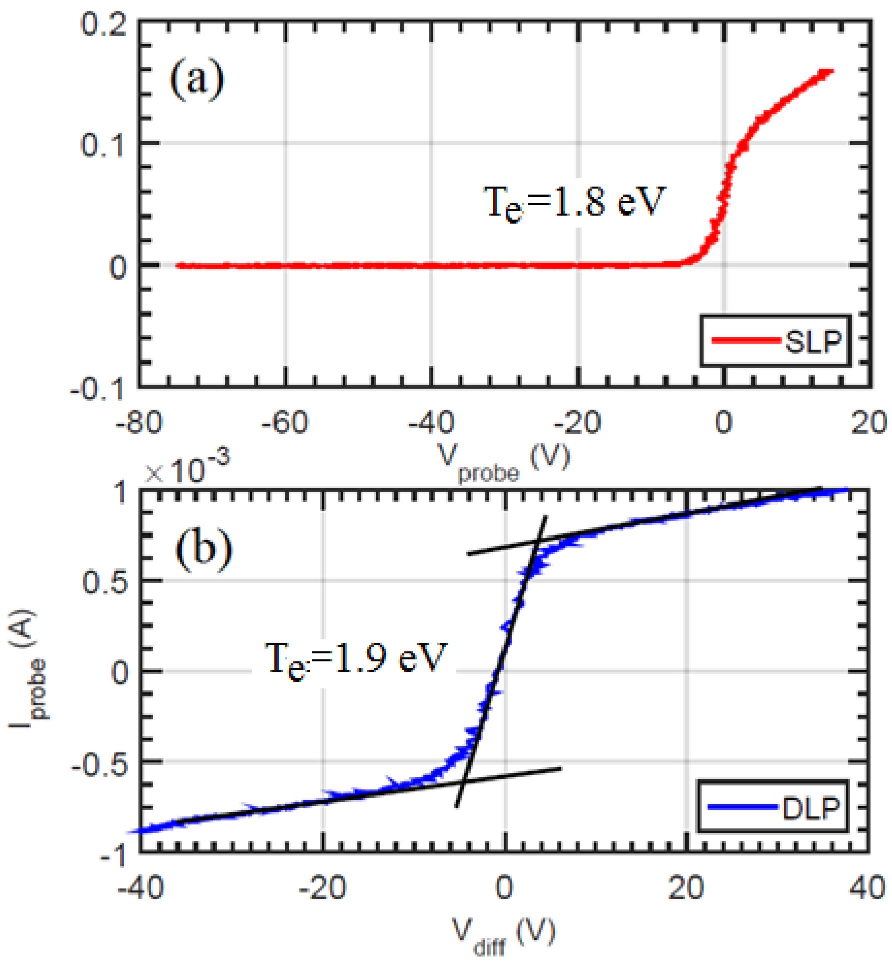

Figure 2.16. The I/V characteristics of (a) single Langmuir probe and (b) double Langmuir probe for plasma temperature measurement in target region of LVPD are shown.

In Figure 2.16, the electron temperature, T_e measured with the double probe is compared with single Langmuir probe for the same plasma region in LVPD. This shows that both seems to be sampling the similar plasma temperature.

2.5.3 Triple Langmuir Probe (TLP)

The single and double Langmuir probes have been widely accepted as a reliable measurement tool for a continuous plasma conditions with limitation of time-dependent measurement. However, real time measurement of electron temperature and its fluctuations in pulsed plasma needs a better tool as transient plasma conditions restrict the use of single and double probes. Furthermore, the single Langmuir probe suffer problem in proper estimations of plasma parameters when measurement are carried out in plasma where floating potential varies with time. This has been improved by incorporating the use of symmetric double probe. However, voltage sweep is still required to obtain I-V characteristics. Later on, Chen et.al. [63] modified this version of Langmuir probe by Triple Langmuir Probe(TLP) for the transient plasma conditions.

The TLP is based on the old technique (single Langmuir probe) and was formulated to instantaneously measure the plasma parameters by compromising minutely on spatial precision. The TLP consists of three probe tips where potential is applied across its two nearby tips and third one is kept floating. The three tips instantaneously capture three data points of the I/V characteristics, which is usually observed in case of SLP.

Let us consider three probes, P_1, P_2 and P_3 as shown in Figure 2.17, with identical geometric configuration and dimensions. They are placed in the plasma in close proximity to each other such that these probes samples same plasma condition. These probes will attain different potentials inside the plasma depending on the applied bias voltage and plasma conditions as shown in Figure 2.17 (b). In these probes P1 and P3 are used in double probe configuration, so the corresponding current must follow $I_1 = I_3$. Probe P2 is sampling floating potential of plasma.

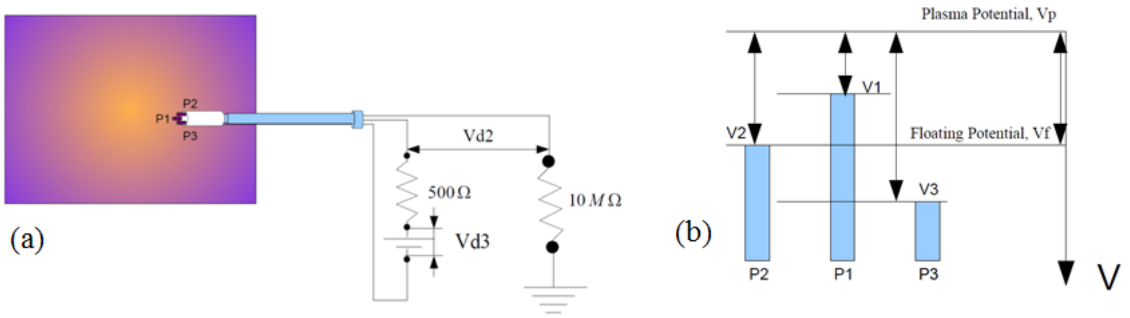

Figure 2.17. Schematic of (a) electrical connection for triple Langmuir probe diagnostic, and (b) potential diagram for three probes of TLP.

The validity of the probe theory requires the following assumption namely, 1) the electron energy distribution in the plasma is Maxwellian, 2) the mean free path of the electrons is much larger than both the thickness of the ion sheath around each probe and the probe radius, and 3) the thickness of ion sheath is smaller than the separation between probes, so that the interaction effects among the probes is negligible. The equation for currents for each probe can be written as

$$-I_1(V_1) = -I_{es}\exp\left(-\frac{e(V_1 - V_p)}{kT_e}\right) + I_{isat1}(V_1) \tag{2}$$

$$I_2(V_2) = 0 = -I_{es}\exp\left(-\frac{e(V_2 - V_p)}{kT_e}\right) + I_{isat2}(V_2) \tag{3}$$

$$I_3(V_3) = -I_{es}\exp\left(-\frac{e(V_3 - V_p)}{kT_e}\right) + I_{isat3}(V_3) \tag{4}$$

where $I_{es} = A_p J_e = A_p n_e e \left(\frac{kT_e}{2\pi m_e}\right)^{1/2}$, $I_{isat} = A_p J_i = A_p n_i e \left(\frac{kT_e}{m_i}\right)^{1/2}$, V_p and A_p are electron and ion saturation current, plasma potential and probe area respectively. Assuming that the geometrical probe area and corresponding ion saturation current for each probe are equal, i.e. $\mathrm{I_{isat1}(V_1) = I_{isat2}(V_2) = I_{isat3}(V_3)}$. Using equation (2 - 4), one can yield a current ratio, $\frac{\mathrm{I_1+I_2}}{\mathrm{I_1+I_3}} = \frac{\exp -\frac{\mathrm{e(V_1-V_p)}}{\mathrm{kT_e}} - \exp -\frac{\mathrm{e(V_2-V_p)}}{\mathrm{kT_e}}}{\exp -\frac{\mathrm{e(V_1-V_p)}}{\mathrm{kT_e}} - \exp -\frac{\mathrm{e(V_3-V_p)}}{\mathrm{kT_e}}}$. By taking into account $I_1 = I_3$ and $I_2 = 0$ since probe P_2 samples the floating potential of the plasma, the expression reduces to $\frac{I_1}{2I_1} = 1 - \exp(-\frac{eV_{d2}}{kT_e})$. For the condition,$\exp -\frac{eV_{d3}}{kT_e} < 1$, the temperature can be estimated from $T_e = \frac{V_{d2}}{\ln(2)} = \frac{V_2 - V_1}{\ln(2)}$. The instantaneous electron temperature is determined by choosing the proper scaling in measurement of potential difference, V_{d2} between floating to positive probe of double probe combination. The critical requirement of TLP diagnostic necessitates good floating ness for the measurement circuitry. For meeting this requirement, we developed in-situ, a versatile electronics circuitry consisting of a floating voltage generator and floating measurement card.

2.5.3.1 Pulsed power supply System

We developed a battery based floating power supply, which uses 12 DC batteries (each of + 12 V) to give rise sweep voltage of $\pm 140\,V$ in push pull mode. This power supply can be utilized for both, ramping as well as fixed biasing of the probe system. The typical block diagram of the circuitry is shown in Figure 2.18**(a).** The two output ends of this power supply can have a maximum range of $\pm\ 140\,V$. Here, individual ends can go to a maximum of $\leq 72\,V$. The typical voltage on two terminals of output is shown in Figure 2.18(b(i)) and Figure 2.18(b(ii)). The coupled out voltage as differential output is shown in Figure 2.18(b) (iii).

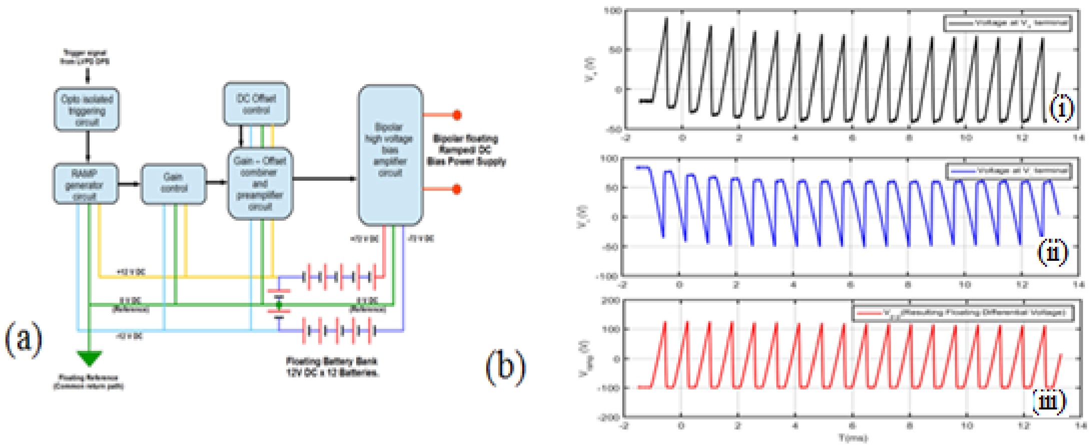

Figure 2.18. (a) Schematic of the floating bipolar / balanced sweeping circuit for symmetric bias span to P1(+) and P3(-) probes and (b) voltage measured at P1(+) and P3(-) probes in (b(i)) and (b(ii)) during the plasma shot with 10X probe shows shifting of potential due to the floating behaviour in plasma. The differential voltage appearing across these probes is shown in b(iii)) which is obtained by the subtraction. This exhibits nice symmetry needed for the double probe measurements.

2.5.3.2 Floating measurement circuitry

The measurement scheme adopted for TLP is such that one of the three probes is always floating while other two are biased with respect to each other. All the probes are however, floating with respect to device ground or measurement ground (both are same), and the biasing of the probes is with respect to each other. Since the probes have references through the plasma, the biasing circuit has a different 'ground' or reference voltage. The measurement is, therefore, undertaken with extremely large input impedances of IC PA85 which upon powering brings extremely large ground isolation ($\geq 50\ M\Omega$). The electrical schematic is shown in Figure 2.19**.** The scheme consists of three closely spaced, identical probes called as P_1, P_2 and P_3 arranged in specific design to sample similar plasma condition.

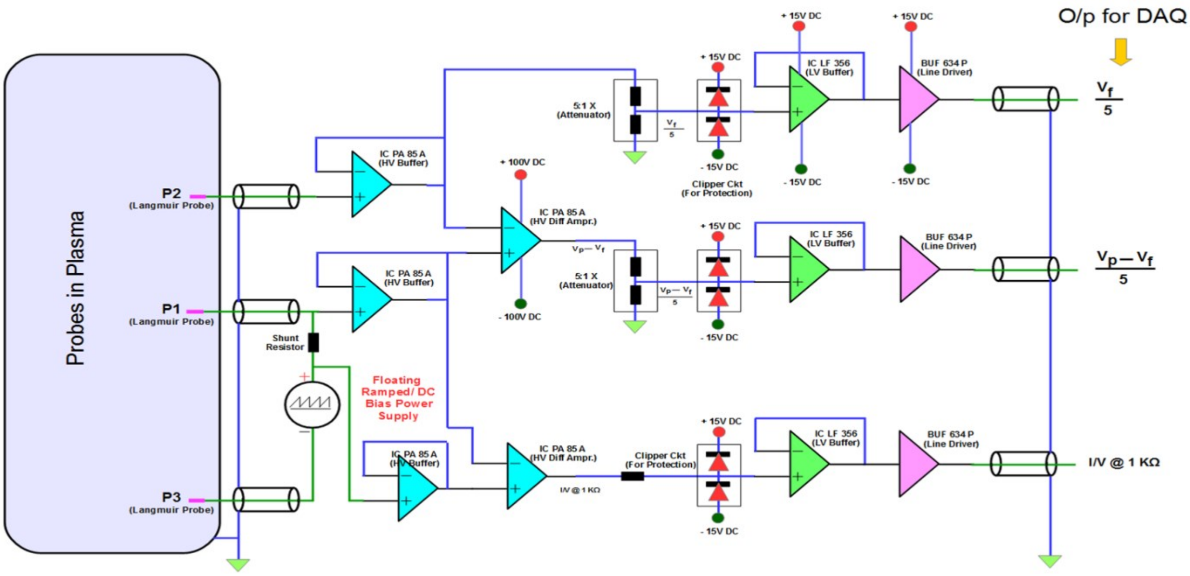

Figure 2.19. Schematic showing scheme of high impedance, high bandwidth TLP diagnostics in LVPD.

The scheme involves the measurement of ion saturation (I_{sat}) current by the biased $P_1$and P_3 against an applied floating biased potential along with the measurement of floating potential by P_2 with respect to ground. The electron temperature is determined with the real-time measured potential difference of the positive biased terminal and floating potential terminal and is estimated by $T_e = (V_+ - V_f)/\ln 2$. The accuracy in temperature measurement is ensured by choosing Vd3 sufficiently high ($> 3\, T_e/e$, where Vd3 is the voltage between P1and P3 probes). In this situation, the probe draws only ion saturation current. We obtained a correct voltage range of V_{d3} for each radial position to measure electron temperature and compared it with a single probe measurement. A brief description of measurements carried out in target plasma of LVPD is provided by the newly developed TLP.

2.5.3.3 Validation of Double Probe Configuration for TLP in LVPD

The identical nature of I/V characteristics when different pair of probes of TLP is used in DLP configuration suggests that the geometrical area, as well as plasma conditions, are same around the 3- TLP tips. The electron temperature is estimated from the formulation described above.

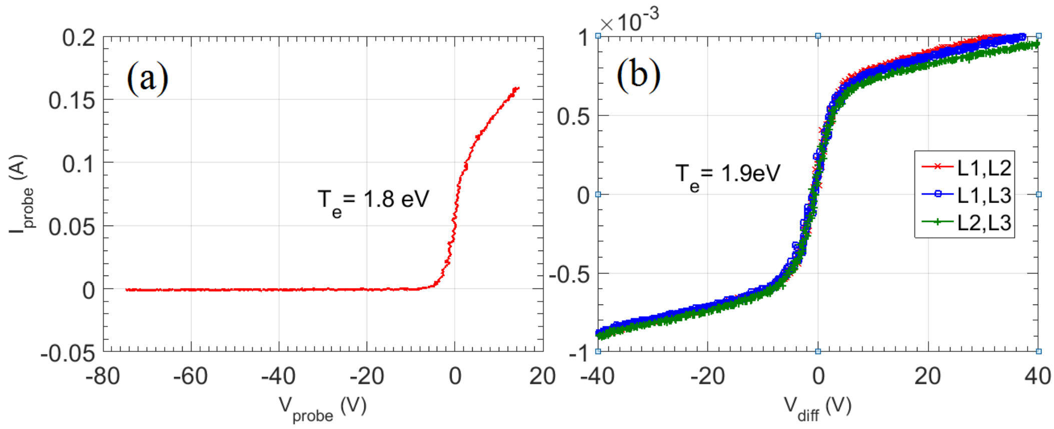

Figure 2.20. (a) Single Langmuir probe characteristics for electron temperature measurement and (b) double probe characteristics validating symmetry needed for TLP.

2.5.3.4 Determination of bias potential for T_e measurements

The proper measurement of electron temperature by a TLP requires the right selection of fixed bias voltage, V_{d3} for a given plasma potential. Work reported by SinLi [63] and Ghosh [64] mentioned that the improper selection of bias voltage leads to the wrong estimation of electron temperature.

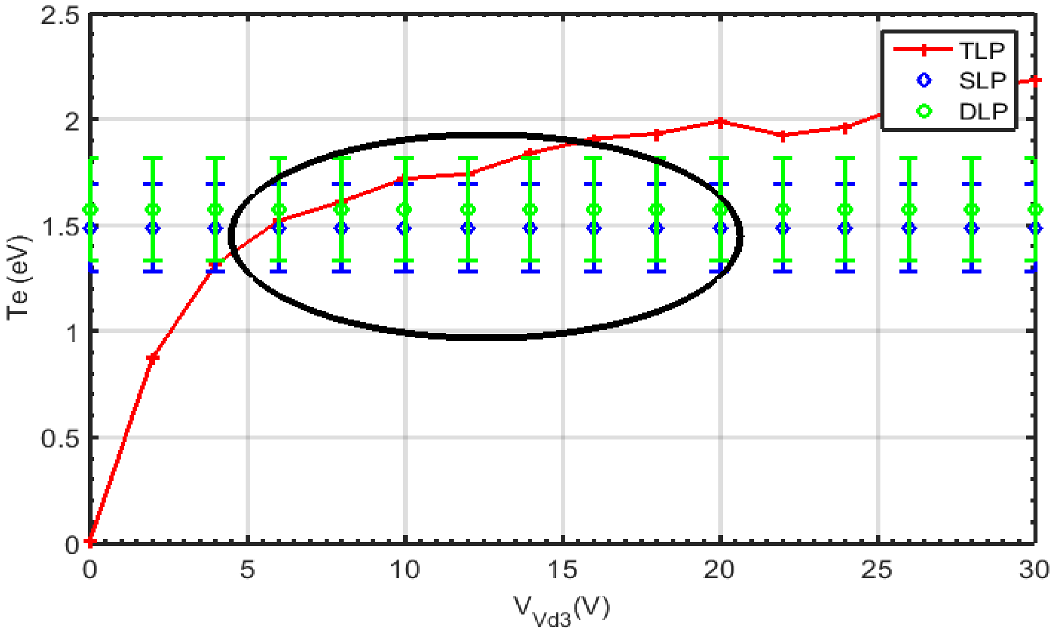

Figure 2.21. Variation in measured temperature by TLP at different, V_{d3}.

They proposed that V_{d3} should follow, $5V_{d2} < V_{d3} < 10\,V_{d2}$. In our investigations, we have first identified proper V_{d3} then carried out the measurement for electron temperature and fluctuations using TLP.

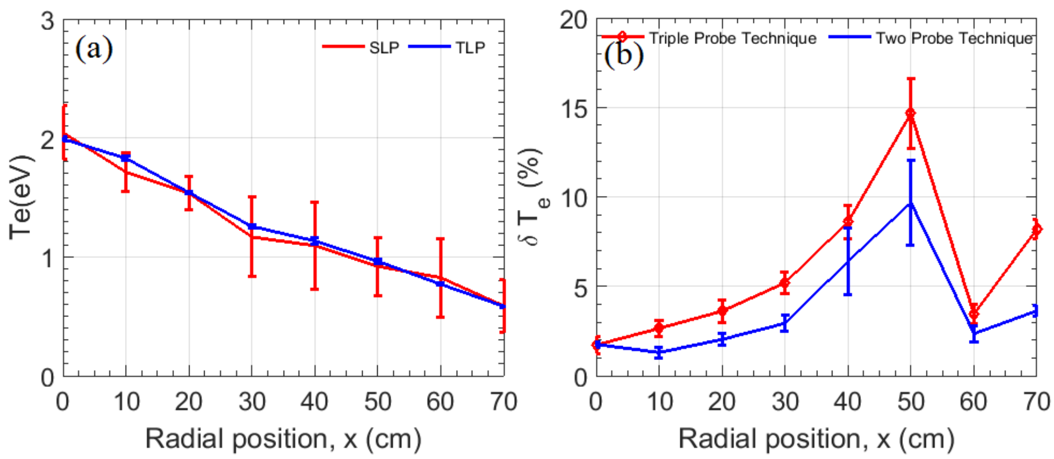

Figure 2.22. Comparison of radial variation of mean electron temperature measured by TLP with (a) single Langmuir probe and fluctuation levels with (b) two-probe technique, respectively.

As shown in Figure 2.22(a), we have estimated electron temperature, T_e using TLP circuitry for different fixed bias values of V_{d3} in the scale of $V_{d2.}$ The measured value of T_e is compared with SLP, which approaches it very closely for mean temperature whereas the temperature fluctuations are compared with the fluctuations measured using two probe technique [24]. We observed that, for V_{d3} ranging between 5 V to 15 V, the measured temperature and temperature fluctuations approaches closely the SLP and two probe method measurements.

2.5.4 B-dot probe

The finite plasma beta ($\beta \sim 2\mu_o \frac{nT_e}{B^2} \gg m_e/m_i$) in LVPD shows significant magnetic fluctuations. The magnetic field fluctuations are important from the perspective that they play an extremely important role to identifying the nature of plasma turbulence as well as to understand turbulence induced particle and energy transport. These magnetic field fluctuations can be measured by use of miniaturized solenoid based on Faraday's law of induced voltage. The voltage picked up by the probe is, $V(t) = N(d\phi / dt) = NAdB(t)/dt$ where N is number of turn and A is area of solenoid. This small solenoid is known as Magnetic probe (B-dot probe).

In this thesis, magnetic field fluctuations are measured by using a 3 axis B-dot probe. This probe is configured in bi-filer geometry and is capable of measuring all the 3-components of the magnetic field in the frequency band of (1-100) kHz. The design and construction are based on the Everson model of B-dot probe [65]. Its design eliminates electrostatic pickup, reduce physical size and increase the signal to noise ratio while maintaining a high bandwidth. The bifilar configuration ensures significant rejection of capacitive pickup which is excited due to the capacitive charging of probe during the plasma discharge. The probe is tested for capacitive rejection, inductive pickup and frequency response. An electrical equivalent of B-dot probe is shown in Figure 2.23(a). The frequency response of B-dot probe in a uniform magnetic field of Helmholtz probe is shown in Figure 2.23(b).

The probe is calibrated for inductive pickup in plasma. Figure 2.23 (c) shows the pickup voltage when the probe is rotated between $0° - 180°$. Marginal asymmetry is observed between signals of 0° and 180°, the reason for this may be due to the capacitive corruption. Here, zero is considered when the flux cutting surface is transverse to the field lines. In Figure 2.23 (d), the B-dot probe is calibrated for its response in plasma. The flux cutting surface of the probe rotated through 360° to obtain a symmetric cosine waveform for pure inductive signal in plasma. A marginal deviation is again observed in the cosine waveform indicating minor poisoning due to capacitive pickup. The effect of the capacitive pickup is taken care in calculating the electromagnetic particle flux by the ratio of signals obtained at 0° and 90° with respect to B_z.

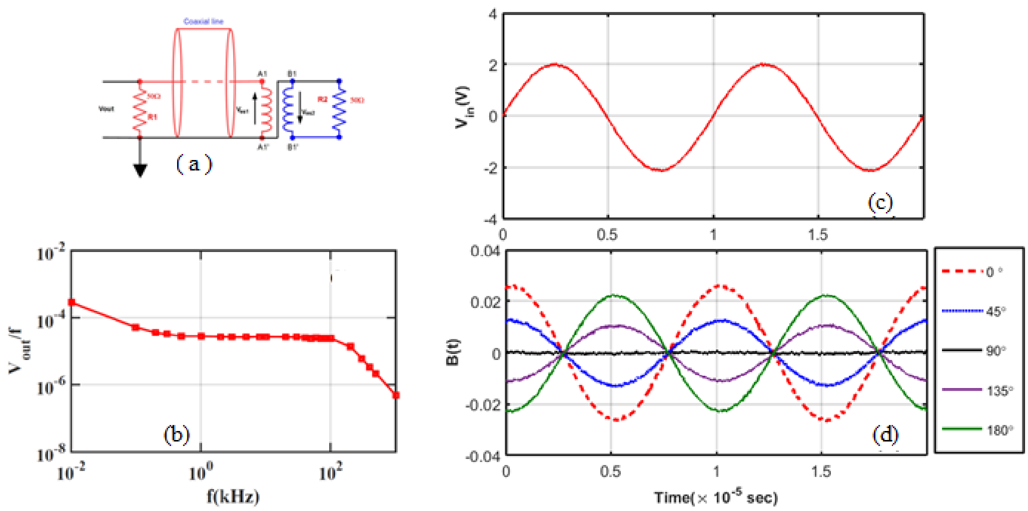

Figure 2.23. The electrical equivalent of the B-dot circuit is shown in (a). The probe eliminates capacitive effects by following the expression $V_{out}=V_{A1A1'}-V_{B1B1'}=V_{ind1}+V_{es1}-(-V_{ind2}+V_{es2})$. Almost flat frequency response is observed in (b) for the probe for frequency between 1-100 kHz. The input signal fed to the Helmholtz probe is shown in (c) and inductive responses of B-dot probe obtained for different orientations w.r.t. the Helmholtz magnetic field are shown in (d).

2.5.5 Directional Langmuir Probe (DP)

A directional Langmuir probe is an ordinary Langmuir probe with shielding provided by insulating structure [Figure 2.24]. The shielding restricts the solid angle through which the probe collects particles. The directional Langmuir probe is useful in direct measurement of particle flux in any particular direction [66,67].

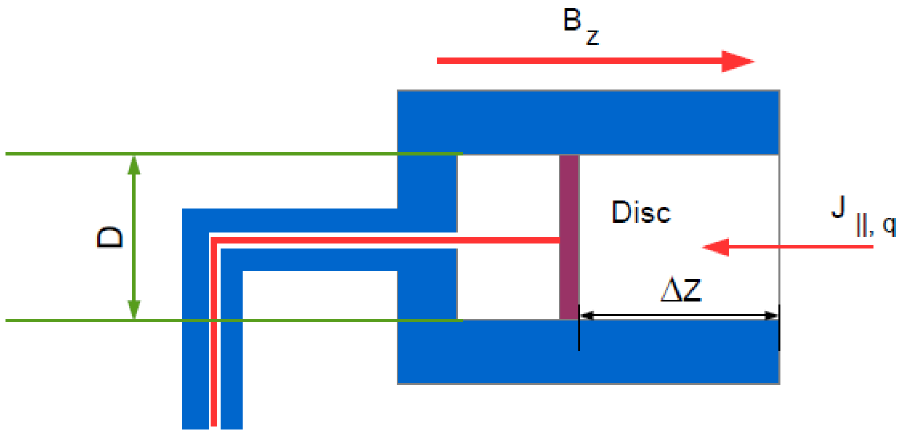

Figure 2.24. Schematic of the directional probe used for the measurement of parallel electron and ion current respectively. Blue color shows the ceramic material.

For the measurement of ion current, it collects the component of ion-saturation current along the particular direction of the flow velocity. One can determine the ion flow velocity in any particular direction by the ion-saturation current measurement in two opposite direction, as the current is different in the two opposite directions if flow exists. The simplified expression for flow velocity determination is $M = \frac{v}{c_s} = \frac{1}{\alpha}\frac{I(\theta+\pi)-I(\theta)}{I(\theta+\pi)+I(\theta)}$, where M is Mach number and α is calibration factor. The directional probe technique is also utilized for the measurement of parallel electron current, $\delta J_{\parallel,e}$ and ion current density fluctuations, $\delta J_{\parallel i}$ for determining the electromagnetic particle flux, which is given by $\Gamma_{em}^{q} = \frac{1}{qB} < \delta J_{\parallel,q}\, \delta B_x >$.

2.5.6 Emissive Probe

Emissive probe is a floating heated Langmuir probe. It is used for measuring locally the mean plasma potential, ϕ_p and its fluctuations, $\delta\phi_p$. Emissive probe is based on floating potential, ϕ_f measurement, which in plasma correlates the local plasma potential, ϕ_p and electron temperature, T_e by the expression, $\phi_f = \phi_p - \mu T_e$, where μ depends on electron and ion saturation current of plasma [68].

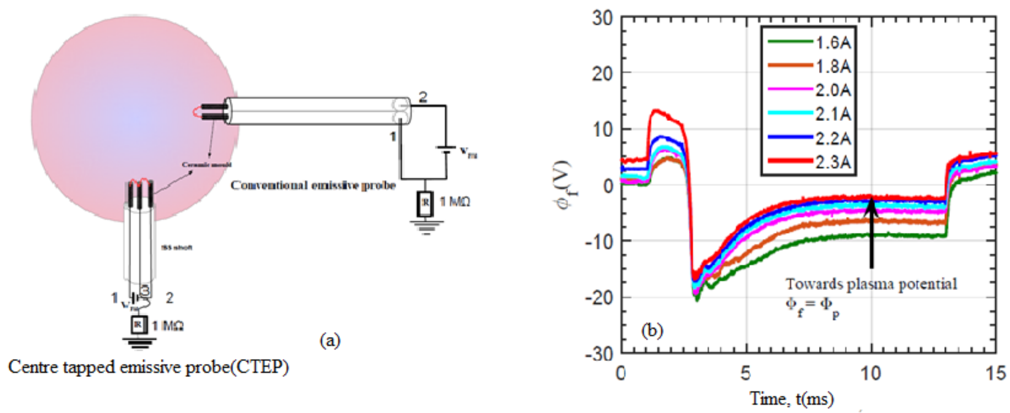

Figure 2.25. (a) Schematic of emissive probe assembly showing both conventional and centre tapped configurations and (b) floating potential variation with different heating current of emissive probe to get the correct plasma potential value.

In general for heated probe, the floating potential can be related to plasma potential by the expression, $\Phi_f = \Phi_p - T_e \ln \frac{I_{es}}{I_{is}+I_{em}}$, here $I_{es}$and I_{is} are electron and ion saturation current respectively. The I_{em} is the emitting electron current from heated probe. When emitting current is sufficiently high then $I_{is} + I_{em} \approx I_{es}$, the floating potential of heated probe thus becomes equivalent to local plasma potential. In LVPD, we have used the centre tapped emissive probe, which is capable of measuring real time plasma potential.

2.5.7 Microwave Interferometry

For target plasma of LVPD, we have developed a facility as shown in Figure 2.26 to measure chord averaged plasma density by using microwave interferometry diagnostics [69]. The whole purpose behind developing this residential diagnostic is to monitor regularly the plasma density formation after every vacuum break of LVPD. As target plasma has comparatively less plasma density than source plasma hence glow discharge cleaning takes longer time to bring back the wall conditions in the target region, hence direct monitoring of plasma density is very useful during this phase, which is done by using the microwave diagnostics. This technique uses the modification in the free space propagation of electromagnetic wave due to electrical properties of the plasma and measures the plasma refractive index. In this technique, power from a single source of monochromatic electromagnetic radiation is splitted into two parts. After traveling equal optical length both waves recombines to produce an interference pattern. When used for plasma, one of the wave traverses through it. This introduces a path difference in the two arms, which resulted in the distortion in the interference pattern obtained without plasma. A proper analysis of phase shift from initial fringe can provide information about the plasma density.

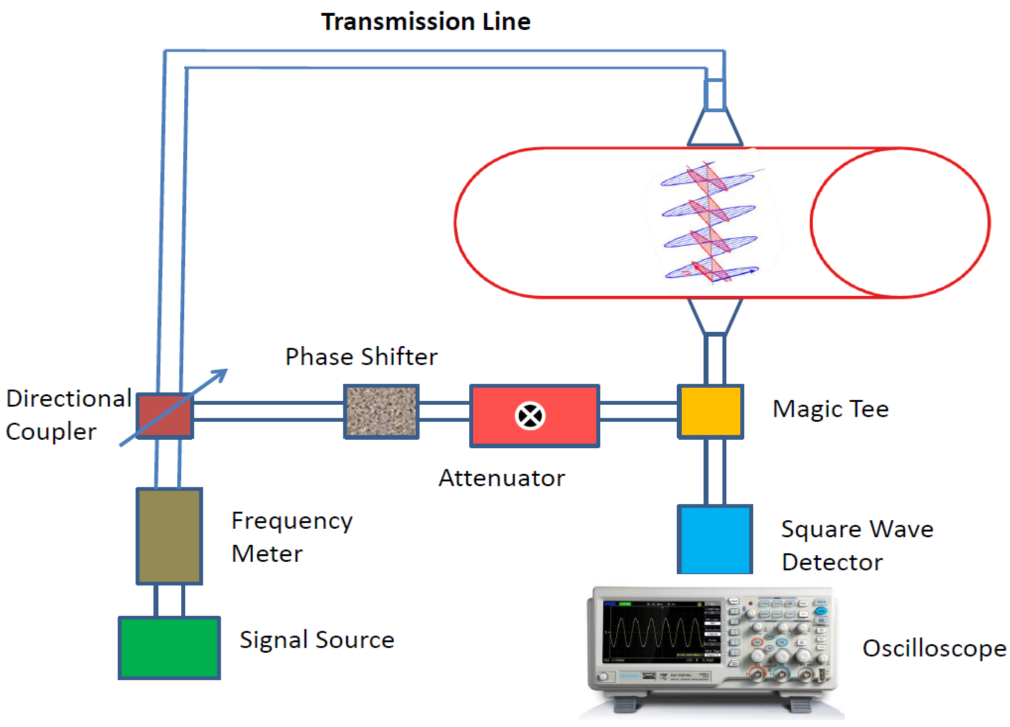

Figure 2.26. Schematic of a microwave interferometry system for chord averaged density measurement in target plasma.

Mathematically this can be represented by considering two-beam interference. Here, monochromatic field $E_1 \exp i\omega t$ and $E_2 \exp i(\omega t + \Phi)$ are added together, with some phase difference Φ between them. In plasma this phase difference is introduced by plasma itself. The total field can be given by, $E_t = (E_1 + E_2 \exp i\Phi) \exp i\omega t$. The power detected, by a square law detector is proportional to $|E_t|^2$, which is given by

$$|E_t|^2 = ({E^2}_1 + {E^2}_2)\left[1 + \frac{2E_1E_2}{E_1^2 + E_2^2}\cos\Phi\right]$$

The output intensity consists of a DC part and a varying part with dependency on $\cos\Phi$. The phase difference information is thus extracted from the measured intensity which caters for the line averaged plasma density with appropriate selection of conversion factor. In plasma, refractive index, N is defined by $N^2 = 1 - \omega_p^2 / \omega$, where $\omega_p = \sqrt{n_o e^2 / m\epsilon_o}$ plasma frequency and $\omega;$ is wave propagating though the plasma. The phase difference in plasma can be expressed in terms of refractive index as $\Delta\Phi = \int (N-1)\frac{\omega}{c} dl$ and subsequently this can be related to plasma density, $\Delta\Phi = -\frac{\omega}{2cn_c}\int n_e \, dl$, where $n_e = \omega^2 / m\epsilon_o e^2$. This gives information about the chord averaged plasma density.

In the design of μ-wave interferometry for LVPD, we have primarily focussed on two parameters namely, 1) the required source frequency and 2) the expected plasma density. The estimation of source frequency is carried out by using the expression of plasma frequency, $\omega_p^2 = n_e e^2 / \varepsilon_0 m$, where $\varepsilon_0 = 8.54 \times 10^{-12} F/m$, ω_p; the plasma frequency, m , the mass of electron, and $e = 1.6 \times 10^{-19} C$; the charge of electron. The plasma frequency becomes, $f_p = 8.983\sqrt{n_e} GHz$. For $n_e = 1 \times 10^{12} cm^{-3}$, the obtained plasma frequency is $f_p = 9 GHz$. We have thus chosen the source frequency as three times the plasma frequency i.e., $f_0 = 22 GHz$.

The density is estimated from $n_e = 2\omega m_e c \varepsilon_0 \phi / e^2 L$ which reduces to $n_e = 1.183 f\phi \times 10^6 / L$ at $f = 22 GHz$. For a plasma column of cross-sectional length of 2m, the final expression correlating density with phase shift assumes becomes $n_e = 1/3 \times 10^{16}\phi$, where ϕ is expressed in radians. Investigations are carried out in

LVPD for calibrating the performance of the diagnostics for different plasma densities. The varying plasma densities are obtained by controlling the emission from the filamentary source. We have kept the ambient magnetic field same so that nature of plasma should not change. The result in Figure 2.27 suggests that using this diagnostics, we can resolve fringes correspond to a plasma density of $n_e \sim 10^{10}$ cm^{-3}.

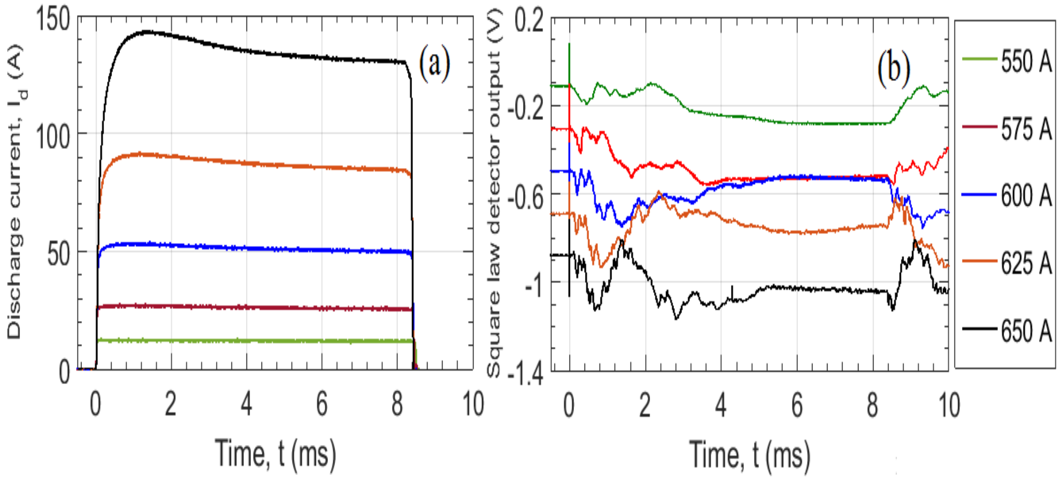

Figure 2.27. (a) Shows the variation of discharge current for different filament emission and (b) the measured microwave interferometry signal with different discharge currents. An arbitrary shift is given to each signal for visualization of detector output signals.

2.6 Linear probe drive

An automated electro-mechanical linear drive system for the positioning of the plasma diagnostics has been designed and implemented in LVPD [70]. In total 12 electro-mechanical assemblies, which are orchestrated using the Modbus communication protocol on 4-wire RS485 communications to meet the experimental requirements.

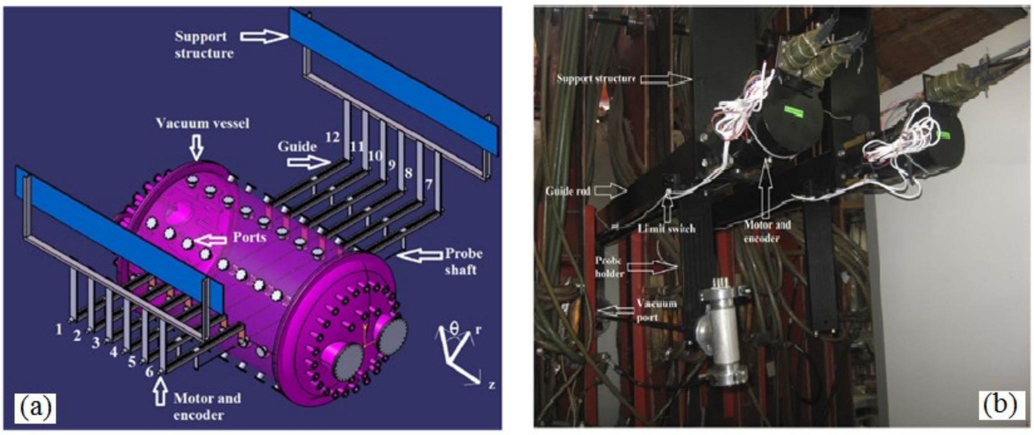

Figure 2.28. (a) Schematic of LPD mounted in LVPD to install diagnostics for radial measurements and (b) the photograph of a pair of LPD mounted in the device.

The mechanical assembly has two components: (i) lead screw-based structure and (ii) Wilson feed-through-based probe shaft assembly. Figure 2.28 (a) shows the schematic of these 12 numbers of electromechanical probe drives fixed to the LVPD and Figure 2.28 (b) shows the photograph of a pair of installed LPD in the horizontal plane. The lead screw assembly (L = 1500 mm) comprises of two parallel running support structures (Aluminium) having a guide “V” groove to guide the movable nut in a horizontal plane. The “V” grooved support channel is having a length of 1500 mm, with rectangular cross section 60 mm × 25 mm. The “V” groove angle is fabricated with a triangle point smoothened, and the angle is maintained at 60 °. The rectangular nut made out of an Aluminium block having a “V” type protrusion is accommodated between the parallel support structures and has inner threading matched to the pitch of the lead screw. The parallel support structures are bolted with flat plate lead screw arrestors (Aluminium) at both ends. Flat support plate arrestors are designed with a spacer washer (SS304) and non-magnetic bearing housing. The inner diameter of the bearing housing is matched with the unthreaded end leads of the lead screw.

The device end of the arrestor plate is curved at one end, and holes on it (ϕ = 9 mm) are matched with the holes of pre-existing diagnostic posts on a pitch centre distance (145 mm). The tail end of the arrestor plate is used to generate wall mountable support from the roof top for the electromechanical assembly. The stepper motor assembly along with the encoder unit is mounted horizontally on the tail end arrestor plate. The lead screw is made of SS304 and is connected to the non-magnetic bearing at two ends. The housing of bearings passes through the rectangular guide nut along the length of the probe drives structure. The screw is a trapezoidal ACME13 (American Acme general purpose thread, ref. American national Standards (ANSI/ASME B1.5)) threaded rod (ϕ = 25.6 mm, L = 1500 mm). In order to move larger distances in the z direction in reasonable time without sacrificing the positional accuracy, the pitch of the screw is selected as 5 threads per inch (TPI). The lead screw is housed in the lead screw arrestor plates. The screw is supported by the ball bearings at the ends. The motor is coupled to the probe drive lead screw with a metal-rubber bushing assembly so that initial torque is not directly transferred to the lead screw.

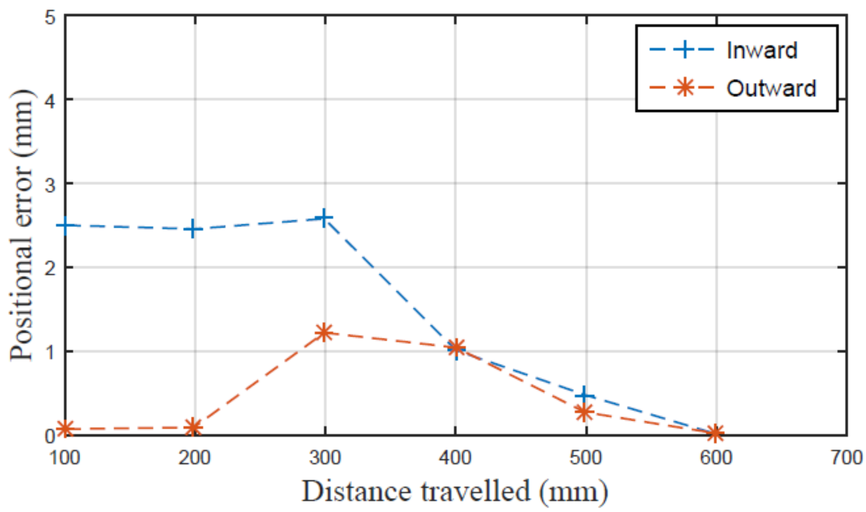

Figure 2.29. Positional error measured due to backlash between the travelling nut and the lead screw showing accuracies better than 3 mm measured for total travel length of 600 mm.

The lead screw is lubricated with silicon grease for its smooth operation. The limit switches are mounted at two ends to set the desired maximum forward and backward travel lengths for the probe shaft, and for providing additional safety to the diagnostics. The effective travel length thus becomes of 1000 mm or less, as desired. The performance of the LPD is shown in Figure 2.29**.**

A vacuum interface to the probe shaft is provided through the Wilson feed-through, mounted directly to the diagnostic port. The end to end vacuum interface is matched with a 40KF coupler. The vacuum interface has been tested for a leak rate better than$10^{-7} mbar$. The atmospheric end of the probe shaft is connected to the BNC-based vacuum compatible instrumentation feed through for taking a probe signal. The alignment and calibration of the mechanical system are carried out to ensure the smooth linear motion of the probe shaft. The pitch of the lead screw is needed as an input to the software for exactly calculating the number of rotations required for the linear motion of the probe within the vacuum vessel. The probe shaft moves through the horizontal port, perpendicular to the device magnetic axis. The horizontal axis of the probe shaft is maintained by two point supports at (1) the Wilson feed through and (2) probe shaft holder plate.

2.7 Spectral analysis and data acquisition system

2.7.1 Spectral analysis

The spectral analysis for the thesis work is performed to identify the nature of turbulence by determining frequency band, wave number, cross correlation, cross power, coherency, and phase angle of observed fluctuations in different plasma parameters.

2.7.1.1 Frequency power spectrum

The technique of frequency spectrum are well developed in past. In short, if $g_1(t)$ and $g_2(t)$ are representing two fluctuation quantity which are simultaneously measured at two location r_1 and r_2. The observed fluctuations can be written as Fourier superposition as $g_1(t) = \int_{-\infty}^{\infty} G_1(f) e^{i(2\pi f t - \vec{k}.\vec{r_1})} df$ & $g_2(t) = \int_{-\infty}^{\infty} G_2(f) e^{i(2\pi f t - \vec{k}.\vec{r_2})} df$, where $\overrightarrow{k(f)}$ is the wave vector as a function of frequency or the dispersion relation of the system. The Fourier transform of the fluctuations can be written as $G_1(f) = G_o(f) e^{-ik.r_1}$ and $G_2(f) = G_o(f) e^{-ik.r_2}$ .Computing the cross power spectral density function$P_{12}(f)$, we find that $P_{12}(f) = G_1^*(f)G_2(f) = |G_o(f)|^2 e^{-ik(f).\Delta r}$, where $\Delta r = r_1 - r_2$ is known as vector distance of the separation of two points where fluctuations are measured. The absolute value of cross-power and phase is given by $|P_{12}(f)| = |G_o(f)|^2$and $\Theta_{12}(f) = k(f).\Delta r$. The wave number is then calculated from the phase such that, $k(f) = \frac{\Theta_{12}(f)}{\Delta r}$. We have used covariance for the analysis, which is defined in terms of the auto and cross power spectrum as follow; $\gamma_{12} = \frac{|P_{12}(f)|}{\sqrt{P_{11}(f)P_{22}(f)}}$. It is the degree of cross-correlation between $g_1(t)$ and $g_2(t)$ at each frequency and if $|\gamma_{12}(f)|$ is zero at a particular frequency then it signals incoherency at that frequency. Similarly, if $|\gamma_{12}(f)| = 1$ then $g_1(t)$ and $g_2(t)$are coherent for a given f and if $0 < \gamma_{12} < 1$ then the signals $g_1(t)$ and $g_2(t)$ are partially coherent at that frequency. This is also a measure of signal to noise ratio. The presence of background noise reduces the coherence to < 1.

2.7.1.2 Wavenumber frequency spectrum

The wavenumber spectrum technique is developed based on the work of Beall et. al. [71]. Following this technique, we have used the large fluctuations data for ion saturation current and potential fluctuations from a pair of closely separated probes. It determine the power distribution of fluctuation data for each k and f simultaneously which is represented as $\mathrm{S(k,f)}$. In the technique determining wave-number spectrum, M ensembles of length T provides discrete sample spectra of elementary band with $\Delta\omega = 2\pi/\mathrm{T}$, which is computed for each record. Each record consists of N samples of fluctuations data for each probe. The sampling interval $\Delta\mathrm{t} = \mathrm{T/N}$ must be short enough so that the Nyquist frequency must be greater than the highest frequency of any significant frequency components to avoid aliasing in FFT in time.

The sample cross spectrum is determined by the auto power of two probe signal for each ensemble $P_{12}(\Delta x, \omega) = G_{11}^{*}(x_1, \omega)G_{22}(x_2, \omega) \ = C(\omega) + iQ(\omega)$, then the sample wave number is given by$k(\omega) = \frac{\Theta(\omega)}{\Delta x}$,where $\Theta(\omega) = \tan^{-1}[\frac{Q(\omega)}{C(\omega)}]$.The maximum wave number will be limited by the separation, Δx, which is $-\frac{\pi}{\Delta x} < k_{max} < \frac{\pi}{\Delta x}$. The local wavenumber and frequency spectra $S_l(K, \omega)$ is computed by summing the sample power values $P^i(\omega)$ at a fixed frequency from those records which have a sampled local wavenumber in the range K to $K + \Delta K$ and dividing by M; $S_l(K, \omega) = \frac{1}{M}\sum_{j=1} I_{|0,\Delta K|}[K - K(\omega)] \times \frac{1}{2}[P_1(\omega) + P_2(\omega)]$, where $I_{[0,\Delta K]}(K - K(\omega)) = \begin{bmatrix} 1, & K \leq K(\omega) \leq K + \Delta K \\ 0, & otherwise \end{bmatrix}$.These procedural steps are followed for all set of ensembles of large data sets and statistical averaging is performed. The procedure followed here yields the local wavenumber spectral density, $S(k, f)$ which yields several important observables.

2.7.2 Data acquisition system

The physics experiments require capable support from data acquisition system (DAQ) to understand complex plasma processes taking place within the device. During the thesis work, a new data acquisition system has been procured and integrated. The system is designed to handle requirements of LVPD system but it is generic enough to be used in multipurpose laboratory plasma experiments. The adopted tools and techniques are useful contribution in the area of machine control system development. The complexity of design is discussed in following section with adopted hardware and software solutions.

2.7.2.1 Requirements

2.7.2.1.1 Physics requirements

Physics problems ranging from the excitation of whistler structures to plasma turbulence, especially, exploring the linear and non- linear aspects of electron temperature gradient driven turbulence and plasma transport across entire cross section of device has been proposed. Pursuit of producing plasma devoid of energetic electrons and to exert a control on electron temperature gradient, the electron energy filter (EEF), a variable aspect ratio solenoid which divides plasma into three distinct regions has been installed. The plasma conditions in the three regions are quite different from each other. Further carrying out investigation over entire cross section of LVPD, the exciting problem of plasma transport (using streamers, zonal flow etc.), non-linear structures in background of ETG and understanding of role of energetic electrons and their loss mechanism, require data from large number of diagnostics simultaneously. The large sized plasma of LVPD and existence of three distinct plasma regions have not only scaled up the diagnostic requirements but also enhanced the sampling rate and record length requirements of the measurement system for better understanding of spectral characteristics of the excited turbulence.

To carry out these investigations, proper interfacing of the instrument and reconstruction of the signals generated by the diagnostics is needed. The required diagnostics are classified into two categories for making DC and turbulent signal measurements. First category is of resident diagnostics, where equilibrium plasma parameters are measured whereas second category handles those diagnostics which are dedicated for measuring the fluctuating signals. The measurements under former category are limited to a frequency range of ≤ 150 kHz, hence DAC system cards are chosen with sampling rate of ≥ 5 MHz while for later category signals, the sampling requirements are met by signal cards having frequency response of ≥ 150 MHz respectively. One of the important requirements of any data acquisition system is its capability of resolving the signal amplitude. In LVPD, this requirement is essentially felt while estimating the mean temperature and temperature fluctuations. The temperature is estimated from the I/V curve which gives a measure of ion to electron current in a single sweep of bias to Langmuir probe. It addresses a large signal variation in probe current in a single sweep to the Langmuir probe. The probe current typically varies from 100 µA (5 mV) to 50 mA (2.5 V) respectively. This requires a data acquisition system with good digitization capability. To sample fluctuations, it is required that in each single I/V sweep, the probe current should undergoes sampling for at least 1000 times to extract a meaningful intelligence from the data acquired. Thus the minimum sampling rate required for such measurements should be ≥ 150 MHz. Beside this, factors like redundancy, availability of on board memory, administrative, service, support, available technology choices and economic factors are considered while making selection for the appropriate instrumentation cards of DAC system. In summary, the key signal requirements are summarized as follows: 1) 32 single ended channels with sampling rate of ≥ 5 MHz, 12 bit and 2) for resolving signals for temperature, 8 single ended channels with sampling rate of ≥ 150 MHz, 10 or 12 bit respectively.

2.7.2.1.2 Operational requirements

The device operates in the pulse mode (single or multiple pulses) with repetition cycle of 1 Hz. This implies that in every second, plasma discharge is produced and the data is acquired from the diagnostics signals. This limitation arises due to heat handling capacity of the vacuum vessel. The pulse duration is decided by the capacity of the discharge power supply. The discharge power supply duration is kept $9.2ms$. We acquired signals with sufficient pre and post trigger margins ($\sim 2.5ms$) to assist analysis. Total acquisition duration is $\sim 15ms$. The data acquisition system must be able to strike $8-10$ discharges in burst mode, this leads to the acquisition length of > 100 ms. In this thesis, we focused on data acquisition system leaving aside discussion related to operation of other subsystems such as magnet coils, power supplies, vacuum production system etc. which was already referred in the past by other researchers.

2.7.2.2 System description

The device offers large access facility through multiple diagnostics ports (~94) where each port is equipped with variety of diagnostics. It lays down the design requirement of a high channel count system. It is challenging as firstly, it leads to the synchronization in terms of timing and data access among different I/O boards. Secondly, complexity due to the signal characteristic pattern originated from various plasma diagnostics which thus requires suitable selection of hardware's. The hardware includes signal conditioning and host controller having multiple I/O boards. Thirdly, the voluminous data management across shared instrumentation bus hosting multiple boards requires specialized hardware and software solutions. A state of art data acquisition system has been implemented using PXIe instrumentation bus based hardware. The PXIe system has capability to measure 32 signals at maximum 60 MHz sampling and 8 signals at maximum 1.25 GHz sampling frequency. This system has successfully demonstrated the solution of design issues concerning high channel count, high speed data acquisition, data streaming and multi board synchronization.

(a) Hardware solution

The PXIe stands for PCI bus for instrumentation. It is a high speed parallel bus providing 6 GB/s shared data bandwidth across multiple hardware boards. It is available in 3U size and can be accommodated in standard 19” rack. Used hardware solution is described in Table 1.

Table 2.1. The hardware solutions used for the development of LVPD data acquisition system.

Hardware item	**Model/ Make**	**Specifications / Description**
Chassis (1 No.)	NI PXIe 1085	19”, Hybrid chassis
Controller (1 No.)	NI PXIe 8135	Intel 7 controller, 8GB RAM, 250GB
Acquisition board type 1 (4 Nos.)	NI PXIe 5105	60MS/sec, 12 bit, 50Ω and 1MΩ, External Triggering
Acquisition board type 2 (2 Nos.)	NI PXIe 5162	1.25 GS/sec, 10 bit,50Ω and 1MΩ, External Triggering
Timing and Synchronization board (1 Nos.)	NI PXIe 6674T	On board clock synchronization
Local Storage solutions		
Interfacing controller card	NI PXIe 8348	PXIe based RAID controller
RAID hard disk	NI HDD 8266	3 TB RAID (24 disk of 146 GB each)

The testing of the data acquisition system involves standalone and integrated testing of each board. Firstly, in the standalone testing mode, the characteristic parameters of each board is tested to verify compliance to the specifications using in-house developed software. Secondly, the integrated performance of the system is verified using signals received from signal generator source. Subsequently, the system is integrated to the centralized signal conditioning hardware which feeds signals from real world diagnostic equipment's. We found that system is performing to the criteria laid down.

(b) Software solution

The software is designed in-house for single or multiple pulse operation of the device. It is completely configurable and generic enough for multipurpose laboratory plasma investigations. The software design is complex due to handling of multiple configurations and status registers (on boards), operating modes, synchronization, data access and transfer metaphors and inter-process communication mechanism involved. It is designed on specialized PXIe instrumentation bus and requires specialized libraries and communication methods. The software architecture is based on confluence of object oriented and data flow techniques of software engineering. It is novel in the hybrid architecture where object orientation in the upper layer facilitates reusability and maintainability whereas lower layer deals with the board configuration and handling using data flow mechanism. Software have an incremental testing approach in the design and testing. We have tabulated various tools and techniques used for its development in Table 2.2.

Table 2.2. Different software solutions used for the development of DAC are tabulated.

Control System Development Platform	
Win.7 Pro. Ser. pack 1	Windows OS is the specialized version for embedded controller.
LabVIEW 2014	LabVIEW is a control system development platform.
Libraries Used	
NI platform services	Driver libraries used by motherboards chips for PXIe controllers and boards.
NI Scope 14.0	It is library for high speed digitizer board handling.
NI Sync 14.5	It is library for timing and synchronization board handling.

In summary, the main features of the designed DAQ software are namely, 1) Configuration of each signal characteristic parameters such as termination resistance, signal range, volts per division etc., 2) Configuration of boards parameters such as selection, sampling frequency, record length etc., 3) Configuration of hardware or software triggering mechanism, pre and post pulse samples etc., 4) Visualization of single pulse or burst of pulses acquired by selected modules, 5) Graphical signal visualization and analysis facility, and 6) Load and save of configuration and acquired data.

The software follows pulsed acquisition logic which is represented by Figure 2.30. It reads the configuration data from user for each channel and the module initializes accordingly and waits for trigger. As soon as trigger received, the single or multiple pulse data in read and analysed by the user in online mode. If data is useful data then it is recorded on the local hardware storage.

There are two kinds of acquisition formats used. (a) .xml based format for loading and saving of the configuration data and (b) LabVIEW based binary (.tdms) file format for acquired data. The .xml format was chosen for compliance to standard and future use for configuration from any authorized PC on the IPR network. The binary format is a compressed format for archival of voluminous data. A separate utility has been developed for the transfer of data from tdms file to text files so that analysis can be carried out by data analysis software such as matlab, gnuplot etc.

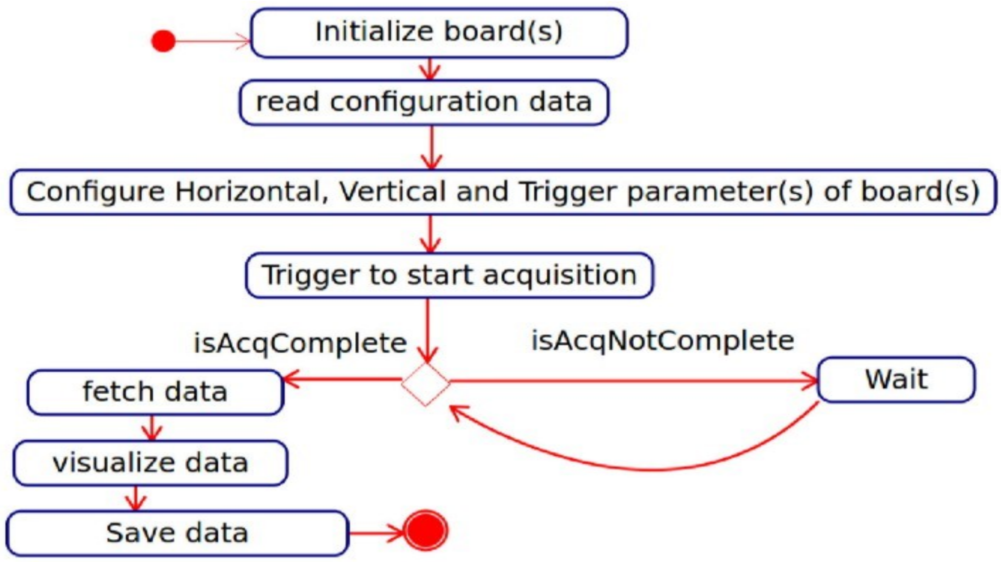

Figure 2.30. The schematic of the control logic of the developed software for DAQ system.

2.7.2.3 Developmental results

In order to test the integrated performance of the developed system, It is important to configure board and channels as represented by Figure 2.31.

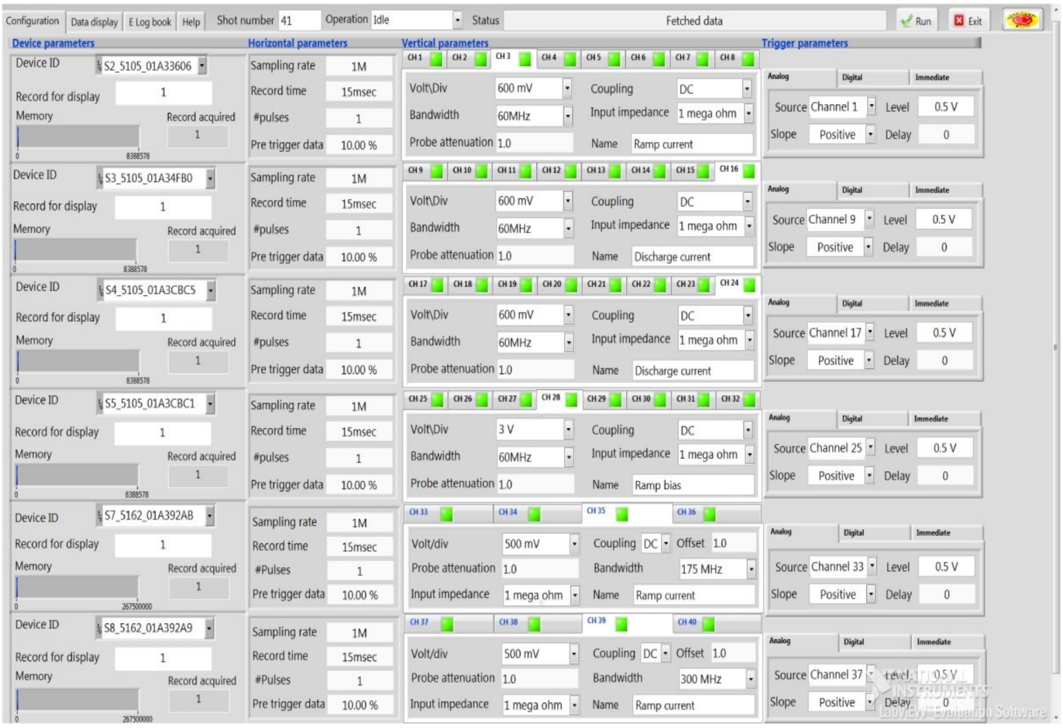

Figure 2.31. The I& C configuration user interface developed for DAC system.

The user interface shows a test case for 15 second pulse where all modules are connected. A typical plasma pulse acquired by PXIe based data acquisition system and subsequently transferred to the database server is represented by Figure 2.32. It shows that EEF solenoid pulse started before the discharge pulse and ended after discharge pulse. During the discharge duration, data is acquired using Langmuir probe diagnostics. The effort to auto transfer data into database in the recently procured high end data server hardware and automatic analysis software tasks are under process.

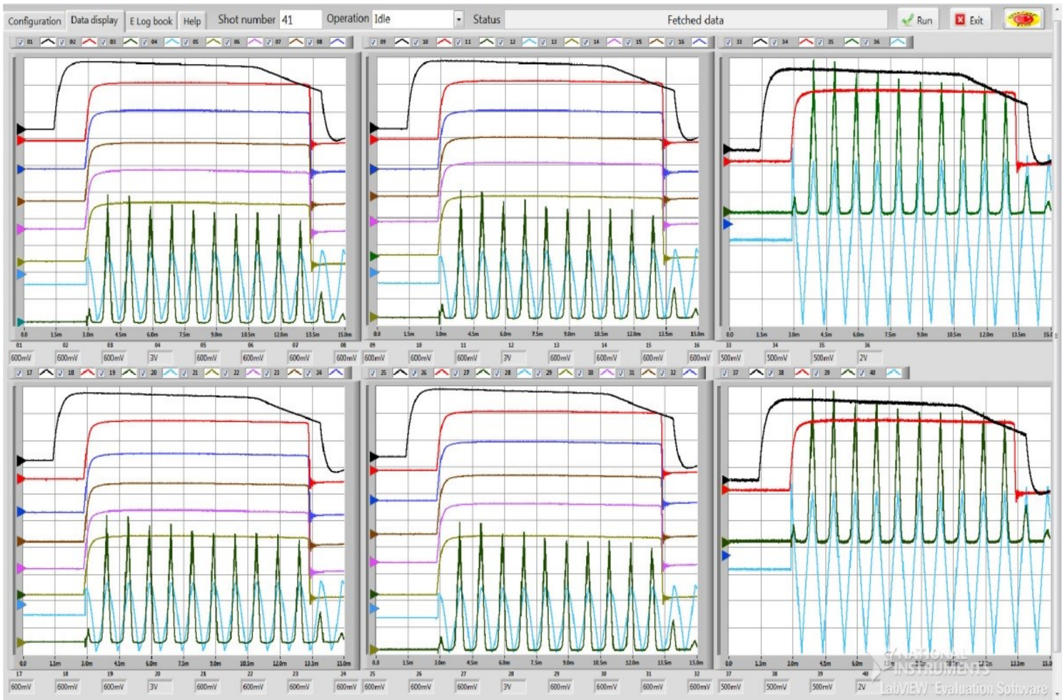

Figure 2.32. Graphical user interface to visualize data acquired by 40 channels (some channels are repetitively feed for the test).

Chapter 3
Experimental study of particle transport due to electrostatic fluctuations

3.1 Introduction

In this chapter, we have discussed the observations of turbulent particle flux in the core region of LVPD plasma due to presence of Electron Temperature Gradient (ETG) turbulence. Since plasma profile in EEF ON condition satisfied the background condition for ETG turbulence i.e., $\eta_{ETG} = L_n / L_{Te} > 2/3$,where L_n and L_{Te} are density and temperature gradient scale lengths, respectively, and observed fluctuations follows the frequency and wavenumber ordering of ETG mode**.** We have identified two extreme configurations of EEF, where in first one ETG turbulence is excited and in second one no signature of it is observed. The spectral features of the fluctuations such as power spectra, cross - correlation, $S(k,\omega)$ and the crucial relationship with plasma parameters are considered to characterize the ETG turbulence.

We compared the radial electrostatic particle flux with theoretical estimates derived from ETG model equations and provided a theoretical explanation for the observed flux. We found that particle flux results are due to the finite phase difference (deviated from 180°) between the density and potential fluctuation, for ETG mode.

The cross phase angle from the investigations agrees well with the cross phase angle due to the non-adiabatic ion response resulting from the wave particle resonance of the ETG mode with the ions. The flux obtained by this model is likely hybrid of pure diffusion and thermo-diffusion since it cannot be splitted distinctly into these two parts. However, in the core plasma where flat density exists, the flux becomes purely thermo-diffusive. Observations have shown the existence of particle pinch like scenario in core region of target plasma of LVPD due to inward radial transport of particle flux.

The remaining part of the chapter is organized as follows: The experimental setup and diagnostics are described in section 3.2. Identification of ETG turbulence is discussed in section 3.3. Section 3.4 describes the theoretical justification for ETG turbulence based on experimental observations. The plasma transport study with its theoretical explanation is presented in section 3.5. Finally, the summary and concluding remarks are given in section 3.6.

3.2 Experimental setup and diagnostics

The experimental setup primarily consists of: (1) the LVPD device [14], (2) the Electron Energy Filter (EEF) [15], (3) particle flux probes for diagnostics of electrostatic and electromagnetic fluctuations, and (4) the PXI based data acquisition system. The LVPD is a double walled, water cooled SS304 vacuum chamber having a diameter ~ 200 cm and length ~ 300 cm supplemented by a combination of rotary-root-diffstak vacuum pumps, capable of pumping the system to a base pressure of 2×10^{-6} mbar.

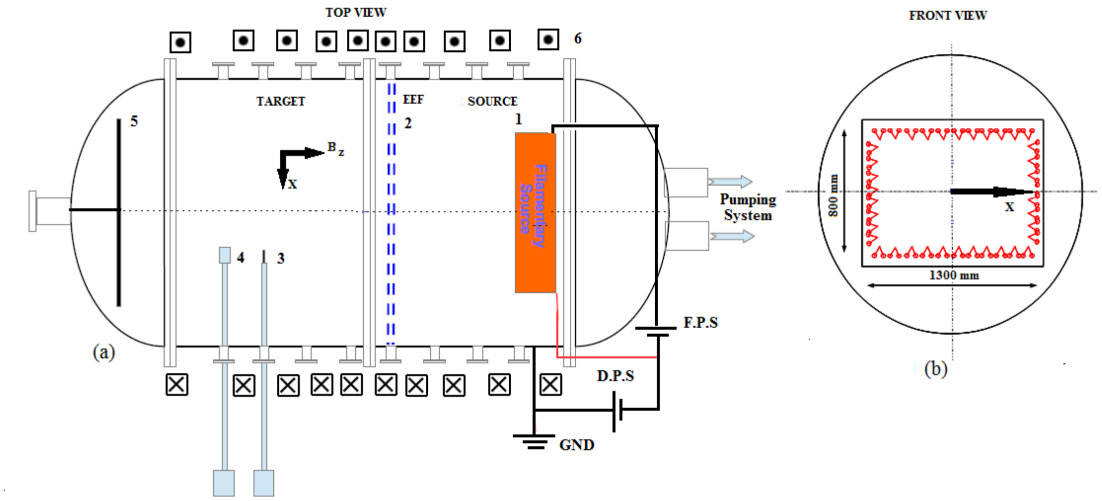

Figure 3.1. (a) Schematic diagram of experimental setup, the layout shows internal components marked as (1) back plate (2) EEF coil assembly (3) Langmuir Probe (4) a pair of B-dot and Langmuir probes (b) cross section view of LVPD showing the filament assembly arranged in a rectangular geometry (130 cm × 90 cm) in the source region.

The Electron Energy Filter (EEF) is a rectangular shaped varying aspect ratio solenoid consisting of 155 number of individual coils arranged in 19 sets and has a width of 4 cm. The EEF produces a uniform transverse magnetic field of $B_x \sim 160$ G with input current of 2 kA for an EEF activation length of 1 m (central 13 coils) [27]. EEF divides LVPD plasma into three distinct experimental regions namely, source, EEF and target plasmas. The source region embeds multi-filamentary plasma source, the EEF region is described by the plasma volume enclosed by the solenoid itself and the target region is the region between EEF and end plate. The cumulative effects of EEF are; firstly it restricts the energetic electrons in the source region and secondly, it reduces the electron temperature and plasma density in the target region because of the preferential transport of cold electrons due to collisions, in line with past research work of others [56,59,72,73].

The plasma source is a directly heated W- wire based multi- filamentary source with hairpin shaped filaments ($n = 36, \phi = 0.05\ cm, l = 18\ cm$) arranged on the periphery of a rectangle ($130\,cm \times 80\,cm$) back plate [Figure 3.1 (b)]. Pulsed plasma (Argon gas, $P_{Ar} \sim 4\times10^{-4}\,mbar$ and $\Delta t_{discharge} = 9.2ms$) is produced by applying a discharge voltage of 70 V between the plasma source and anode (vacuum vessel) in a coupled axial magnetic field comprises of $B_z = -6.2G$, produced by 10 garlanded coils on LVPD and $B_x \sim 160G$, produced by EEF for the duration of $12ms$ by the use of in-house developed 5kA pulsed power supply [52].

The experiments are carried out in target region where Electron Temperature Gradient (ETG) relevant plasma conditions are satisfied that includes presence of finite electron temperature fluctuations. Plasma parameters are measured by using Langmuir and B-dot probes. The plasma potential ϕ_P is measured by using a hot emissive probe [68,74]. The electron temperature T_e is determined from the *I-V* characteristic of the Langmuir probe. The azimuthal wavelength and phase velocity of the mode are measured by an array of cylindrical Langmuir probes (n = 5, ϕ =0.08 cm, l = 0.8 cm and poloidal separation, Δy = 0.5 cm) mounted on a radially movable shaft [70]. The fluctuation data and mean parameters are recorded at sampling rates of 500 kS/s and subjected to band pass filter ($300\,\text{Hz} \le f \le 300\ \text{kHz}$) respectively. Schematic of the various probe assemblies utilized to perform the experiments are shown in Figure 3.2.

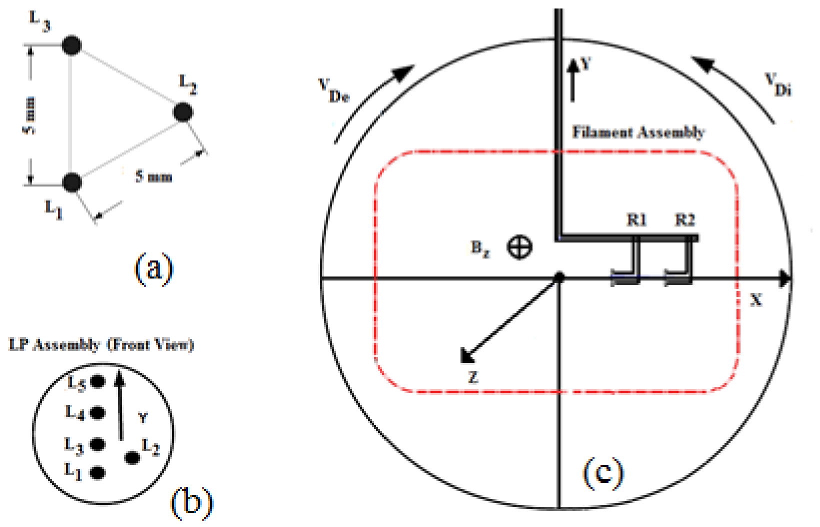

Figure 3.2. (a) Three single Langmuir probe assembly for simultaneous measurement of floating potential and plasma density fluctuations, (b) probe configuration for S(k_y, ω) spectra measurements and (c) probe assembly mounted from the top port of LVPD for simultaneous measurements of particle flux at two different radial locations.

The electrostatic radial particle flux is measured by using a specially designed three single Langmuir probe assembly in 'Δ' configuration with length of the vertices as, d = 0.5 cm. In this configuration, two probes separated vertically ($L1$ & $L3$) measures the floating potential fluctuations ($\delta\phi_f$) and the third probe ($L2$) intercepting a different magnetic field line is used for measuring the density fluctuations (δn_e). We have also configured another probe assembly with two vertically separated emissive probes in order to measure the plasma potential fluctuations ($\delta\phi_P$) directly. This exercise is carried out to see the effect of temperature fluctuations (δT_e) over the measurement of potential fluctuations. The ion saturation current signal is obtained by biasing the probe at $-80V$, and the floating potential measurements are carried out with floating probes terminated across a high impedance ($1M\Omega$). The large data length of more than 2×10^5 data points is used for power spectral analysis and is obtained from the ensemble of approximately 100 identical plasma discharges. The data series is constructed by extracting 1024 data points from the steady state period of $6ms-8ms$ from each plasma discharge. This data is segmented into 200 bins of 1024 data points each for obtaining a higher frequency resolution in spectral analysis.

The data acquired for different parameters is captured in PXI based 40 channel fast data acquisition system. Out of total 40 channels, 32 are single ended channels with maximum sampling rate of $60MS/s$, digitization rate of 10 bit, and record length of 250 k points and 8 single ended channels with maximum sampling rate of $1.25GS/s$, digitization rate of 12 bit and a record length of 12 M points. The data is retrieved to local computers for post processing.

3.3 Identification of electron temperature gradient driven turbulence

Unambiguous measurement of plasma parameters, especially the electron temperature becomes necessary while addressing ETG turbulence but presence of energetic electrons poses serious concern to laboratory plasmas (RF, filamentary etc.), while making measurement of electron temperature. This diminishes hope of distinct identification of free energy source associated with the observed turbulence. We have therefore dressed the plasma for unambiguous measurement of electron temperature by using EEF. The EEF divides LVPD plasma into three different plasma regions. The source plasma embeds large population of energetic electrons, the EEF plasma is a low beta ($\beta \sim 10^{-3}$) sandwiched plasma between two high beta plasmas of the source ($\beta \sim 1.6$) and target ($\beta \sim 0.2$) regions [75]. The sandwiched EEF plasma region proposes a complex plasma scenario. We observed that energetic electrons are trapped in the mirror of the solenoid field of the EEF in the source plasma region of LVPD and no trace of these electrons is observed in the target region [27]. The transport across EEF magnetic field helps in producing a plasma profile suitable for the excitation of ETG instability, in axially far-off region, approximately 70 cm away from the EEF surface. A comparison of plasma parameters in the three regions is given in Table 3.1.

Table 3.1. The typical plasma parameters obtained in the target, EEF and source plasmas of LVPD.

Plasma Parameters			
	Source	**EEF**	**Target**
Plasma density, n_e (cm^{-3})	6.0×10^{11}	2.3×10^{11}	1×10^{11}
Electron Temperature, $T_e(eV)$	5.0	2.5	2.2
Plasma beta, β	1.6	10^{-3}	0.2
$f_{pe}(Hz)$	7×10^9	4.9×10^9	3.5×10^9
$f_{pi}(Hz)$	3×10^7	1.8×10^7	1.3×10^7
$f_{ce}(Hz)$	1.0×10^7	2.8×10^8	1.0×10^7
$f_{ci}(Hz)$	236	6×10^3	236
Electron-ion, $\nu_{ei}(s^{-1})$	$\sim 1 \times 10^5$	$\sim 4 \times 10^4$	$\sim 1 \times 10^4$
Debye length, $\lambda_D(cm)$	2.1×10^{-3}	2.3×10^{-3}	2.7×10^{-3}
Electron gyroradius, ρ_e (cm)	0.8	0.02	0.5
Ion gyro radius, ρ_i(cm)	73	2.2	46

3.3.1 Radial profiles: Plasma parameters and fluctuations

The plasma discharge pulse ($\Delta t \sim 9.2\ ms$) is produced and data from steady state region ($4\ \text{ms} \leq t < 9\ \text{ms}$) is captured from the onset of discharge. Radial profiles of basic plasma parameters and their fluctuations are shown in fig. 3.3 for EEF OFF and ON conditions. Target plasma in LVPD is divided into two distinct regions namely, (1) core ($x \leq 50\ \text{cm}$) and (2) edge ($x > 50\ \text{cm}$) respectively. In the core region, Figure 3.3(a) shows hollow plasma density profile for EEF OFF plasma but nearly flat profile for EEF ON plasma with typical gradient scale length, $L_n = \left[\frac{1}{n_e}\frac{dn}{dx}\right]^{-1} \sim 300$ cm. Figure 3.3(b) shows nearly flat electron temperature profile for EEF OFF plasma but radial electron temperature gradient exists for EEF ON plasma with typical gradient scale length, $L_{T_e} = \left[\frac{1}{n_e}\frac{dn}{dx}\right]^{-1} \sim 50$ cm . On the other hand, edge plasma exhibits finite gradient in plasma density and nearly flat electron temperature for EEF ON condition. Although, finite electron temperature gradient exits in the edge region for EEF OFF plasma and satisfies the gradient scale length threshold condition of ETG but due to the presence of energetic electrons, loses relevance for carrying out unambiguous ETG studies [22]. Figure 3.3(c) shows plasma potential profiles for EEF OFF and ON cases. EEF ON plasma shows negligible radial gradient in core region, suggesting absence of radial electric field ($E_x \approx 0$). Hence, $E \times B$ rotation in the core region can be safely neglected. A detailed characterization of the plasma with EEF was reported by S. K. Singh et al. [28], where various plasma scenarios satisfying ETG threshold condition for different imposed operational conditions of EEF is discussed.

The plasma equilibrium in EEF ON case can be understood in the following manner, electrons and ions remain confined in the core region. The plasma density gets flattened over the ion gyro scale, $\rho_i \sim 45cm$ while plasma electron temperature follows the electron gyro scale, $\rho_e \sim 0.5cm$ and thus offers significant gradient in the core region. In this region, the equilibrium is established with preferable movement of ions in radial direction and electrons along the field lines in z direction.

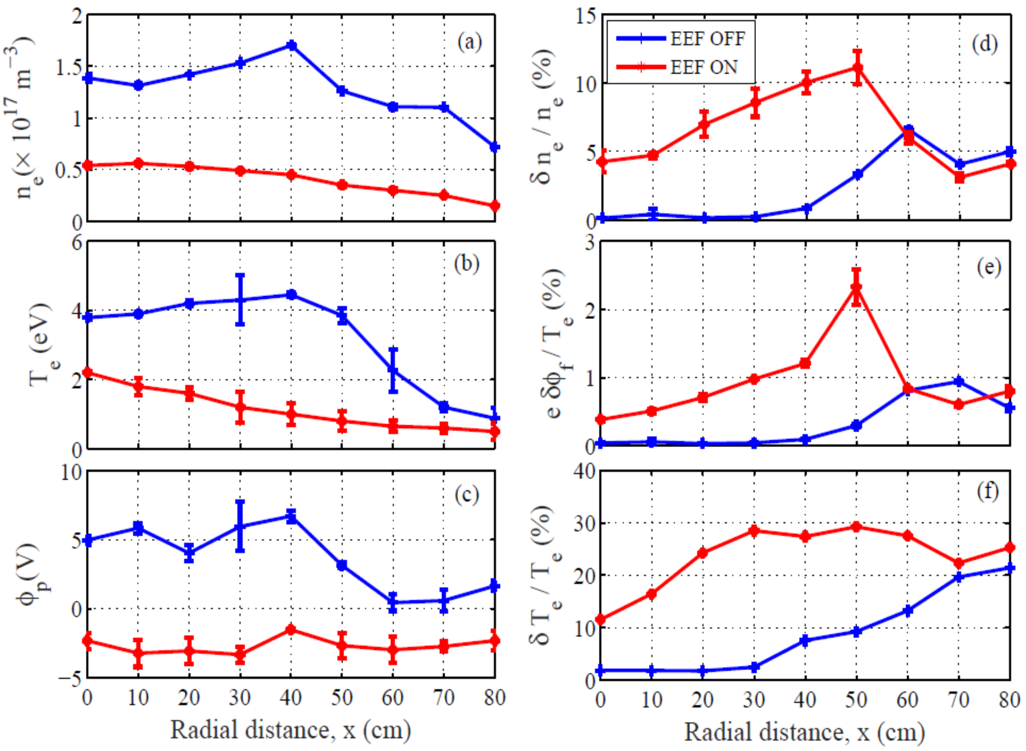

Figure 3.3. Comparison of radial profiles of mean plasma parameters is shown for, (a) plasma density, n_e, (b) electron temperature, T_e, (c) plasma potential, ϕ_p and fluctuations in (d) density, $\tilde{n} = \delta n_e / n_e$, (e) potential , $\tilde{\phi} = e\delta\phi / T_e$ and (f) electron temperature, $\tilde{T}_e = \delta T_e / T_e$ for EEF OFF and EEF ON cases.

The fluctuations in different plasma parameters, in the core region enhanced for EEF ON case. Observed fluctuations are subjected to various statistical techniques before investigating fluctuation induced particle flux in the core target plasma. Normalised fluctuations are measured radially for n_e, ϕ_f and T_e with typical values obtained for EEF ON plasma are $5\%-10\%$, $0.5\%-2.5\%$ and $10\%-30\%$ respectively [Figure 3.3 (d-f)] but for EEF OFF plasma, they reduced to near noise level. Edge region on the other hand exhibits enhanced level of fluctuation for both plasma conditions.

3.3.2 Spectral properties

In the core plasma, a comparison is made for the cross-correlation function of the normalized density and potential fluctuations [Figure 3.4]. Strong correlation with the correlation coefficient, $C_{n_e,\phi_f} \sim -0.8$ for EEF ON case but for EEF OFF case they remain uncorrelated. There may be a slight spatial de-correlation in the measurement of cross correlation coefficients as the probes used are not located on the same magnetic field line. Literature available on ETG mode suggests a strong anti-correlation for them [24].

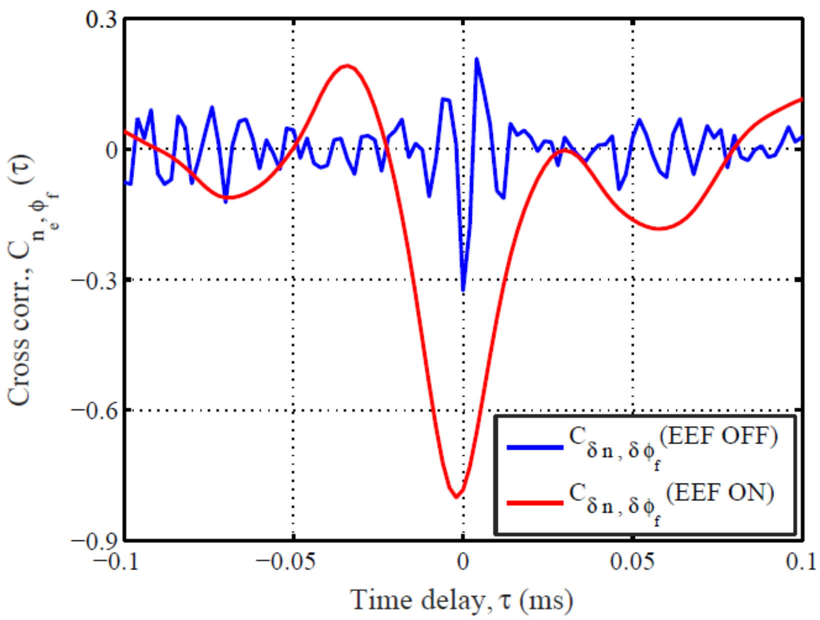

Figure 3.4. The cross-correlation coefficient, $C_{ne,\phi f}$ for density and potential fluctuations measured in the core region (x = 30 cm) of target plasma for EEF OFF and EEF ON conditions are shown.

The coherency and cross-phase angle between density and potential fluctuations are shown in Figure 3.5(a) and Figure 3.5(b). The degree of coherency is ~ 0.8 and is significant for the turbulence in the frequency band, $1\, kHz < f \leq 15\, kHz$. This corresponds to the finite cross phase angle which is deviated from $180°$. The corresponding auto power spectrum for density and potential fluctuations exhibits broad band nature [Figure 3.5(c)].

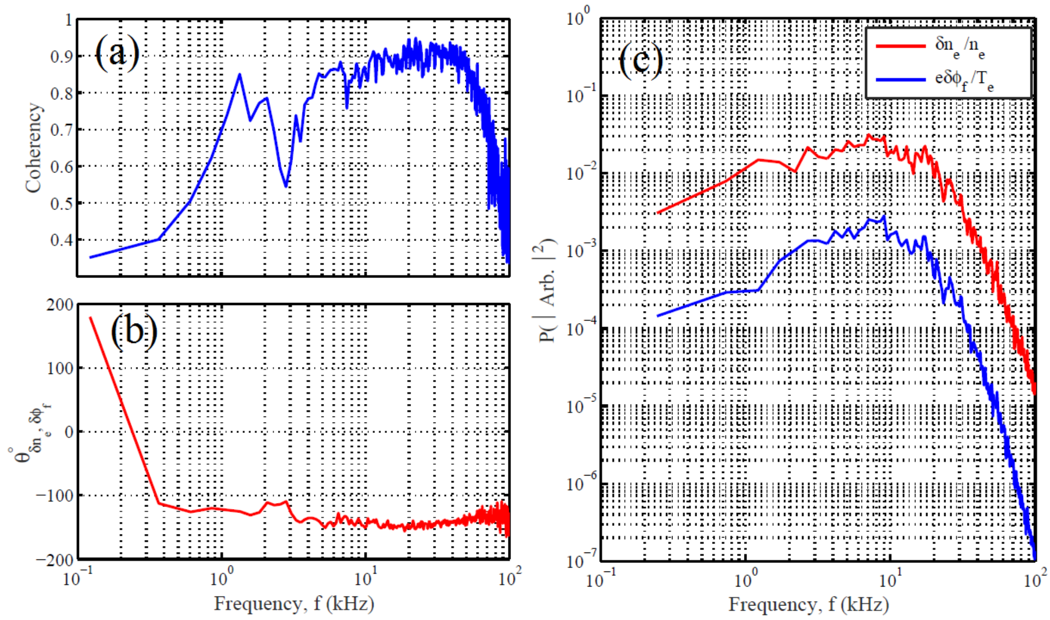

Figure 3.5. The figure shows (a) coherency, (b) Cross-phase angle, ($\theta_{n\text{-}\phi}$) plot and (c) the auto power for density (n_e) and potential (ϕ) fluctuations. The auto power spectrum exhibits broadband nature with significant power residing within $f \leq 15$ kHz These measurements are carried out for EEF ON case at $x = 30$ cm in target plasma.

The turbulence observed in the core plasma exhibits broadband spectra with significant power for $\leq 15kH_z$ (Figure 3.5(a)). As evident from the figure, the mode frequency, f falls in the lower hybrid range, between ion ($f_{ci} \sim 200Hz$) and electron cyclotron frequency ($f_{ce} \sim 17.5MHz$), $f_{ci} < f < f_{ce}$ with wave number ordering, $k_{\perp}\rho_e \leq 1$, $k_{\perp}\rho_i >> 1$ and $k_{\perp}V_{th,i} \geq \omega$ suggest that the instability driving the turbulence represents ETG mode, where, ρ_e and ρ_i are electron and ion gyro radius respectively and perpendicular wave number, $k_\perp \approx (0.1-0.4)\, cm^{-1}$. Here, $k_\perp = \sqrt{k_x^2 + k_y^2}$ for $k_x << k_y$, $k_\perp \sim |k_y|$, $V_{th,i}$ is the ion thermal speed and ω is the observed turbulence frequency. The joint wave number- frequency spectra, $S(k,\omega)$ for the density fluctuations is obtained by using the method proposed by Beall et. al [25] is shown in Figure 3.6(a). The spectrum exhibits $\Delta f / f \approx 1.8$, and $\Delta k / k \approx 2.2$ suggesting a broad band nature. The wave length of the propagating mode in poloidal direction is ~ 20 cm and corresponding phase velocity of the observed mode is, $v_{ph} \sim 10^5\, cm/s$. The radial phase velocity is measured using a pair of radially separated probes and it shows propagation from probe (2) to (1) i.e., radially inward with phase velocity, $v_x = -1.5\times 10^5\, cm/s$. Both probes are accommodated well within the radial correlation length (~ 20 cm) in the core region. Measurements were repeated at different radial locations in the core plasma and observed inward phase velocity. The measured poloidal and radial phase velocities of the turbulence are comparable.

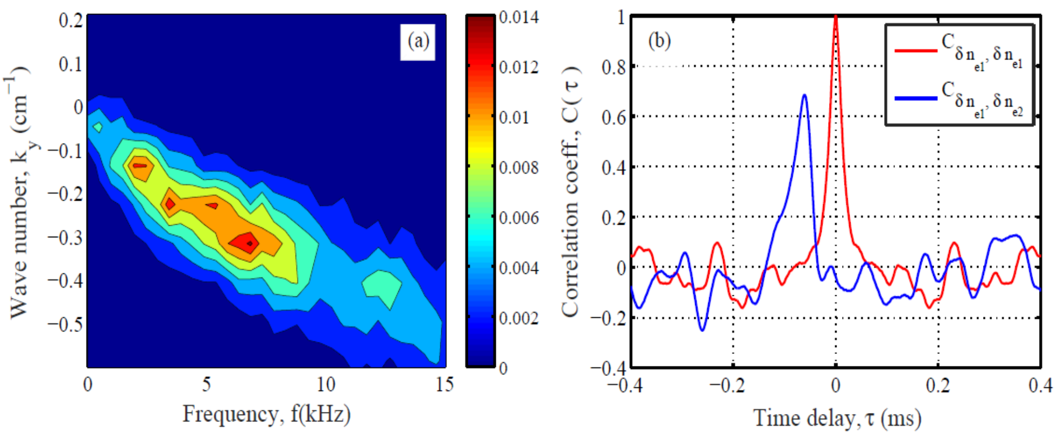

Figure 3.6. (a) The wave number-frequency spectrum S (k_y, ω) The mode exhibits peak power for frequency between, $f \sim$ 1-15 kHz for wave number, $k_\perp \sim$ 0.1-0.4 and (b), the correlation for density fluctuations is shown for radially separated pair of

probes, located at x = 20 cm and x = 30 cm . This gives a measure of radial phase velocity and its direction.

3.4 Theoretical justification for ETG turbulence

The basic characteristics of the mode viz., gradient scale length, real frequency, growth rate and wave-number, are determined from the dispersion relation described by Mattoo et *al*. [24]. The reported experimental wave number $k_y \rho_e \sim 0.2$ exhibits sufficient power but numerical calculation shows maximum growth rate at $k_y \rho_e \sim 0.45$. The theoretically obtained frequency corresponding to the maximum growth rate turns out to be $f \sim 10$ kHz which is approximately close to the experimental observation. We observed for LVPD plasma that $\delta B_z / B_z, \delta n_e / n_e$ and $\delta T_e / T_e$ matches well with the theoretically estimated values from the response functions for ETG mode. For plasma beta $\beta_e = 0.1 - 0.15$, the estimated value of $\delta T_e / T_e \sim 18\%$, turns out to be close to the experimental observation. In summary, our measurements identify ETG driven turbulence in LVPD with no ambiguity.

3.5 Plasma transport

In this section, measurements estimating the particle transport due to the ETG driven fluctuations in the core target plasma of LVPD and subsequently, the net plasma transport will be presented. An estimation of fluctuation induced electrostatic and electromagnetic fluxes will be made in order to estimate the net particle flux. A comparison of the experimentally measured electrostatic particle flux with theoretical estimations will also be presented.

3.5.1 Electrostatic particle flux and PDF analysis of fluctuation induced flux

The electrostatic particle flux (Γ_{es}) is measured from the correlated density (δn_e) and radial velocity (δv_x) fluctuations. The velocity fluctuations are estimated from fluctuating poloidal electric field ($\tilde{E}_\theta$) and by cross product with ambient magnetic field, $\tilde{E}_\theta \times B_z$, where $\tilde{E}_\theta$ is estimated from the floating potential fluctuations measured by a pair of poloidally separated Langmuir probes, $\tilde{E}_\theta = -(\tilde{\phi}_2 - \tilde{\phi}_1)/d$. The electrostatic particle flux is calculated as, $\Gamma_{es} = <\delta n_e.\delta v_x>$ [76–78]. In the presence of temperature fluctuations, electric field fluctuation measurement for estimating the particle flux using floating potential fluctuations may not yield correct result [79]. Therefore, we have compared the electrostatic flux estimated from electric field calculated based on floating as well as plasma potential fluctuation measurement. Figure 3.7(a) and Figure 3.7(b) shows the flux estimated from the floating potential ($<\Gamma_{es}> \approx -1.51\times10^{18} m^{-2}s^{-1}$) and plasma potential ($<\Gamma_{es}> \approx -1.33\times10^{18} m^{-2}s^{-1}$) measurements for the EEF ON plasma. The method of measurement has already been discussed in section II. It has been observed that in spite of morphological deviations observed in temporal profiles of estimated floating and plasma potential fluxes, the magnitude of averaged flux due to them differs only marginally. This can be true for the conditions where there is insignificant phase delay between the plasma potential and floating potential fluctuations when measured simultaneously.

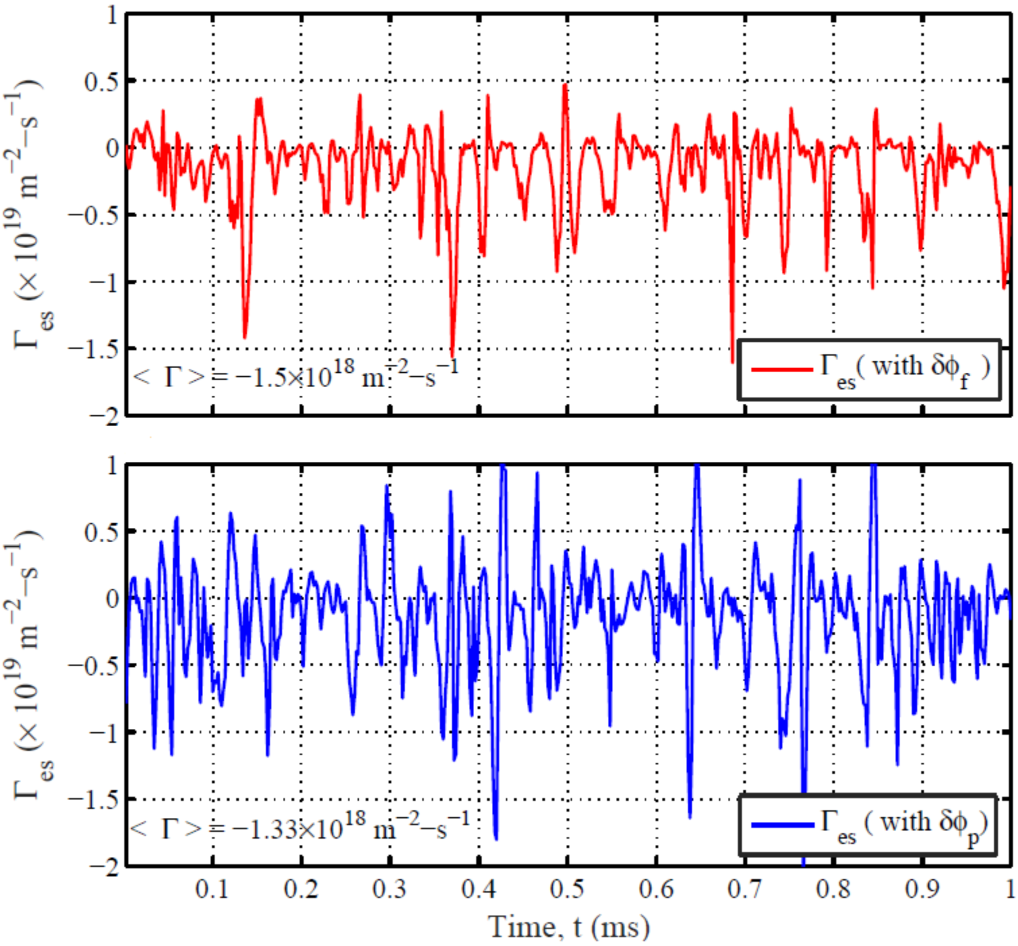

Figure 3.7. The comparison of particle flux at x =30 cm measured with a) floating potential, b) plasma potential fluctuations taken into consideration.

As there is no significant difference observed in the flux estimation, we have therefore carried out further investigations on particle flux by using floating potential fluctuations. The electrostatic flux measured by Langmuir probes for two plasma conditions (EEF ON & OFF) is shown in Figure 3.8. The figure shows that electrostatic flux is significantly higher for EEF ON plasma compared to EEF OFF case.

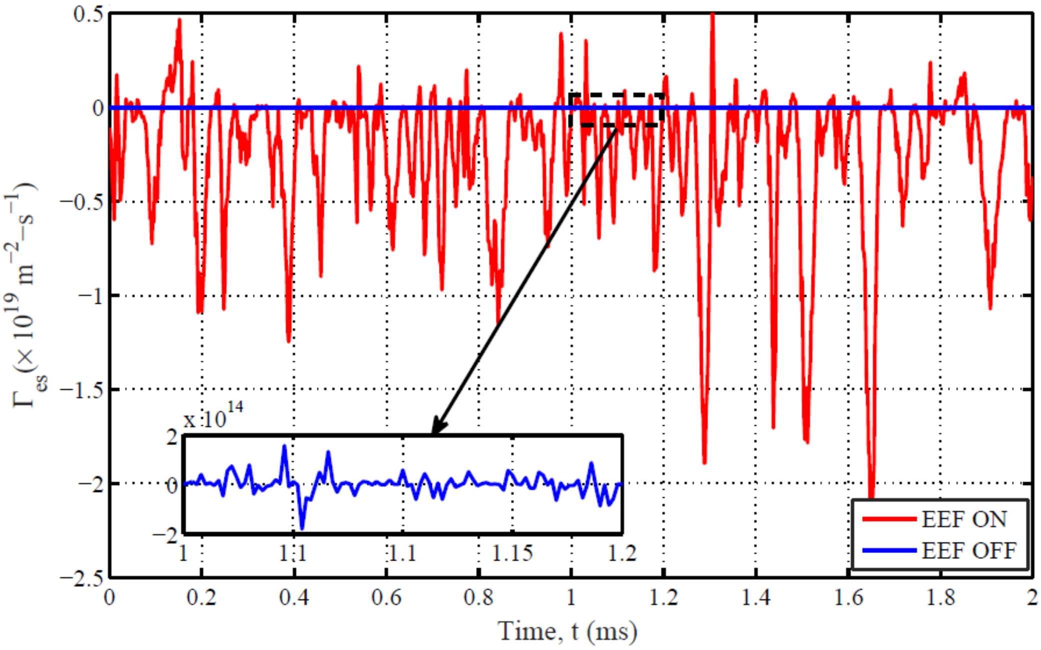

Figure 3.8. Particle flux x = 30 cm for EEF OFF and EEF ON cases are shown. Significantly high level of particle flux is observed for the EEF ON plasma.

The estimated average value for the electrostatic particle flux is $<\Gamma_{es}>\approx -10^{18} m^{-2} s^{-1}$ and the associated negative sign suggests that the observed turbulent particle flux is directed radially inward. In the whole thesis work, only EEF ON plasma will be discussed for particle and heat flux considerations.

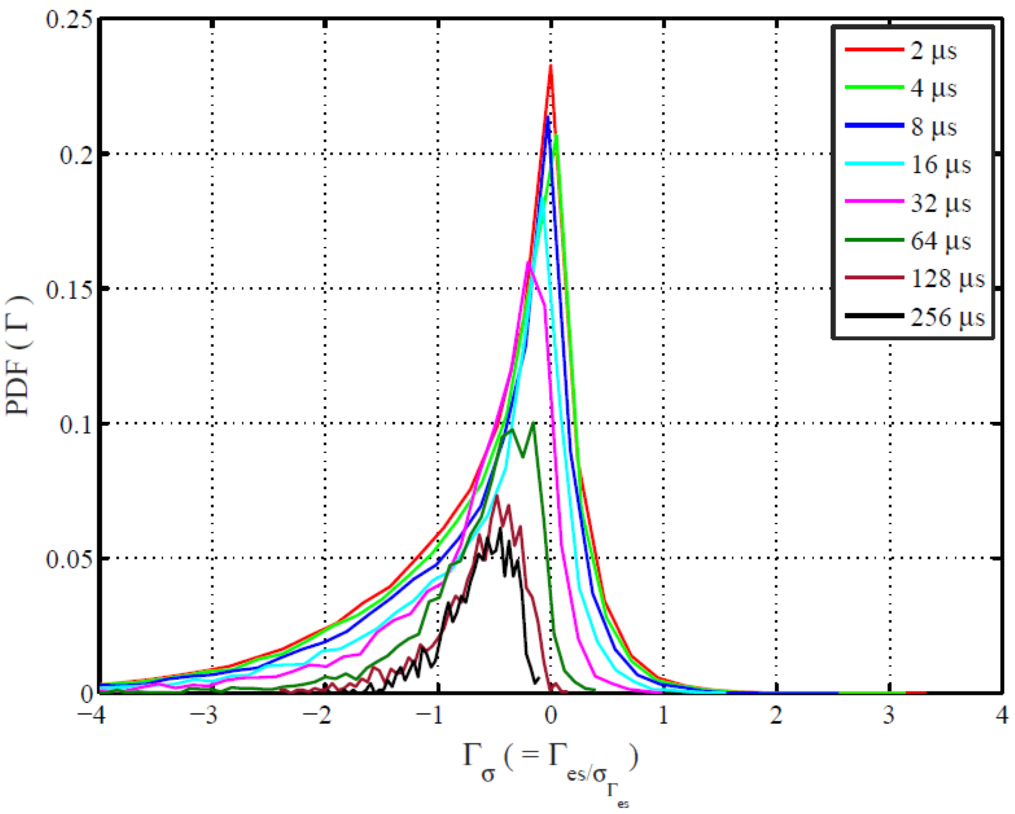

Figure 3.9. Probability distribution function (PDF) for particle flux (Γ_{es}), in the units of standard deviation ($\sigma_{\Gamma es}$ ≈ 4 × 10^{18} $m^{-2}s^{-1}$) for different averaging time. The distribution of particle flux is asymmetric.

To ensure the nature of particle flux in ETG region, the probability distribution function (PDF) analysis is performed using sufficient number of data points, accumulated over 100 plasma discharges [6]. In this process, ensembles of data set with time averaging in steps of 2^n are created. We observed that with increase in time averaging, the peak of the distribution shifts negatively. As shown in Figure 3.9, the PDF is non-Gaussian in nature, it is asymmetric and negatively skewed. The skewness and kurtosis obtained are ~ -1.6 and ~ 6.5 respectively. The negative skewness indicates predominance of large negative flux.

3.5.2 Theoretical explanation for particle flux

The radial profile of time averaged particle flux (Γ) and the phase angle ($\theta_{n,\phi}$) between density and potential fluctuation is shown in Figure 3.10. It is seen that the electrostatic particle flux (Γ_{es}) is radially inward in the core region and is roughly maximizing at radial location $x \le 50cm$. Also, the cross phase angle is deviated from 180^0 where $\eta_e (= L_n / L_{T_e})$ has dominance. The profile of particle flux is determined by the product of density and potential fluctuation amplitudes with sinus (Sine) of the cross phase angle.

Experimental results are compared with the theoretical model proposed by R. Singh et al. [80], for turbulent flux in the electrostatic ETG turbulence. The present observation is based on a model where ions are un-magnetized and collision less. In the limit $k_\perp V_{thi} \sim \omega$, ETG mode resonates with background ions, which deviates from Boltzmann relation known as ion non-adiabatic response.

$$\tilde{n} = -\tau_e \tilde{\phi}\left[1 + i\pi^{\frac{1}{2}}\frac{\omega}{k_\perp V_{thi}}\exp\left(-\frac{\omega^2}{k_\perp^2 V_{thi}^2}\right)\right] \tag{5}$$

This non-adiabatic ion-response induces a net particle flux due to phase lag between density and potential fluctuation. Phase lag between density and potential also agrees with experimental observation made in core plasma of LVPD [Figure 3.5]. The particle flux is given by

$$\Gamma_n = < \tilde{V_x}\tilde{n} > = \Sigma_k \tilde{V}_{xv}\, \tilde{n}_k^* = \ -\Sigma_\mathrm{k}\frac{k_y}{B}|\tilde{\phi}_k||\widetilde{n_k}|\sin\theta_{n\phi} \tag{6}$$

Where $\theta_{n\phi} = \theta_n - \theta_\phi$ is the cross angle between density and potential fluctuation. The particle flux expression for ion response is given by eqn. (3) becomes

$$\Gamma_n = \sum_k \pi^{\frac{1}{2}} \tau_e n c_e k_y \rho_e \frac{\omega_r}{k_\perp V_{thi}} \exp - \frac{\omega_r^2}{k_\perp^2 V_{thi}^2} |\widetilde{\phi_k}|^2 \quad (7)$$

Where, $c_e = \sqrt{T_e / m_e}$, ρ_e is the electron Larmor radius and ω_r is the real frequency. This shows that the particle flux can become negative when $\omega / k_y < 0$ that is when the mode is propagating in ion diamagnetic drift direction. The S (k, ω) and four probe assembly measurement shows that the mode is propagating in ion diamagnetic drift direction and hence observed particle flux is radially inward.

The experimental results are compared with theoretical values for cross angle $\theta_{n\phi}$ obtained from Eqn. (5) and flux (Γ) from Eqn. (7). For each comparison, the values for ω and k_y are chosen, corresponding to peak power of density perturbation in $\omega - k_y$ space from Figure 3.6(a).

As shown in Figure 3.10, the radial profiles of cross phase and flux thus calculated follows similar trend as the experimentally observed profiles and has good agreement with each other. The small quantitative difference between theory and experiment could be due to the fact that for theoretical estimate, we only considered the mode with maximum power while in experimental observations, all the modes are contributing to produce the net particle flux larger than the theoretical estimates. Consideration of floating potential fluctuations in place of plasma potential fluctuations for particle flux measurements in the presence of temperature fluctuations may have also contributed in observed deviation. However, the same argument does not seem to hold around the maximum flux region where the theoretical estimates corresponding to maximum power mode is larger than experimental observations.

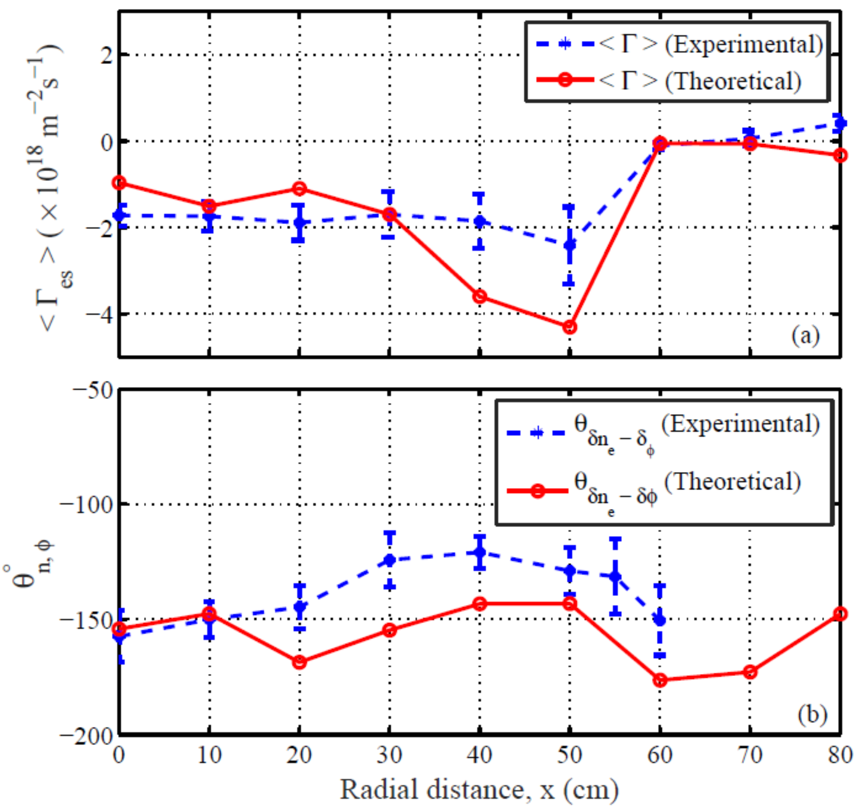

Figure 3.10: Radial profile of (a) mean particle flux, $<\Gamma_{es}>$ and (b) phase angle, ($\theta_{n\phi}$) compared with theoretical estimates for ETG mode with experimental S (k_y, ω).

The inward particle flux is not inconsistent with thermodynamics. Following the work of Horton et al., [81] , it can be seen that the inward anomalous particle flux Γ_{es} leads to the reduction in entropy of the system which should be compensated by the radial thermal flux q_e in such a way that the net entropy production from all anomalous transport processes should become positive definite.

3.6 Summary and conclusion

We studied fluctuation induced particle transport in LVPD. The source of the underlying turbulence has been established to be due to electron temperature gradient driven modes in the core of the target region of the device. This is ensured by making the target region free of energetic electrons by using a transverse magnetic field with the help of an EEF. Experimentally observed density-potential cross-correlations and turbulence power spectra along with their frequency and wave number ordering confirm that the observed turbulence is driven by ETG.

The particle flux maximizes in the core region when EEF is ON clearly indicates that the flux is due to the fluctuations resulting from ETG. Net particle flux results from the phase difference between the density and potential fluctuations, other than 180^0 for ETG driven modes. Turbulence intensity maximizes roughly at the location where particle flux maximizes. The experimental cross phase angle and flux has been compared with the cross phase and flux resulting due to the non-adiabatic ion response due to the resonant interaction of the ions with the ETG mode $k_\perp V_{thi} \sim \omega$. The experiment and theoretical results quantitatively follows the same trend across the radius and agrees well within 20% with each other.

Chapter 4
Experimental study of particle transport due to electromagnetic fluctuations

4.1 Introduction

In this chapter, we have investigated electromagnetic (EM) fluctuations induced plasma transport in finite beta ($\beta = 2\mu_o n T_e / B^2 \sim 0.01 - 0.4$) of Large Volume Plasma device (LVPD) where magnetic fluctuations are present [82]. This types of transport is arises due to correlated fluctuations of parallel current and radial magnetic field fluctuations present in the system defined by

$$\Gamma_{em}^{q} = \frac{1}{qB} < \delta J_{\parallel,q} \delta B_r > \quad (8)$$

where $\delta J_{\parallel q}$ is parallel current fluctuations for charge species q (= e, i for electron and ion, respectively), δB_r radial magnetic field fluctuations and B is plasma confining magnetic field.

The significance of magnetic fluctuations in the edge of various toroidal devices suggests that they are very significant in contributing to transport in different device configuration regimes like reversed field pinches [38] , high beta tokamaks [39], and tokamaks in L-H transition [40] .

The magnetic fluctuations can be driven by different instabilities present in plasma due to inhomogeneity in plasma parameters. The basic understanding of magnetic fluctuation induced particle transport processes is thus of great interest and potentially critical to plasma density control and understanding fast particle losses in future plasmas like ITER. As reported, magnetic fluctuations induced plasma transport can be large even if the fluctuation amplitude is extremely small [35] . The stochastic magnetic field is deliberately imposed in tokamak plasmas by using external coils to mitigate the edge-localized modes excited electromagnetic particle flux [42]. However, transport due to magnetic fluctuations has been mainly studied indirectly by measuring runaway electron flux to a limiter. Such experiments are useful for probing the magnetic fluctuations but do not provide a local measurement of particle transport resulting from the magnetic field.

In high beta ($\beta \sim 0.01 - 0.4$) plasma of LVPD, the coupling of Whistler and ETG mode becomes important where W-ETG mode becomes unstable like ETG only when the electron temperature gradient crosses a threshold value, $\eta_e > 2/3$. In magnetized plasma, the electromagnetic flux in ETG background is expected to be zero as per the conventional ETG mode theory, where it is assumed that the electron current, $J_{\parallel,e}$ is the total current, $J_{\parallel}$. Noticeably, we do observe a small ($\Gamma_{em} \approx 10^{-5}\Gamma_{es}$) but finite electromagnetic flux in the LVPD. Obviously this means that the assumption $J_{\parallel e} = J_{\parallel}$ is broken in reality and consequently leads to a finite flux. This chapter provides a detailed measurement of radial electromagnetic particle flux, $\Gamma^{e,i}_{em}$ for both charge species, electron and ions, which results primarily from the correlation between fluctuations of parallel electron current ($\delta J_{\parallel,e,i}$) and radial magnetic field (δB_r) across the radius of the LVPD. We provide a general theory of the electromagnetic particle flux in ETG turbulence in a straight homogeneous magnetic field geometry which explains well the experimental observations. A finite electromagnetic radial flux is shown to result from the sluggish and passive parallel ion velocity fluctuations resulting from the parallel force experienced by ions due to ETG fluctuations although ions are un-magnetized. The motion is sluggish because the ion velocity scales as $\frac{m_e}{m_i} v_{\|e}$ and passive because this small mass ratio for Argon plasma barely effect the linear features of the ETG mode. Lack of magnetization of ions fails to produce a fluctuating radial drift of ions, which leads to no turbulent ion flux making the flux non-ambipolar. The electron flux is made up of pieces resulting from parallel ion current fluctuations and resulting from magnetic stresses. The piece of flux resulting from ion current fluctuations is exactly similar to electromagnetic ion flux, had the ions been magnetized like the ITG turbulence. Due to this morphological similarity it is dubbed here as pseudo ion flux. Quasilinear estimate is obtained for the pseudo ion flux which agrees well with the experimental measurement. Sluggish parallel ion response is identified as the key mechanism for generation of small but finite electromagnetic flux for ETG turbulence of LVPD.

The rest of the chapter is organized as follows; the experimental setup and diagnostics are described in section 4.2. The experimental observations are discussed in section 4.3. In section 4.4, we discuss the theoretical model and its comparison with experimental results. Finally, the summary and conclusion of this chapter is provided in section 4.5.

4.2 Experimental setup

The experimental setup primarily consists of Large Volume Plasma Device (LVPD) [26], the cathode, large electron energy filter(EEF) and diagnostics. The directional probes are used for the measurement of parallel current density due to electrons, $J_{\|,e}$ and ions, $J_{\|,i}$ motion [66,83]. Miniature bi-filer B-dot probes are used for measuring the three components of magnetic field (B_x, B_y, B_z) fluctuations. Basic plasma parameters are acquired by conventional diagnostics as discussed in Chapter 2.

The large volume plasma device is a cylindrical, double walled, water cooled, vacuum chamber of dimension ($\phi = 2m, L = 3m$) [26]. The source of primary ionizing electrons is a set of 36 filaments of dimension ($W, \phi = 0.5mm, L = 16cm, A_{emission} \sim 75cm^2$), which are deployed on the periphery ($90\ cm \times 130\ cm$) of a rectangular, water-cooled cusped plate. The $4kG$ Samarium Cobalt magnets are used to produce the cusp magnetic field. Axial confinement of plasma particles is provided by similar cusped end plates, placed axially opposite to the cathode plate [84]. The radial confinement is provided by a uniform 6.2 G axial magnetic field, produced by a set of 10 coils, garlanded over the surface of the vacuum chamber. The pulsed Argon plasma is produced of discharge duration ($\Delta t_{discharge} = 9.2ms$) by applying a discharge voltage of $70V$ between the cathode and the vacuum chamber at a filling pressure of $P_{Ar} \sim 4 \times 10^{-4} mbar$. The device has a base pressure of $1.5 \times 10^{-6} mbar$.

In LVPD, we have produced plasma conditions suitable for carrying out an unambiguous investigation on ETG turbulence. The recipe for such plasma is characterized by uniform plasma density, sharp electron temperature gradient, and plasma devoid of non-thermal electrons. This ensures that excited plasma instabilities have origin only in electron temperature gradient. Usually, filamentary discharges contain a large population of non-thermal electrons and hence producing ETG suitable conditions is a tedious assignment. Also, establishing an independent control over density and temperature profiles is proved to be a difficult task. We dressed LVPD plasma to meet these requirements by inventing a large-sized electron energy filter [24,27]. The filter is a solenoid having rectangular cross section with 82% transparency and is placed across the diameter of the LVPD. It is of the variable cross-section with a maximum at its axis ($190\,cm \times 4\,cm$) and minimum near the walls (4 cm × 4 cm). It divides LVPD plasma into three regions of Source, EEF and target plasmas.

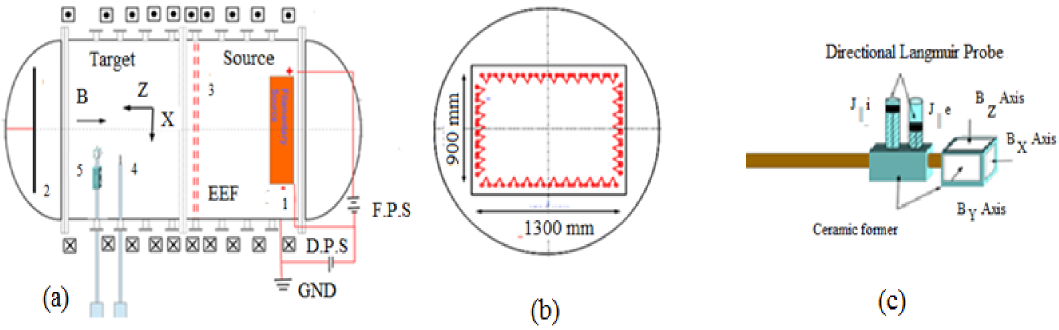

Figure 4.1. Schematic diagram of experimental setup is shown in (a), the layout shows internal components marked as (1) back plate, (2) end plate, (3) Electron Energy Filter(EEF), (4) Langmuir Probe, (5) a pair of B-dot and directional Langmuir probes for $J_{//}$ measurements, (b) cross-section view of LVPD showing the filament assembly arranged in a rectangular geometry (1300 mm × 900 mm) in the source region, and (c) probe assembly for EM flux measurement is marked as (5) in figure (a). This assembly contains a pair of directional Langmuir disc probes for parallel electron and ion current measurements and a 3-axis B-dot probe.

A detailed description of LVPD, EEF, information about characteristic features of different plasma regions and details of conventional diagnostics is already described in the referred work [26,27,75] and in essential details of Chapter 2. The present study focuses on the target region, where scale length of the gradient in density and electron temperature satisfies the ETG threshold conditions [Figure 4.1].

The investigations on EM particle flux, we do the measurement of parallel electron and ion currents along with magnetic field fluctuations in target plasma. For this purpose, we installed a specially designed probe array, accommodating a pair of directional probes (DP) for the measurement of fluctuations in parallel currents and a 3-axis B-dot probe for magnetic field fluctuation measurement [66,85]. The directional probe assembly contains a disc probe of diameter, ϕ =5 mm and is encapsulated in a ceramic tube so that shielding restricts the solid angle through which probe collects particle and thus allows only the directed charge species see Figure 4.1 (c). The pair of directional probe assembly is radially separated by Δ x = 8 mm. Out of these two probes, the one probe which is used for collecting parallel electron current is accommodated within the ceramic tube at a distance of 5mm [$\sim \rho_e$ (maximum at $x = 0$)] thus allowing primarily collection of parallel electron current at all radial locations. The parallel electron current density $J_{\|e}$ is measured by keeping probe biased at plasma potential. Near plasma potential, probe collects electrons moving with electron thermal velocity, $V_{the} = \left(\frac{T_e}{m_e}\right)^{0.5}$. In the collision less scenario of LVPD, where electrons are magnetized, the parallel electron flux can be approximated as electron thermal flux, i.e. $J_{\|e} \approx J_{e,sat}$. Due to shielding of directional probe, only those electrons with Larmor radius, $\rho_e < \phi_{disc}$ and which are tied to magnetic field lines will contribute for parallel electron current density fluctuations. The electrons coming from random directions will be screened out. In the order to measure parallel electron current, we first established plasma potential measurement by making use of a center tapped emissive probe (CTEP) [74].

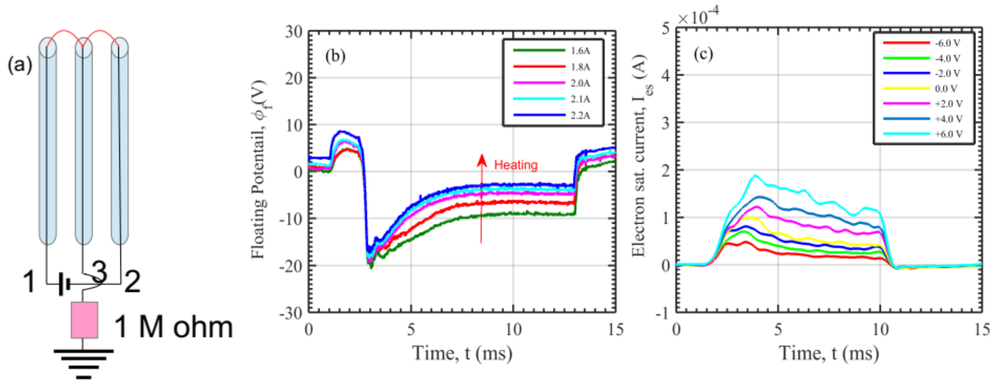

Figure 4.2. The schematic of the CTEP is shown in (a). In CTEP, floating potential is measured at nodal point 3, by heating it to different temperatures, operating CTEP in floating point technique. The floating potential is measured at the center of the device. The saturated CTEP potential at I_{CTEP} ~2.1 give the measure of plasma potential, ϕ_P in (b). The parallel electron current measurements in (c) are made by keeping the directional disc probe at potential $\geq \phi_P$.

The center-tapped emissive probe consists of a pair of emissive probes of equal electrical length and center of total electrical length serves as a center tap point. The three nodes of the probe are crimped to the gold plated beryllium copper pins. These pins are accommodated in a 3 bore ceramic tube and are isolated from plasma by the filled ceramic paste. The three bores of the ceramic tube hold all three nodes of the emissive probe. The two nodes 1 & 2 are elevated to potential –V and +V with respect to the common of DC power supply whereas the center tap point remain tied at zero potential (-V+V)/2=0). Measurements made at the junction remains unaffected due to the lifting of potential at two ends. A schematic diagram of CTEP is shown in Figure 4.2(a).

The plasma potential is measured using CTEP by operating it using floating point technique. The CTEP heating current is varied till floating potential saturates.

Figure 2(b) shows the saturation of floating potential at -4V for a heating current of ~ 2.1 A. This voltage is taken as bias potential for the measurement of parallel electron current. The bias potential to the disc probe, in the vicinity of plasma potential is varied till electron current approaches saturation. The typical variation of $I_{||e}$ near to plasma potential is shown in Figure 4.2(c). The estimation of parallel electron current is made at all radial locations by keeping the probe bias fixed at this voltage.

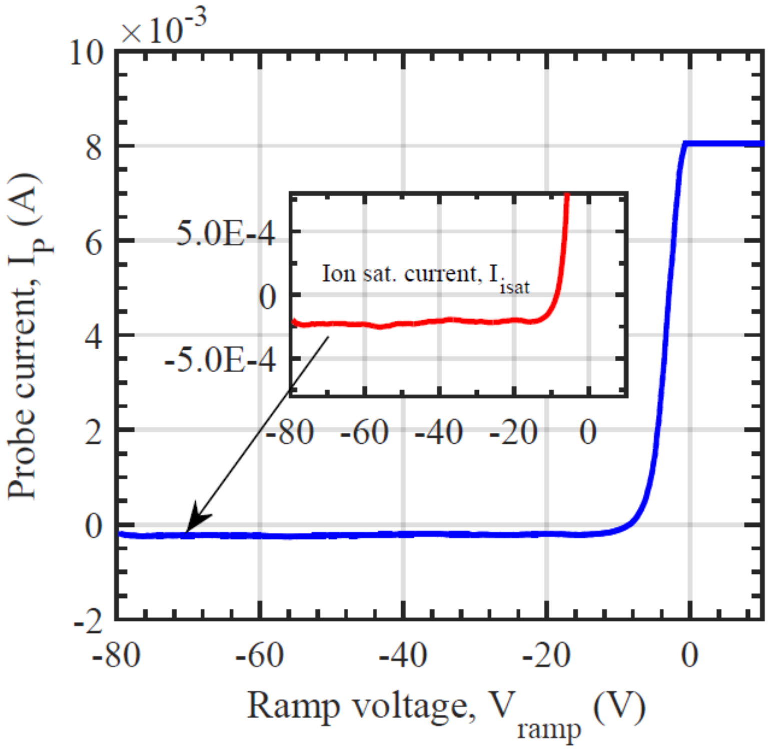

Figure 4.3. I/V curve obtained at x = 0 for the directional disc probe used for measuring parallel ion current is shown. The almost saturated value of ion current indicates the negligible effect of sheath expansion in ion current measurements. The probe is biased at -80 V to ensure contribution primarily for parallel ion current.

The second disc probe ($\phi_{disc} =$ 5 mm) of the array is used for measuring parallel ion current. This probe is kept at 2 mm ($\gg 10\,\lambda_d$) inside the ceramic tube to cater the effect of ion sheath expansion.). The I/V curve obtained for this is shown in Figure

4.3, suggesting that at high negative bias potential, the probe collects only ion current and its saturation indicates negligible effect of sheath expansion in ion current measurements. The current density is given as, $J_{i,sat} \approx 0.6\, n_i e c_s$, where n_i is ion density, $c_s = \sqrt{\frac{T_e}{M_i}}$; Bohm velocity, and e the electronic charge. The parallel ion current density is estimated following $J_{\|i} = e n_i V_{\|} = (\frac{M}{0.6}) * J_{i,sat}$, where $\frac{V_{\|}}{c_s} \approx M$ [66,86,87].

The magnetic field fluctuations are measured using a 3 axis B-dot probe. This probe is configured in bi-filer geometry and is capable of measuring all three components of the magnetic field over the frequency band of (1-100) kHz. Details on this are described in diagnostics section of Chapter 2.

4.3 Experimental observations

4.3.1 ETG turbulence characterization

The plasma of the far target region from EEF is characterized for ETG threshold conditions [24]. We have divided the target plasma of LVPD in two regions namely, core (x ≤ 50 cm) and edge (x > 50 cm) plasmas. The core plasma exhibits uniform plasma density profile but offers a finite gradient in electron temperature. It is important to mention here that EEF produces a transverse magnetic field of B_x ~160 G over its axial width of 4 cm. The EEF magnetic field falls rapidly beyond its boundaries and attains a magnitude, equal to the ambient axial magnetic field of $B_z = 6.2$ G produced by a set of 10 garlanded coils.

The mean plasma parameters namely, plasma density, n_e, electron temperature, T_e, and floating potential, V_f, are measured using compensated cold Langmuir probes [88,89]. The electron temperature is estimated from the I_e versus V_B characteristic of the probe by using the expression, $T_e = [d\ln(I_e)/dV_B]^{-1}$ and $I_e (= I_p - I_s)$, here I_e and V_B are the electron current and probe bias voltage respectively. The characteristic exhibits no signature of the presence of tail electrons in the region. However, temperature fluctuations are estimated by using a pair of closely separated Langmuir probes ($\phi_{P_{1,2}} \approx 1mm, L_{P_{1,2}} = 5mm$ and $\Delta x_{P_{1,2}} = 5mm$) from $\delta T_e = e(\phi_2 - \phi_1)/\ln(I_{e1}/I_{e2})$ where ϕ_1, ϕ_2 and I_{e1}, I_{e2} are the bias voltages and electron currents of the respective probes [24]. The probe orientation for all these measurements is always maintained perpendicular to the axial magnetic field.

The radial profiles are generated in the far target region of LVPD and are shown in Figure 4.4. The plasma density and electron temperature gradient scale lengths are $L_n = [\frac{1}{n_e}\left(\frac{dn_e}{dx}\right)]^{-1} \sim 300$ cm and $L_T = [\frac{1}{T_e}\left(\frac{dT_e}{dx}\right)]^{-1} \sim 50$ cm in the core region. In the outer region, the density fall becomes sharper while the electron temperature flattened out. Plasma potential does not show much variation in its value beyond an extent of $40cm$. The threshold condition for ETG turbulence $\eta = L_n / L_T > 2/3$ is satisfied in the core region $x \le 45cm$ and an axial distance of $z \ge 70cm$ away from the EEF. The maximum level of fluctuations reported for density, temperature and potential from the core region are 10 %, 30 % , and 1 % , respectively [30].

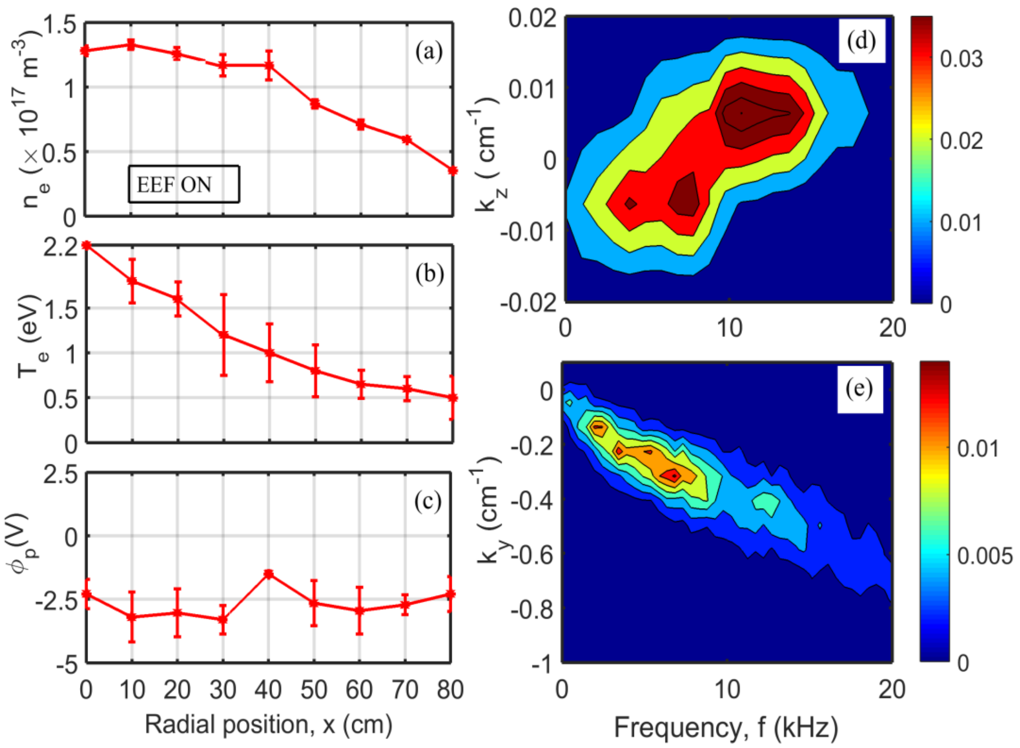

Figure 4.4. Radial equilibrium profiles for plasma parameters viz., (a) density, $n_e(m^{-3})$, (b) electron temperature, $T_e(eV)$, (c) plasma potential, ϕ_p , are shown. The wave number ffrequency spectra, S(k, ω) for parallel and perpendicular propagation are shown in (d) and (e), respectively.

The wave number- frequency spectra for parallel, $S(k_z,\omega)$ and poloidal, S(k_y, ω) propagation are measured to define characteristic features of the observed fluctuations in Figure 4.4(d, e). The S(k , ω) is obtained by simultaneous measurement of ion saturation current fluctuations with the pair of axially separated ($\Delta z \approx 30cm$) and poloidally separated probes ($\Delta y = 1.5\ cm$). The large data length of 2×10^5 points is used for the power spectral analysis. This is obtained from an ensemble of ~ 100 identical plasma discharges with sampling rate of 1 MS/s. The data series is constructed by extracting 2048 data points from the steady state period of $6ms-8ms$ from each plasma discharge. These data are segmented into 200 bins of 1024 data points each for obtaining a higher frequency resolution in the spectral analysis. The analysis exhibits confidence measure, $(1 - \frac{1}{\sqrt{N}}) * 100 = 93\ \%$, where N is number of ensembles and variance, $\sigma^2 \sim \pm 0.01$ respectively. The measured maximum power from $S(k_z, \omega)$ for axial measurements correspond to frequency, $f \approx 7kHz$ and wavelength, $|k_z| \approx 0.006cm^{-1}$ respectively. Significant power for poloidal $S(k_y, \omega)$ resides in frequency band of $(25 - 90)\ krad/s$ in correspondence to wavenumber, $k_y\rho_e \sim 0.1 - 0.2$. These observations satisfy the frequency and wavelength ordering of ETG mode turbulence, $\Omega_{ci} < \omega(25 - 90)\ krad/s \ll \Omega_{ce}$, $k_\perp\rho_e \leq 1$ and $k_\perp\rho_i > 1$, where ($\Omega_{ci} \sim 2\ krad/s$) and $\Omega_{ce} \sim 94 \times 10^3 krad/s$) are ion and electron cyclotron frequency and $\rho_e(\sim 5mm)$ and $\rho_i(\sim 40cm)$ are larmor radii of electron and ions respectively. The axial phase velocity $v_z \approx 7 \times 10^6 cm/s$ of the mode is two orders higher than the perpendicular velocity, $v_\perp \approx 2\times 10^4$ cm/s [28].

A comparison of experimental observations is made with the estimates obtained from the generalized dispersion relation of ETG as suggested by Singh et *al.* [21, 26]. They have shown that in the absence of magnetic gradient and curvature effects, similar to situations prevailing in linear devices, the long wave length "toroidal" ETG-like mode can be excited, because coupling of the slab ETG mode with the whistler mode at high β leads to the similar compression physics that is valid for toroidal mode. They have shown similarity in temperature perturbations produced in continuity equation by finite diamagnetic compressibility due to non-zero $\nabla_x B$ effect and finite diamagnetic compressibility due to δB_z perturbation effect and for both cases, their responses to temperature perturbations, which are responsible for temperature gradient driven mode, emerge in same phase. Moreover, they have shown that W-ETG mode gets destabilized only when the electron temperature gradient crosses a threshold, $\eta_e > 2/3$.

The generalized dispersion relation for the ETG mode is expressed as

$$\hat{\omega}\left[\hat{\omega}\,\tau_e^* + \epsilon_n \hat{k}_y + \hat{k}_\perp^2\left(\hat{\omega} - (\epsilon_n + \epsilon_T)\hat{k}_y\right) + \hat{\beta}(1+\tau_e^*)\{\hat{\omega} - (\epsilon_n + \epsilon_T)\hat{k}_y\}\right]$$
$$- \hat{\beta}\left[\hat{\omega} - (\epsilon_n + \epsilon_T)\hat{k}_y\right]\left[\left(\epsilon_T - \frac{2}{3}\epsilon_n\right)\hat{k}_y - \frac{2}{3}\tau_e^*\hat{\omega}\right] \quad (9)$$
$$= \hat{k}_\parallel^2 \hat{k}_\perp^2 \left[\left(1 + \frac{5}{3}\tau_e^*\right)\hat{\omega} - \left(\epsilon_T - \frac{2}{3}\epsilon_n\right)\hat{k}_y\right] / \left[\hat{\omega}\left(\hat{\beta} + k_\perp^2\right) - \hat{\beta}(\epsilon_n + \epsilon_T)\hat{k}_y\right]$$

Here we have introduced normalized parameters: $\hat{\beta} = \beta_e/2$ $\hat{\beta} = \beta_e / 2$, $\varepsilon_T = R/L_T$, $\varepsilon_n = R/L_n$, $\hat{\omega} = R\omega / c_e$, $\hat{k}_\perp = \hat{k}_y \sim \hat{k}_x = k_\perp \rho_e$, $\hat{k}_z = k_z R = k_\parallel R$, $\hat{\rho}_e = \rho_{e/R}$, $\tau_e = T_e / T_i$, and $\tau_e^* = \tau_e[1 - \tau_e \hat{\omega}^2 \hat{\rho}_e^2 m_i / \hat{k}_\perp^2 m_e]^{-1}$, where R is an arbitrary normalization length.

Figure 4.5 shows the growth rate, real frequency, and variation of normalized fluctuations in a magnetic field and electron temperature with plasma density for different plasma beta values. The Figure 4.5(a, b) shows that a variation of linear growth rate ($\hat{\gamma}$) and real frequency ($\hat{\omega}$) with increasing values of beta, all other parameters used are shown in the figure itself.

Numerical predictions suggests that the growth rate for the observed mode peaks at $\hat{k}_y \sim 0.45$ in comparison to the work of Mattoo et *al.*, [24] where they have shown that it observed turbulence peaks at $\hat{k}_y \sim 0.2$.

Following model equations, Mattoo et al., [24] have estimated non linearly saturated fluctuation levels with numerical values. The amplitudes of density fluctuation $\tilde{n}$, parallel magnetic field fluctuation $\tilde{B}_z$ and electron temperature fluctuation $\tilde{T}$ are expressed in term of potential fluctuation $\tilde{\phi}$,

$$\left|\frac{\delta n_e}{n_e}\right| = |\tau_e^*| \left|\frac{e\delta\phi}{T_e}\right| \tag{10}$$

$$\left|\frac{\delta B_z}{B_z}\right| = \frac{\beta_e}{2}\left|\left[1 + \frac{5}{3}\tau_e^* - \left(\epsilon_T - \frac{2}{3}\epsilon_n\right)\frac{k_y\rho_e}{R\omega c_e}\right]\right| \left|\frac{e\delta\phi}{T_e}\right| \tag{11}$$

and

$$\left|\frac{\delta T_e}{T_e}\right| = \left|\left[\left(\epsilon_T - \frac{2}{3}\epsilon_n\right)\frac{k_y\rho_e}{R\omega c_e} - \frac{2}{3}\tau_e^*\right]\right| \left|\frac{e\delta\phi}{T_e}\right| \tag{12}$$

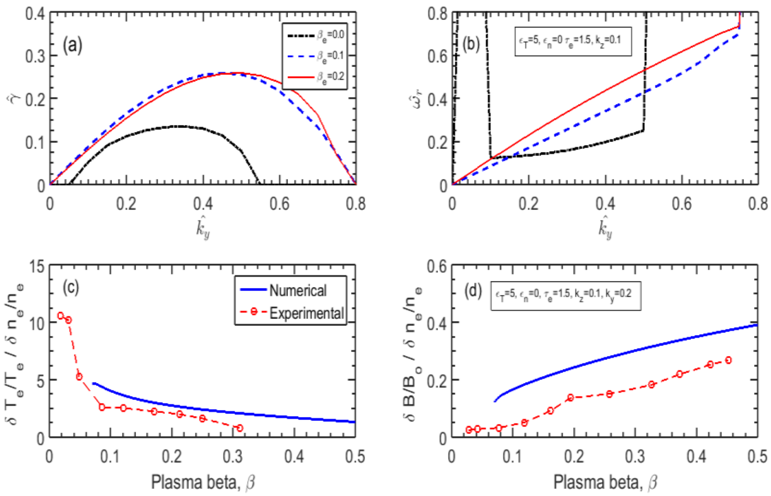

Figure 4.5: Normalized (a) growth rate $\hat{\gamma}$ and (b) real frequency, $\hat{\omega}$ verses $\hat{k}_y$ are shown for the ETG mode. A comparison of the ratio of numerically obtained normalised fluctuations of temperature and magnetic field with the normalised density fluctuations are shown in (c) and (d), with plasma beta variation in comparison to experimental measurement.

We have obtained growth rate and real frequency for the observed turbulence from the dispersion relation [Eqn. 9]. Figure 4.5(a, b) shows that a variation of linear growth rate ($\hat{\gamma}$) and real frequency ($\hat{\omega}$) with increasing beta values. In Figure 4.5(c, d), numerically obtained normalized value of fluctuations in temperature and magnetic field with density are compared with the experimentally obtained values. We examined the ratios of fluctuation amplitudes, as it eliminates the need for the absolute fluctuation amplitude of potential. We have obtained the ratios of fluctuations by using equations (10-12) for different plasma beta conditions imposed. For experimentally obtained $\hat{k}_y \sim 0.2$, the theoretically estimated values of, $(\delta T_e/T_e)$ / $(\delta n_e/n_e)$ and $(\delta B_z/B)$ / $(\delta n_e/n_e)$ agrees well with experimental observations.

4.3.2 Characterization of $J_{||e}$, $J_{||i}$ and B_z fluctuations

In finite beta plasma of LVPD, the observed ETG turbulence may exhibit characteristics of W-ETG turbulence, where parallel compression excited by the long wavelength of whistler wave gives additional perturbation in confining axial magnetic field [22]. The W-ETG turbulence due to finite β effect causes magnetic fluctuations. By the use of bifilar B-dot probe, fluctuations in all the three components (δB_x, δB_y and δB_z) of the magnetic field are measured.

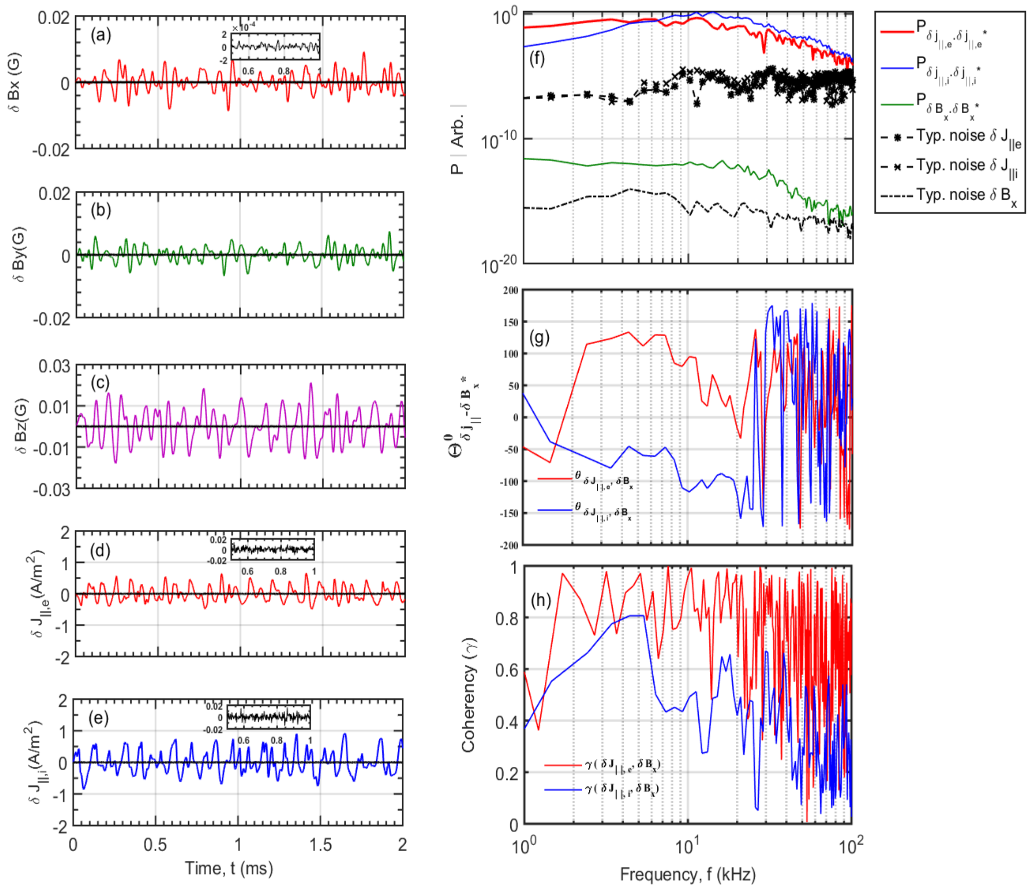

Figure 4.6. Time profile of magnetic field fluctuations in (a) x-component, δB_x and the noise (b) y-component, δB_y and (c) z-component, δB_z , and parallel current density fluctuations due to d) electrons, $J_{\parallel e}$ and e) ions, $\delta J_{\parallel i}$ and respective noise of the probe are shown. In (f- h), the auto power spectra of all signals and noise, phase angle and coherency between $J_{\parallel e}$, $\delta J_{\parallel i}$ with δB_x are shown.

Using specially designed directional probe arrangement, the parallel electron and ion current fluctuations are measured. Figure 4.6(a- e) shows a typical time series snap shot of fluctuations for all the three components of magnetic field and parallel electron and ion current respectively. The spectral characteristics are shown in Figure 4.6 (f- h). The power spectrum shows the spread of fluctuations over the frequency band of $1 - 10\ kHz$, in line with the $S(k_y, \omega)$ for W- ETG turbulence [Figure 4.6 (f)]. The phase angle of the fluctuations in radial magnetic field with electron(red) and ion(blue) currents, $\Theta_{\delta J_{\|e,i},\delta B_x}$ remains uniform over the wide band of frequency [Figure 4.6 (g)]. The coherency, $\gamma(f)$ between the respective signals is high ≥ 0.6 in comparison to the calculated minimum significance level of coherency which is typically ≈ 0.1 for the frequency band of $1 - 10\ kHz$ [90]. A comparison of the measured signal for both directional and B-dot probes with noise shows significant S/N ratio in measurements. The data acquisition system (PXI -NI5105, 12 bit digitization), resolves voltage signals $\sim 0.25\mu V$ which is well below the noise level ($\sim 1\ \mu V$).

4.3.3 Radial profiles of normalized fluctuations

The radial profiles of normalized fluctuation in B_x, B_y ,B_z, $J_{\|e}$ and $J_{\|i}$ are measured and shown in Figure 4.7. We observed that normalized fluctuation amplitudes are higher in the core region and the typical levels of δB_x, δB_y and δB_z lies between $0.05\,\%-0.2\,\%$ whereas, the normalized parallel current fluctuations because of electron and ions are 10 % to 20 %.

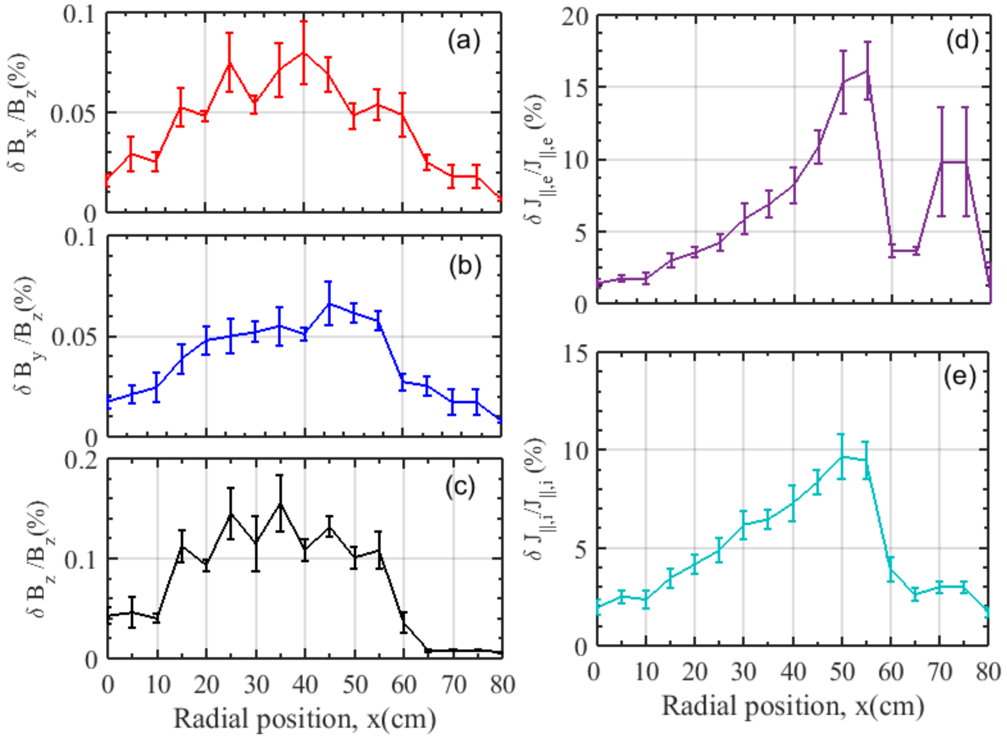

Figure 4.7. Typical radial profiles of normalized fluctuations in three components of the magnetic field and parallel electron and ion current are shown in (a-c) and (d-e) respectively.

4.3.4 EM flux measurement and comparison with electrostatic particle flux

Both electrostatic and electromagnetic particle fluxes due to fluctuations are measured along the radius of the target chamber. The electrostatic particle flux ($\Gamma_{es} = \delta n_e \delta v_r$) is measured from the density (δn_e) and radial velocity (δv_x) fluctuations. The velocity fluctuations are estimated from the cross product of fluctuating poloidal electric field (δE_y) and ambient magnetic field, i.e. $\delta E \times B$, where δE is estimated from the floating potential fluctuations measured by a pair of poloidally separated Langmuir probes [30]. The electromagnetic flux derived from

$\Gamma_{em} = \frac{1}{qB} < \delta J_{\|q} \delta B_x >$, where 'q' is the charge, is observed to be $\sim 10^{-5} \times < \Gamma_{es} >$.

Figure 4.8 shows a comparison of the estimated electromagnetic particle flux due to electron current with electrostatic flux at x=30 cm in the target chamber.

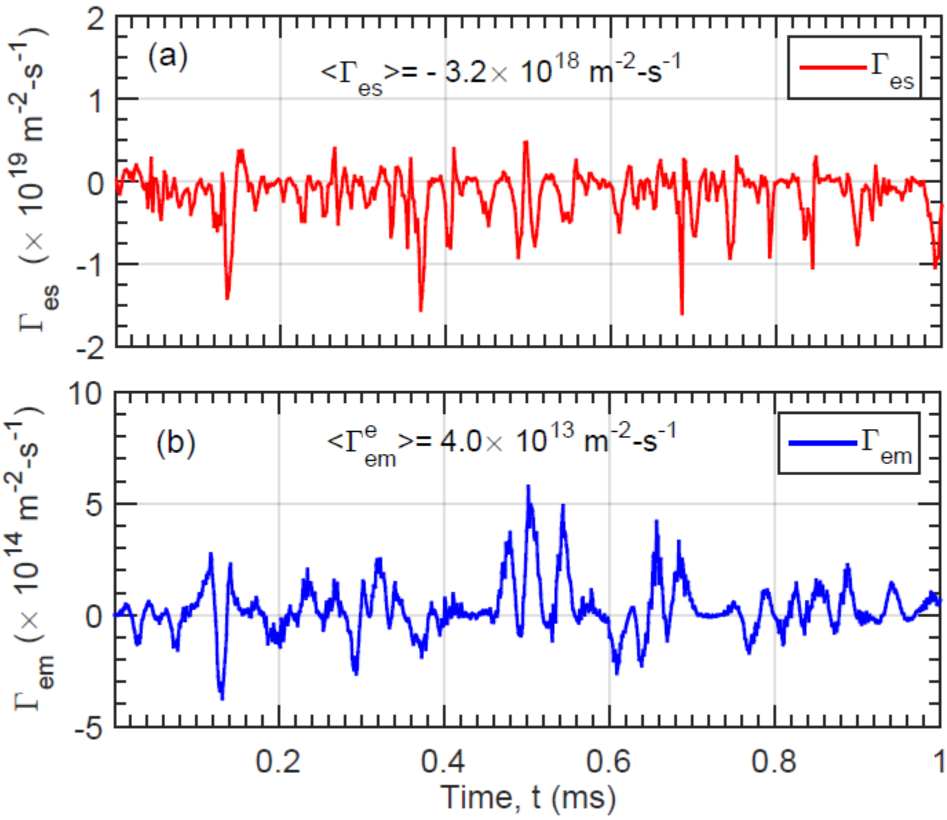

Figure 4.8: The time series of simultaneously measured electrostatic (a) and electromagnetic (b) fluxes in ETG background at x = 30 cm are shown. The typical time-averaged values obtained are $<\Gamma_{es}> = -3.2 \times 10^{18}$ $m^{-2}s^{-1}$ and $<\Gamma_{em}> = 4 \times 10^{13}$ m^{-2} s^{-1}, respectively.

We found that the electromagnetic flux is finite even though as mentioned, it should be zero [91]. This has prompted us to look for the reason that why EM flux is finite in ETG plasma in slab geometry of LVPD.

4.4 Theoretical model and experimental comparison

4.4.1 Quasi-linear theory for electromagnetic particle flux

Electromagnetic electron particle flux is given by,

$$\Gamma_{em}^{e} = -\frac{1}{eB} < \delta J_{\parallel e} \delta B_r > \tag{13}$$

Since the total current perturbation $\delta J_{\parallel}$ is sum of electron and ion current perturbations $\delta J_{\parallel i} + \delta J_{\parallel e} = \delta J_{\parallel}$, the electron flux can be written as

$$\Gamma_{em}^{e} = \frac{1}{eB} < \delta J_{\parallel i} \delta B_x > - \frac{1}{eB} < \delta J_{\parallel} \delta B_x > \tag{14}$$

Then noting $\delta J_{\parallel} = \frac{c}{4\pi} (\nabla \times \delta B)_{z-component}$. Here, the displacement current contribution is ignored as $\frac{1}{c^2}\frac{\partial E}{\partial t}$ scales with $(L/c^2T^2)B$, which is negligible. Here, L is characteristic length, T is characteristic time scale and c is the speed of light .

$$\delta J_{\parallel} \delta B_x = \frac{c}{4\pi} [\frac{\partial}{\partial x}\left(\delta B_x \delta B_y\right) - \delta B_y \frac{\partial}{\partial x} \delta B_x - \frac{\partial}{\partial y}\left(\frac{1}{2}\delta B_x^2\right)]$$

Further using $\nabla . B = 0 \Rightarrow \frac{\partial}{\partial x} \delta B_x = -(\frac{\partial}{\partial y}\delta B_y + \frac{\partial}{\partial z}\delta B_z)$ and hence

$$< \delta J_{\parallel} \delta B_x > = \frac{c}{4\pi} [\frac{\partial}{\partial x}\left(< \delta B_x \delta B_y >\right) + \frac{\partial}{\partial y} < \frac{1}{2}\delta B_y^2 > + < \delta B_y \frac{\partial}{\partial z} \delta B_z >$$

$$- \frac{\partial}{\partial y} < \frac{1}{2}\delta B_x^2 >]$$

The terms $\frac{\partial}{\partial y} < \frac{1}{2}\delta B_y^2 >$ and $\frac{\partial}{\partial y} < \frac{1}{2}\delta B_x^2 >$ vanishes due to poloidal averaging. Poloidal derivative of poloidally averaged quantity is zero. So eventually the expression for flux becomes

$$\Gamma_{em}^{e} = \frac{1}{\mathrm{eB}} < \delta J_{\parallel i} \delta B_x > - \frac{1}{\mathrm{eB}}\frac{c}{4\pi}\frac{\partial}{\partial x} < \delta B_x \delta B_y > - \frac{1}{\mathrm{eB}}\frac{c}{4\pi} < \delta B_y \frac{\partial}{\partial z} \delta B_z > \tag{15}$$

The first term on the right hand side though looks like an electromagnetic ion flux is not a true ion flux. Because of ETG mode frequency scaling, $\Omega_{ci} < \omega \ll \Omega_{ce}$ the ions are unmagnetized and hence the electromagnetic radial ion velocity perturbation is not same as the electron radial velocity perturbation. In fact it can be shown that the radial ion drift velocity perturbation is zero at the leading order. Hence, the actual turbulent ion flux is zero when ions are unmagnetized in ETG turbulence. The first term had been actual ion flux in the frequency range $\omega \ll \Omega_{ci}$ (e.g. ITG turbulence) when ions are magnetized and the ions radial drift velocity fluctuations is given by the same expression as for the electrons to the leading order in Ω_{ci} . Hence the first term represents a pseudo ion flux in ETG turbulence due to its morphological similarity with the actual ion flux in ITG turbulence. The second term is the divergence of Maxwell-stress $<\delta B_x \delta B_y>$ and third term is another correlation between δB_y and $\frac{\partial}{\partial z}\delta B_z$. Equation (8) can also be expressed in terms of the vector potentials as follows

$$\Gamma_{em}^{e} = \frac{1}{eB} < \delta J_{\parallel i} \delta B_x > - \frac{c}{4\pi}\frac{1}{B}\nabla_x < \frac{\partial}{\partial x}\delta A_z \frac{\partial}{\partial z}\delta A_y > + \frac{c}{4\pi}\frac{1}{B} < \vec{\nabla}\delta A_z . \vec{\nabla}\frac{\partial}{\partial z}\delta A_y > \tag{16}$$

This clearly shows that the limit of $\delta A_y \to 0$ the electron flux is purely made of pseudo ion flux due to parallel ion current fluctuations, while the conventional theory by Holland and Diamond et al. [91] produces no flux. This is the new significant improvement in the understanding of electromagnetic flux in ETG turbulence. We next obtained a quasi-linear expression for the ion flux. From the parallel ion momentum equation it is straight forward, to arrive at the following equation for parallel current perturbation. Assuming quasi neutrality, no collisionality and cold ions

$$\delta J_{\parallel,i} = \frac{e^2}{m_i} n \left(\frac{1}{\omega} k_\parallel \delta\phi - \frac{1}{c} A_\parallel\right) - \frac{e}{m_i}\left(-\frac{1}{\omega} k_\parallel \delta p_i + \frac{i}{\omega}\frac{\delta B_r}{B} P'_{i0}\right) \tag{17}$$

Here δp_i is ion pressure perturbation and $\grave{P_{io}}$ is equilibrium ion pressure gradient. Hence electromagnetic pseudo ion flux becomes

$$\Gamma^i_{em} = \frac{1}{eB} < \delta J_{\parallel i} \delta B_r >$$

$$= \sum_{\vec{k}} \left[\frac{e}{m_i B} n \left(\frac{1}{\omega} k_\parallel \delta\phi - \frac{1}{c} A_\parallel\right) - \frac{1}{m_i B}\left(-\frac{1}{\omega} k_\parallel \delta p_i + \frac{i}{\omega}\frac{\delta B_r}{B} P'_{i0}\right)\right](-ik_y A^*_\parallel)$$

$$=$$

$$\sum_{\vec{k}} \left[\frac{e}{m_i B} n \left(-i\frac{1}{\omega} k_\parallel k_y \delta\phi A^*_\parallel + i\frac{1}{c} k_y \left|A_\parallel\right|^2\right) - \frac{1}{m_i B}\left(i\frac{1}{\omega} k_\parallel k_y \delta p_i A^*_\parallel + i\frac{1}{\omega} k_y^2 \frac{1}{B}\left|A_\parallel\right|^2 P'_{i0}\right)\right]$$

$$= \sum_{\vec{k}} \frac{\beta_e}{2}\frac{e}{m_i B} n \frac{k_\parallel k_y}{|\omega|^2}\left(-\omega_r Im(R_A) + \gamma Real(R_A)\right)|\delta\phi|^2 - \sum_{\vec{k}} \frac{1}{m_i B}\left(i\frac{1}{\omega} k_\parallel k_y \delta p_i A^*_\parallel + \frac{\gamma}{|\omega|^2} k_y^2 \frac{1}{B}\left|A_\parallel\right|^2 P'_{io}\right)$$

$$\Gamma^{\mathrm{i}}_{\mathrm{em}} = \Gamma^{\mathrm{i}}{}_{em1} + \Gamma^{\mathrm{i}}{}_{em2} + \Gamma^{\mathrm{i}}{}_{em3} (say) \tag{18}$$

where the linear electromagnetic response function is given by

$$R_A = \frac{k_z \omega - \frac{5\tau_e \omega}{3} - \left(\eta_e - \frac{2}{3}\right) k_y}{\omega\left(\frac{\beta_e}{2} + k_\perp^2\right)\omega - \frac{\beta_e}{2} K k_y}$$

It is more enlightening to analyze the different pieces of the flux separately

$$\Gamma_{em1} = \sum_{\vec{k}} \frac{\beta_e}{2}\frac{m_e}{m_i} n c_e \frac{k_\parallel c_e k_y \rho_e}{|\omega|^2}\left(-\omega_r Im(R_A) + \gamma Real(R_A)\right)\left|\frac{e\delta\phi}{T_e}\right|^2 \tag{19}$$

$$\Gamma_{em2} = -\sum_{\vec{k}} \tau_i \frac{\beta_e}{2}\frac{m_e}{m_i} n c_e i \frac{1}{\omega} k_{\parallel} c_e k_y \rho_e R_A^* \left(\frac{\delta n}{n_0} + \frac{\delta T_i}{T_i}\right)\left(\frac{e\delta\phi^*}{T_{e0}}\right)$$

$$= \sum_{\vec{k}} \frac{\beta_e}{2}\frac{m_e}{m_i} n c_e \frac{k_{\parallel} c_e k_y \rho_e}{|\omega|^2} [(\omega_r - \gamma\delta_k) Im(R_A) \tag{20}$$

$$- (\gamma + \omega_r \delta_k) Real(R_A)] \left|\frac{e\delta\phi}{T_e}\right|^2 + \alpha\tau_i \frac{\delta T_i}{T_{i0}} \frac{e\delta\phi^*}{T_{eo}}$$

Here, we used the non-Boltzmannian ion response coming from the resonance of the ETG mode with the ions [30,92]

$$\frac{\delta n_i}{n_0} = -\tau_e (1 + i\delta_k) \frac{e\delta\phi_k}{T_{e0}} \tag{21}$$

Where the non-adiabatic parameter δ_k is given by $\delta_k = \sqrt{\pi}\frac{\omega}{k_\perp c_i} \exp - \left(\frac{\omega}{k_\perp c_i}\right)^2$.

The third piece is

$$\Gamma_{em3} = \sum_{k} \tau_i \left(\frac{\beta_e}{2}\right)^2 \frac{m_e}{m_i} n\, c_e \frac{\gamma c_e L_{pi}^2}{|\omega|^2}\, k_y^2 \rho_e^2 |R_A|^2 \left|\frac{e\delta\phi}{T_{eo}}\right|^2 \tag{22}$$

Here L_{pi}^{-1} is pressure gradient scale length. It is noticeable that Γ_{em3} is of higher order in $\frac{\beta_e}{2}$ as compared to Γ_{em1} and Γ_{em2}. Assuming $\frac{\delta T_i}{T_{i0}} = 0$ and noting that part of Γ_{em2} cancels with Γ_{em1}, we get the total radial EM flux as

$$\Gamma_{em}^i = -\frac{\beta_e}{2}\frac{m_e}{m_i} n_0 c_e \sum_{\vec{k}} \frac{k_{\parallel} c_e k_y \rho_e}{|\omega|^2} \delta_k \left[\left(\gamma Im(R_A) + \omega_r Real(R_A)\right)\right] \left|\frac{e\delta\phi_k}{T_{e0}}\right|^2 + 0\left(\left(\frac{\beta_e}{2}\right)^2 \frac{m_e}{m_i}\right) \tag{23}$$

Since the expression for electrostatic electron flux Γ_{es} from Ref. [30].

$$\Gamma_{es} =< \delta n_e \delta v_{E\times B} >= \sum_{k} n_o c_e \tau_e \delta_k k_y \rho_e \left|\frac{e\delta\phi_k}{T_{eo}}\right|^2 \tag{24}$$

For the typical $k_z = 0.1$, $\omega = 0.1(1+i)$, $k_y = 0.1$, $\tau_e = 10$, $\eta_e = 3$, $\beta = 0.2$, the ratio of electromagnetic to electrostatic flux yields

$$\frac{\Gamma_{em}^{i}}{\Gamma_{es}} \approx \frac{\beta_e}{2}\frac{m_e}{m_i}\frac{1}{\tau_e} \times (10 \sim 100) = 0.08 \times \frac{1}{40 \times 1836} \times \frac{1}{\tau_e}(10 \sim 100) \approx 10^{-5} \tag{25}$$

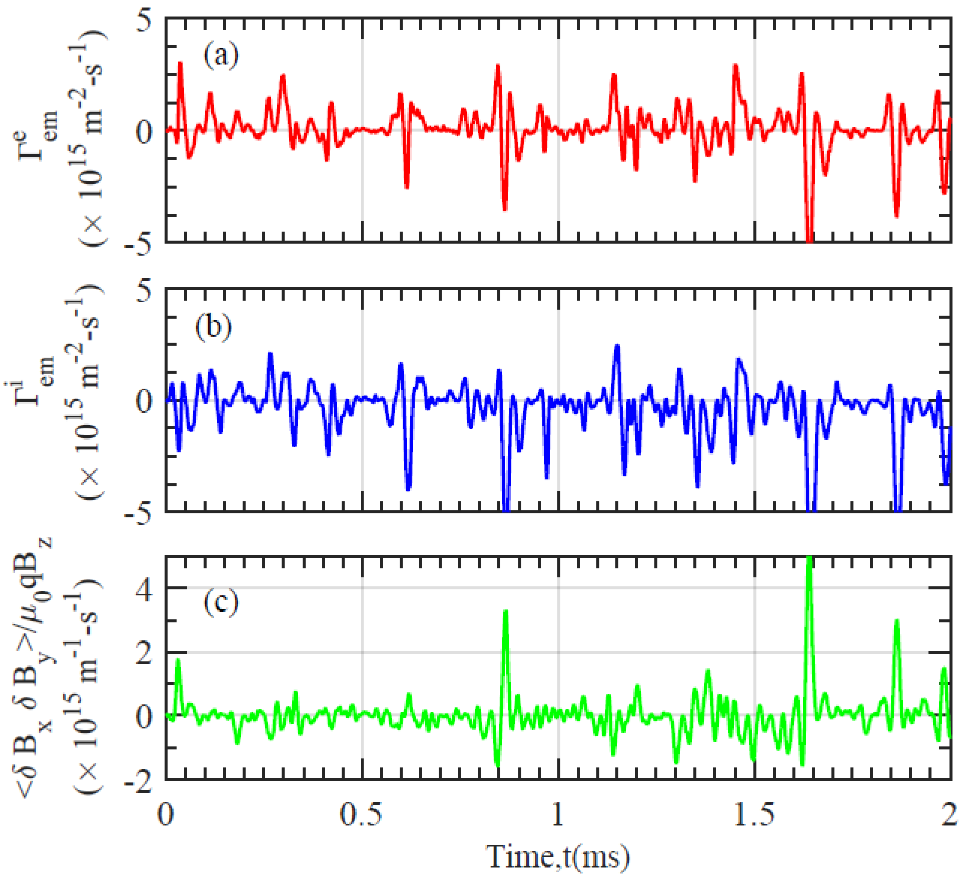

Figure 4.9. Electromagnetic particle flux is shown due to parallel (a) electron streaming, Γ^{e}_{em}, (b) ion streaming, Γ^{i}_{em} and (c) time variation of Maxwell stress at x=30 cm. The average values of the flux components due to parallel electron and ion currents are 4.0×10^{13} m^{-2} s^{-1} and -1.2×10^{14} m^{-2} s^{-1} respectively and the Maxwell Stress contribution is about $- 3.2 \times 10^{13}$ m^{-1} s^{-1}.

In Figure 4.9, we have made an attempt to estimate the experimentally observed particle flux due to electron and ion parallel motion. It was observed that the average electron and ion flux contribution differ significantly. This suggested that the electromagnetic flux may have a non-ambipolar nature which can probably leads to the creation of radial charge separation balanced by the sum of divergence of Maxwell –stress, and grad of axial magnetic field fluctuations.

As can be seen from equation (15), the difference in flux produced by electron and ions can be understood by the radial evolution of Maxwell stress.

4.4.2 Radial profiles of ion and electron fluxes and comparison with theoretical values

In Figure 4.10, the electromagnetic fluctuations driven radial electron flux is measured during the steady state period between (6- 8) ms of discharge pulse using the correlated parallel electron and ions current density fluctuations, $\delta J_{\parallel e,i}$ and radial magnetic field fluctuations, δB_x. The contribution to flux due to ion current is compared with the theoretically obtained values. The theoretical values are obtained using the expression

$$\Gamma_{em}^{i} = -\frac{\beta_e}{2}\frac{m_e}{m_i} n_0 c_e \sum_{\vec{k}} \frac{k_\parallel c_e k_y \rho_e}{|\omega|^2} \delta_k [(\gamma Im(R_A) + \omega_r Real(R_A))] \left|\frac{e\delta\phi}{T_{e0}}\right|^2 + 0\left(\left(\frac{\beta_e}{2}\right)^2 \frac{m_e}{m_i}\right)$$

By the use of experimentally measured parameters such as parallel wave number, $|k_\parallel| \sim 0.006\, cm^{-1}$, poloidal wave number, $|k_y| \approx 0.15 cm^{-1}$ (from Figure 4.4), local experimental β_e and local fluctuation levels, $\left|\frac{e\delta\phi}{T_e}\right|$, we found that the estimated value of flux agrees well with the experimentally obtained ion current flux.

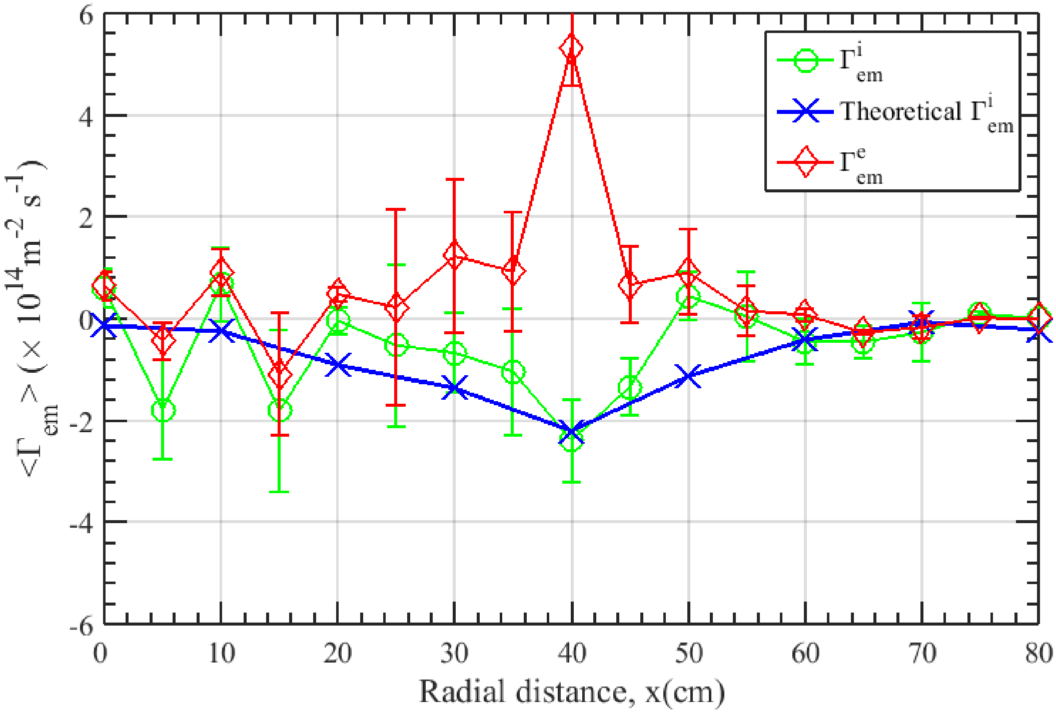

Figure 4.10. Radial electromagnetic particle flux due to parallel electron current, $\Gamma_{\delta J//e,\delta Bx}$, parallel ion streaming current, $\Gamma_{\delta J\|I,\delta Bx}$ and numerical values obtained from theoretical the expression for Γ^i_{em}.

4.5 Summary and conclusion

We studied electromagnetic particle flux due to ETG turbulence in LVPD. The measurement shows that the electromagnetic flux is non-ambipolar leading to the net charge flux. The electromagnetic flux is found to be smaller than the electrostatic flux. A quasilinear theory is proposed to explain the observed flux which convinces that the non-ambipolarity is due to divergence of Maxwell stress $\frac{\partial}{\partial x} < \delta B_x \delta B_y >$ and another correlation $<\delta B_y \frac{\partial}{\partial z} \delta B_z>$. The pseudo ion flux similar to ion flux in morphology had the ions been magnetized. This is because the parallel ion dynamics are little affected by the degree of magnetization of ions. The physical electromagnetic ion flux in ETG turbulence is zero because no radial ion drifts fluctuation due to un-magnetization of ions. Then the overall quasi-neutrality must be maintained by the parallel fluxes. The quasi-linear estimates of the electromagnetic pseudo ion flux due to parallel ion current fluctuation is compared well with measured flux. The complete study of electromagnetic electron flux also requires measurement of divergence of Maxwell-stress which together with the Reynolds stress, $<\delta v_x \delta v_y>$ may be responsible for the $E \times B$ shear layer formation at $x = 40\ cm$ (evident from the peak of the plasma potential in Figure 4.4(c)). This is still an on-going work and will be presented elsewhere.

Chapter 5
Experimental study of total turbulent heat transport

5.1 Introduction

The plasma turbulence is equally responsible for the particle and heat losses in most of the plasma confining system. After knowing the particle flux generation due to ETG turbulence we explore the heat/energy flux in the background of Electron Temperature Gradient (ETG) driven turbulence. The experimental observation and related theoretical discussion will be provided in this chapter for the heat flux.

In the present work, thermal heat conductivity is calculated with the estimated heat flux. For the measurement of heat flux, we designed a triple Langmuir probe for temperature fluctuations in pulsed plasma of LVPD. The cross-phase angle between temperature and potential fluctuations is also measured which differs from 180 degrees. Radial conductive heat flux ($3/2\ n_e < \delta T_e \delta V_x >$) is measured with convective heat flux ($3/2\ T_e <\delta n_e \delta V_x>$) and found radially outward. This is greater than convective heat flux which is radially inward due to radially inward particle flux [30]. The estimated heat flux is compared with the numerically obtained values from slab ETG model equations which are also discussed in this chapter for the ETG region of target plasma ($x \leq 50$ cm). Thermal conductivity is calculated and found to scale quadratically with fluctuation intensity which is what is expected from quasi-linear estimates. All the measurement are presented in this chapter is based on the experimental observation in target plasma of LVPD which approximately 1 m axially away from EEF.

The rest of the chapter is organized as follows: the experimental setup and diagnostics are discussed in section 5.2. The experimental observations on fluctuations and characterization are described in section 5.3. The observation of heat flux, its comparison with numerically obtained values and justification are given in section 5.4. Finally, the summary and conclusions of this chapter is discussed in section 5.5.

5.2 Experimental setup and diagnostics

The experiments for energy flux measurement are carried out in the target region of LVPD. Details of plasma confinement system, plasma source, EEF, and various other subsystems are already described in Chapter 2.

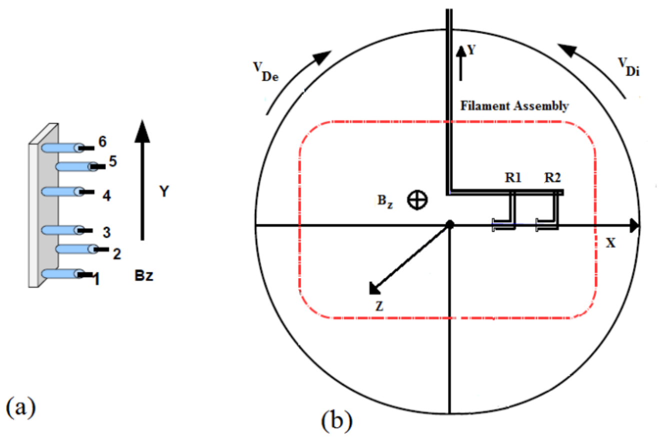

Figure 5.1.(a) Assembly of six single Langmuir probe for simultaneous measurement of electron temperature, δT_e floating potential, $\delta \phi_f$ and plasma density fluctuations, δn_e (b) Schematic of the direction of drift velocities in LVPD and radial positing of the probe in the target region (front view) for simultaneous measurements of particle and heat flux.

The measurement of various plasma parameters (electron temperature, T_e, plasma density, n_e, floating potential, φ_f and plasma potential, φ_p) are determined by using conventional cylindrical Langmuir probes (W, Φ = 1 mm and L = 5 mm) and Centre Tapped Emissive Probe(CTEP) [74]. Specially designed compensated Langmuir probes are used for the measurement of electron temperature by sweeping the probe between -100 V to +20 V over a swept period of 500 μs [88]. All these probes are mounted at different axial locations in the ETG region on radially movable probe shafts. The mean electron temperature obtained with a single Langmuir probe (SLP) is compared with the triple Langmuir probe (TLP) diagnostic for real time temperature fluctuations measurements [63]. Plasma potential is measured with the use of centre tapped emissive probe (CTEP) [74]. The mean values of plasma parameters and fluctuations are obtained for the steady state plasma region of (4 – 9.2) ms from the onset of plasma discharge.

The schematic for TLP assembly is shown Figure 5.2(a) and its electrical scheme is presented in Figure 5.2(b). A brief description of TLP diagnostic is discussed in Chapter 2.

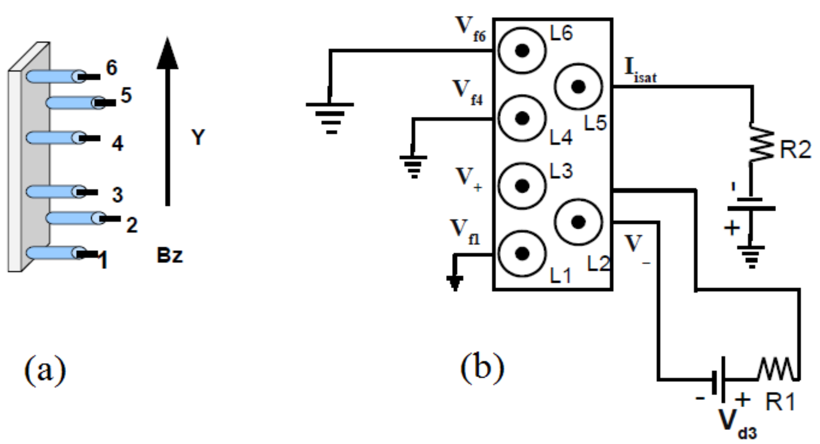

Figure 5.2. (a) Schematic of six probe assembly for simultaneous measurement of parameters to estimate particle, Γ_{es} and heat flux, q. Probes are arranged at vertices of two consecutive equilateral triangles (b) the electrical scheme followed for measurement of fluxes.

The salient features of TLP diagnostic are, 1) bandwidth 300 kHz, 2) galvanic isolation 250 V, 3) input impedance for voltage measurement exceeding ~10 $M\Omega$ and current measurement with shunt resistor ~ 300 Ω. The probe assembly shown in Figure 5.2, consists of two sets of three Langmuir probes. Each probe is cylindrical in shape and has a dimension ($W, \varphi = 1$mm$, L = 8$mm). First vertical array has 4 numbers of probes (L1, L3, L4, and L6) with separation, $\Delta y = 15$ mm, while second vertical array consists 2 probes(L2 & L4), vertically displaced, $\Delta y = 30$ mm. Axially the two arrays are separated byΔx~15mm. Probes numbering, L1, L2, L3 and L4 are used for electron temperature measurement. Probes are placed at different magnetic field lines and are transverse to the ambient magnetic field so as to avoid the influence of shadowing effect and magnetic field. The probe array assembly is mounted on a radially movable probe drive [70]. The TLP measurements are calibrated against single Langmuir probe measurements and TLP configuration is confirmed by obtaining I/V characteristics of double probe. The pair of L2 and L3 are used in double probe configuration and are fed power by floating battery-based power supply. It has characteristic features viz., variable voltage, negligible capacitance with respect to ground. The ion saturation current is obtained across 500-ohm resistance using a floating, battery biased current measurement circuitry. The poloidally separated probes L1, L4, and L6 are used to measure floating potential. The potential (V_+ of positively biased probe L3 is also measured. The Langmuir probe L5 measures ion saturation current and is biased at a high negative potential with respect to plasma potential to estimate mean and fluctuations density of the plasma. By choosing a suitable value of bias voltage between L2 and L3, one calculates electron temperature, T_e by using expression $T_e = (V_+ - V_f)/\text{Log}\,(2)$, where V_f is the average value of V_{f1} and V_{f4} .

The probe arrangement ensures that the parameters V_f, I_{isat} are measured by probes placed in close vicinity of each other to avoid the phase delay error. For the investigation of fluctuations, data is recorded during the steady state of plasma current. The fluctuating E_θ can be obtained by poloidally separated probes using $\tilde{E}_\theta = -\partial\,\phi/\partial\,y$ where δV_r is derived from $\delta E_\theta \times B$ drift. The radial velocity fluctuations are responsible for conductive ($n_o < \delta T_e \delta V_r >$) and convective heat flux ($T_e < \delta n_e \delta V_r >$) having a correlation to temperature and density fluctuations respectively. The fluctuations in electron temperature, δT_e, density, δn_e and potential, $\delta\phi$ are measured for the complete duration of plasma evolution 10 ms with a sampling rate of 1 MS$/s$.

The data is acquired with a 12bit digitizer based PXI data acquisition system. An ensemble of 100 shots from the steady state window is used for carrying out spectral analysis viz., correlation, coherency, phase, power spectra, and joint wave number frequency spectrum, S(k,w) [71,93].

5.3 Experimental observations and fluctuation characterization

Typical time profiles of plasma parameters in the target region for activated EEF are shown in Figure 5.3. The plasma discharge pulse (Figure 5.3b) is accommodated within the pulse duration of the EEF current (Figure 5.3a). The ion saturation current (Figure 5.3c) do not show fluctuations in the early phase of the discharge but after $\sim 1ms$, fluctuations start appearing and are seen stabilizing after 6 ms from the onset of discharge. A similar trend in fluctuations is seen for other plasma parameters such as floating potential and electron temperature. The floating potential,V_f is measured using Langmuir probe at high impedance ($\geq 10\ M\Omega$) and is shown in Figure 5.3(d). The evolution of mean electron temperature T_e is recorded using triple Langmuir probe (Figure 5.3e). The fluctuation and mean part of these plasma parameters are measured for the steady state plasma duration for further analysis to characterize the mean profile and nature of plasma turbulence.

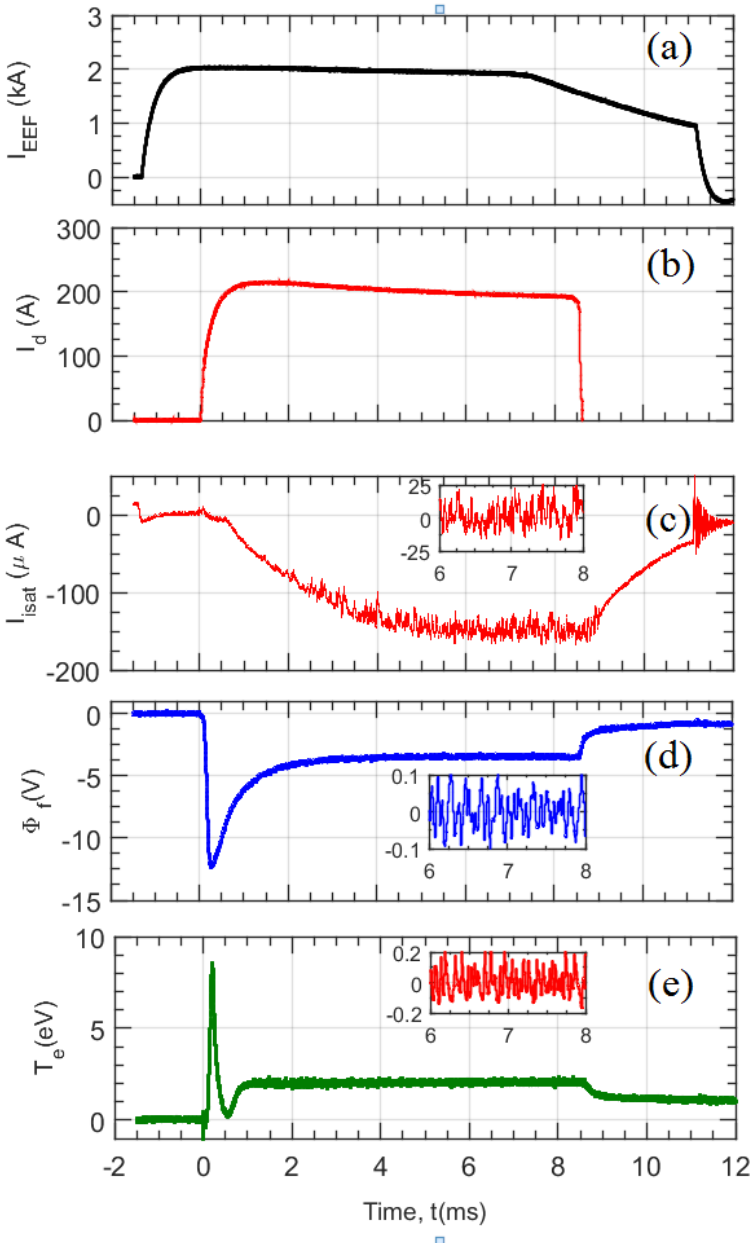

Figure 5.3. Time series traces of (a) filter current, I_{EEF}, (b) discharge currents, I_d, (c) ion saturation current, Iisat, (d) the floating potential, ϕ_f, and (e) the electron temperature, T_e in the target plasma. The temporal evolution of electron temperature and its fluctuations using TLP are shown in (e). The inset of (c), (d) and (e) shows the ac coupled part for steady-state plasma (6 -8 ms).

We revisited the ETG turbulence conditions and measured profiles of plasma density, and electron temperature in the target region of LVPD. The plasma potential remain uniform in the region thus produces, $E_x \approx 0$. Radial profiles of plasma density and electron temperature are shown in Figure 5.4. The nature of fluctuations is characterized by the joint wave number- frequency spectra, S(k,w). The obtained S(k,w) and radial profiles of plasma density and electron temperature satisfies wavelength $k_\perp \rho_e \le 1$ and $k_\perp \rho_i > 1$, and frequency ordering $\omega_{ci} < \omega \ll \omega_{ce}$ where ω_{ci} is ion-cyclotron frequency, ω_{ce} is electron cyclotron frequency and ω is mode frequency. The scale length of density, $L_n = \left(\frac{1}{n}\frac{dn}{dx}\right)^{-1} \approx 300cm$ and electron temperature , $L_{T_e} = \left(\frac{1}{T_e}\frac{dT_e}{dx}\right)^{-1} \approx 55cm$ satisfies the threshold, $\eta_{\mathrm{ETG}} = L_n/L_T > 2/3$ of ETG turbulence in the core region($x \le 45$cm) [24].

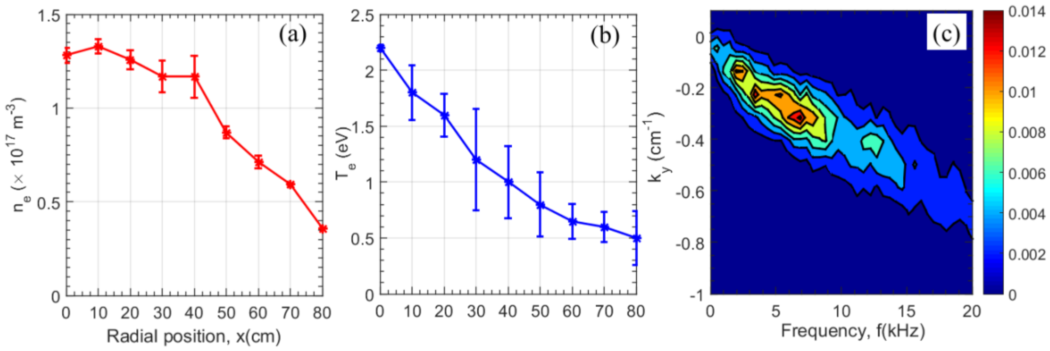

Figure 5.4. Radial profiles of (a) plasma density, n_e , (b) electron temperature, T_e, and (c) the joint wave number –frequency, S(k, f) , where, k_y is the poloidal wave vector.

Figure 5.5 shows the snapshot of typically saturated fluctuations in temperature, floating potential and ion saturation current, δT_e, $\delta\phi$ and δI_{sat} , respectively. Turbulent data is collected for 100 plasma discharges in the core region and concocted for its characterization. Time profile shows in-phase correlation between density and temperature fluctuations and both are found out of phase to the potential fluctuations.

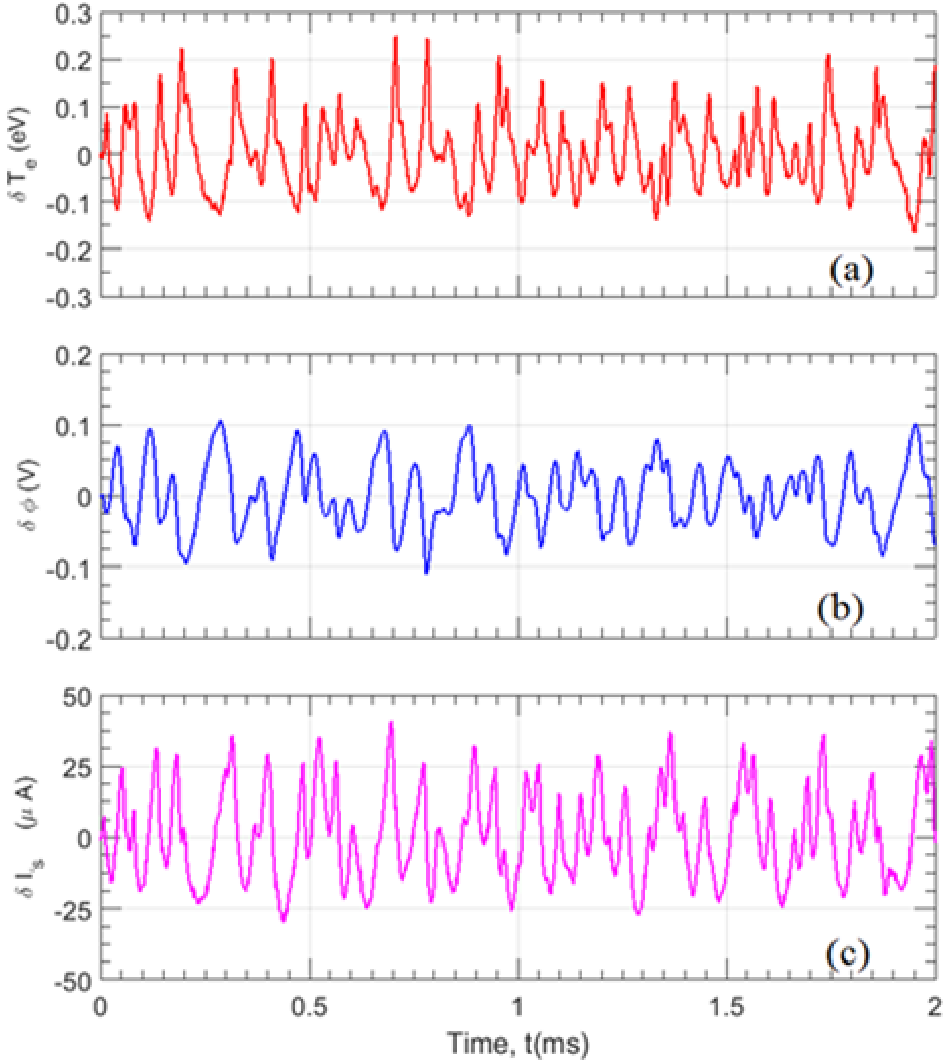

Figure 5.5. The typical fluctuation of (a) electron temperature, δT_e (b) floating potential, $\delta\phi$ and (c) ion-saturation, δI_{isat} at x = 20 cm.

A strong correlation is observed for temperature and density fluctuations with potential fluctuation. Cross-correlation between them is found to be highly negative with correlation coefficients $C_{\delta n_e - \delta\varphi} \sim -0.8$ and $C_{\delta T - \delta\varphi} \sim -0.9$, respectively, as shown in Figure 5.6.

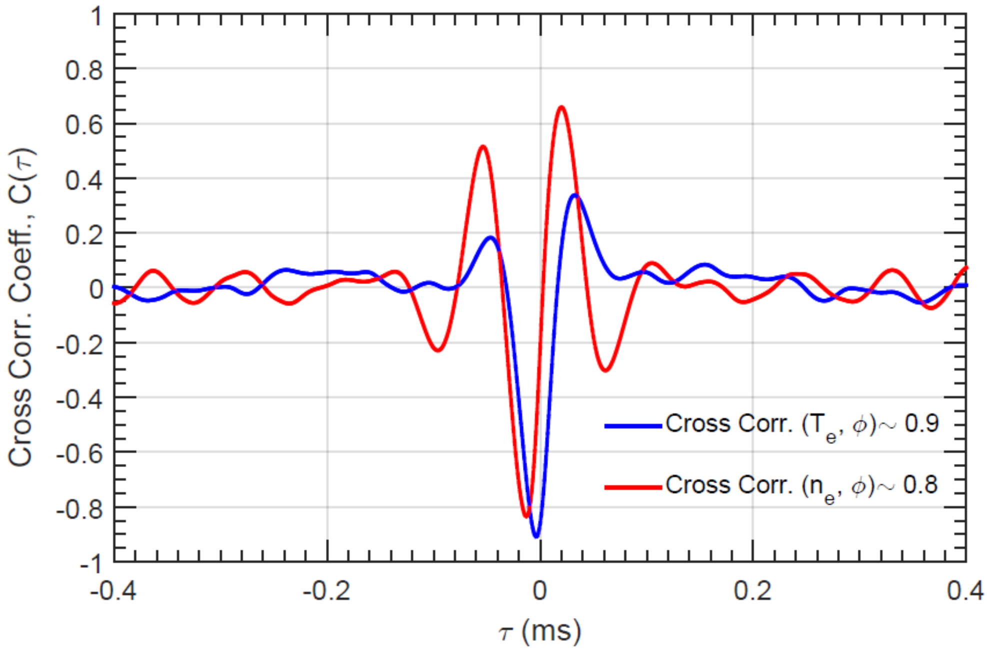

Figure 5.6. Cross-correlation between potential with temperature and density fluctuations is shown. Potential fluctuation is found out of phase to both temperature fluctuations and density fluctuation. The measurement is taken at x = 20 cm.

The typical radial profiles of fluctuations in electron temperature, potential, and ion saturation current are shown in Figure 5.7. The fluctuation levels vary for electron temperature from (2 - 20)%, the potential from (1 - 10)% and ion saturation current fluctuations, which resembles plasma density between (2 - 8)%. The level of fluctuation maximizes at x = 50 cm.

-

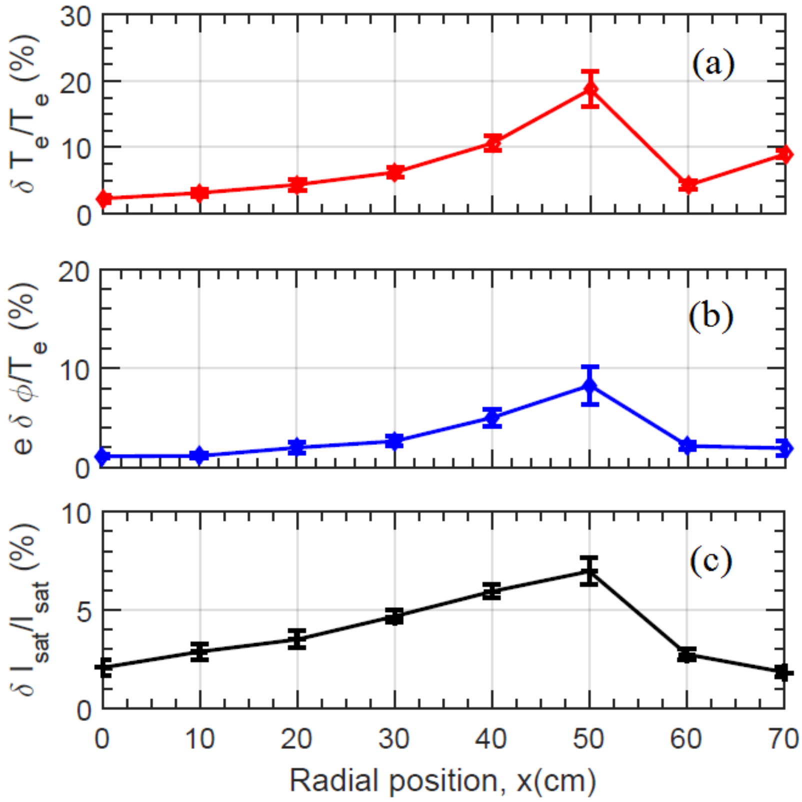

\

Figure 5.7. The radial profile of normalized fluctuations in (a) electron temperature, δTe / Te, (b) floating potential, eδϕ ⁄ Te and (c) ion saturation current, δ I_{isat} / I_{isat}.

The auto-power, phase angle, and coherency spectra are determined following the procedure described by Beall *et al.* [71] and are shown in Figure 5.8. The mode frequency has a broad peak at 1–60 kHz, and the phase angle between the temperature and potential fluctuations is $\sim -150^0$. The coherency is significant (> 0.8) up to 60 kHz between the temperature and potential fluctuations.

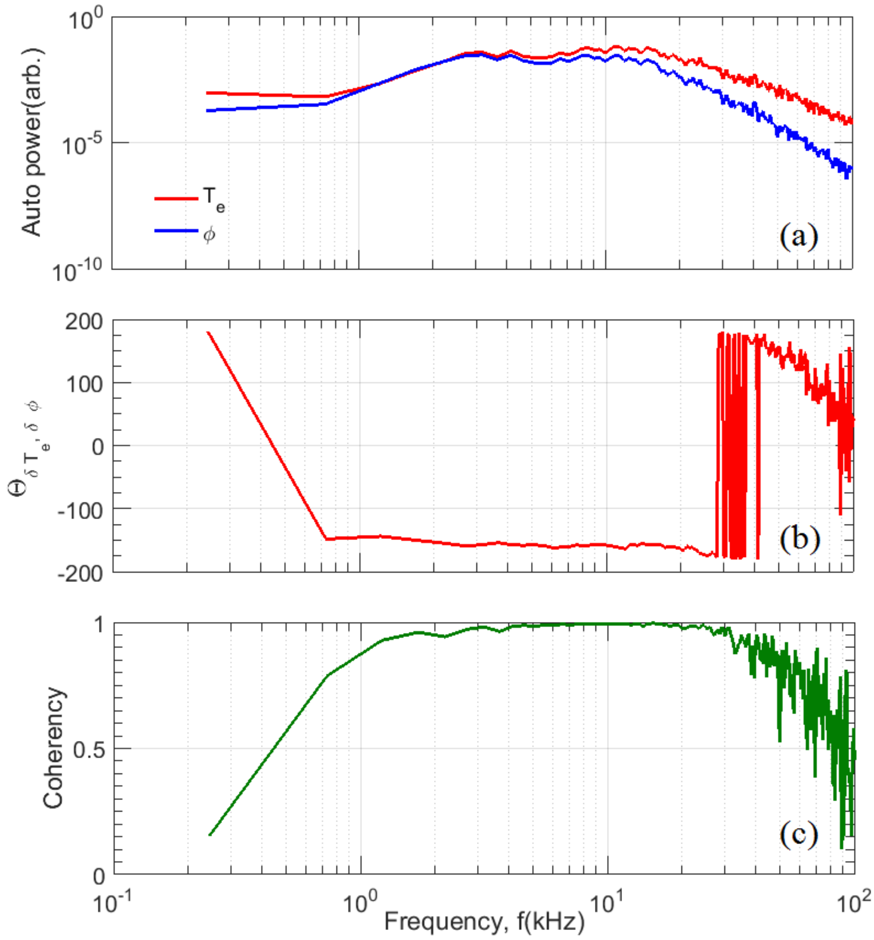

Figure 5.8. The auto power (a), phase angle variation (b), and coherency (c) plot of temperature and potential fluctuations are shown. The spectrum has broad band nature with good coherency between 1-60 kHz. The measurements are carried out at x=30 cm.

This observed phase angle between temperature and potential fluctuations is in good agreement of obtained values from ETG model equations with considerations of ion non-adiabatic response which is better explained in the following section.

5.4 Theoretical model and measurement of heat flux

A theoretical expression formulated for heat flux due to ETG scale fluctuation to compare with experimental measurement of heat flux. The experimental heat flux is calculated with correlated measurement of potential and electron temperature fluctuations.

In LVPD, plasma beta is high (β ~ 0.01-0.4) hence both electrostatic and electromagnetic fluctuations are observed in ETG background [24]. Both ES and EM fluctuations can contribute to total heat flux in the form of convective and conductive heat fluxes. The details for both contributions are explained in the following text.

5.4.1 Electrostatic Heat Flux

The electrostatic electron heat flux is defined as $q_e = \frac{3}{2} < \delta v_r \delta p_e > = \frac{3}{2} n_0 < \delta v_r \delta T_e > + \frac{3}{2} T_{e0} < \delta v_r \delta n_e >$ where the first and second terms are called conductive and convective heat fluxes.

Recall the electron temperature perturbation equation drift reduce for ETG scale

$$\frac{\partial}{\partial t}(T_e - \frac{2}{3} n_e) + (\eta_e - \frac{2}{3}) \nabla_y \varphi + [\varphi, T_e - \frac{2}{3} n_e] = 0$$

which gives the linearized temperature fluctuation as

$$T_{\mathrm{ek}} = (\eta_e - \frac{2}{3}) \frac{k_y}{\omega} \varphi_k + \frac{2}{3} n_{\mathrm{ek}} \tag{26}$$

In dimensional form it reads

$$\frac{\delta T_{\mathrm{ek}}}{T_{e0}} = (\eta_e - \frac{2}{3})\frac{c_e k_y \rho_e}{L_n \omega}\frac{e\delta\varphi_k}{T_{e0}} + \frac{2}{3}\frac{\delta n_{\mathrm{ek}}}{n_0} \tag{27}$$

Using $\frac{\delta n_{\mathrm{ek}}}{n_0} = \frac{\delta n_{\mathrm{ik}}}{n_0} = -\tau_e(A_k + i\delta_k)\frac{e\delta\varphi}{T_{eo}}$ where $A_k$is even in k and $\delta_k$is odd in k, $\tau_e = T_e/T_i$ ratio of electron temperature to ion temperature.

As, $\delta_k = \frac{\sqrt{\pi}\omega}{k_\perp\, V_{thi}}\exp - \frac{\omega^2}{k_\perp^2 V_{thi}^2}$, now using $\delta v_r = -c_e\rho_e \frac{\partial}{\partial y}\frac{e\delta\varphi}{T_{eo}}$ for radial velocity fluctuation yields (R stands for real part in the following)

$$q_{cond,es} = \frac{3}{2} n_o < \delta v_r \delta T_e >$$

$$= \frac{3}{2} n_o c_e T_{eo} \Re \sum_k \left[\left(\eta_e - \frac{2}{3}\right) \frac{c_e \gamma_k (k_y\rho_e)^2}{L_n |\omega_k|^2} \left|\frac{e\delta\phi_k}{T_{eo}}\right|^2 + \frac{2}{3}\frac{\delta n_{ek}}{n_o} i k_y \rho_e \frac{e\delta\phi_k}{T_{eo}} \right]$$

$$= \frac{3}{2} n_o c_e T_{eo} \sum_k \left[\left(\eta_e - \frac{2}{3}\right) \frac{c_e \gamma_k (k_y\rho_e)^2}{L_n |\omega_k|^2} \left|\frac{e\delta\phi_k}{T_{eo}}\right|^2 \right] + T_{eo}\Gamma_e \tag{28}$$

where,

$$\Gamma_e = \sum_k \pi^{\frac{1}{2}} \tau_e n c_e k_y \rho_e \left(\frac{\omega_r}{k_\perp V_{thi}}\right) \exp(-\frac{\omega_r^2}{k_\perp^2 V_{thi}^2}) \left|\frac{e\delta\phi}{T_{eo}}\right|^2$$

Clearly, the usual conductive part also contains a distinct convective flux. Hence we subtract the convective part from above expression and define the conductive flux as

$$q_{cond} = \frac{3}{2} n_o < \delta v_r \delta T_e > - T_{eo}\Gamma_e$$

The total heat flux due to electrostatic fluctuations

$$q_{es} = q_{es}^{cond} + q_{em}^{conv}$$

$$= \frac{3}{2} n_o c_e T_{eo} \sum_k \left[\left(\eta_e - \frac{2}{3}\right) \frac{c_e \gamma_k (k_y \rho_e)^2}{L_n |\omega_k|^2} \left| \frac{e\delta\phi_k}{T_{eo}} \right|^2 \right] + T_{eo}\Gamma_e + \frac{3}{2} T_{e0}$$

$$< \delta v_r \delta n_e >$$

$$= \frac{3}{2} n_o c_e T_{eo} \sum_k \left[\left(\eta_e - \frac{2}{3}\right) \frac{c_e \gamma_k (k_y \rho_e)^2}{L_n |\omega_k|^2} \left| \frac{e\delta\phi_k}{T_{eo}} \right|^2 \right] + \frac{5}{2} T_{eo}\Gamma_e \tag{29}$$

5.4.2 Electromagnetic heat flux

A general expression for electromagnetic heat flux can be written as

$$q_{em} = \frac{3}{2}\frac{1}{B} < TnV_{\parallel e} B_r > = -\frac{3}{2}\frac{1}{eB} < TJ_{\parallel e} B_r >$$

$$= -\frac{3}{2}\frac{T_{eo}}{eB} < \delta J_{\parallel e} \delta B_r > - \frac{3}{2}\frac{T_{eo}}{eB} J_{\parallel eo} < \frac{\delta T_e}{T_{eo}} \delta B_r >$$

$$= \frac{3}{2} T_{eo} \Gamma_e^{em} - \frac{3}{2}\frac{T_{eo}}{eB} J_{\parallel eo} < \frac{\delta T_e}{T_{eo}} \delta B_r >$$

The first term is known and is considered as convective heat flux due to EM flux. The second term is conductive heat flux due to electromagnetic fluctuations and its contribution vanishes and this can be understood in the following manner;

$$< \frac{\delta T_e}{T_{eo}} \delta B_r > = -\Sigma_k i k_y R_A^* R_{T_e} \left| \frac{e\delta\phi_k}{T_{eo}} \right|^2$$

$$= \Sigma_k k_y \left[(R_A^*)^r \left(R_{T_e}\right)^i + (R_A^*)^i \left(R_{T_e}\right)^r \right] \left| \frac{e\delta\phi_k}{T_{eo}} \right| \tag{30}$$

$$= 0$$

Where, $R_A = \frac{k_z \omega - \frac{5\tau_e \omega}{3} - \left(\eta_e - \frac{2}{3}\right) k_y}{\omega\left(\frac{\beta_e}{2} + k_\perp^2\right)\omega - \frac{\beta_e}{2} K k_y}$ and $R_{T_e} = \left[\left(\eta_e - \frac{2}{3}\right)\frac{c_e k_y \rho_e}{L_n \omega} - \frac{2}{3}\tau_e\left(1 + i\frac{\pi^{\frac{1}{2}}\omega}{k_\perp V_{thi}}\exp\left(-\frac{\omega^2}{k_\perp^2 V_{thi}^2}\right)\right)\right]$, R_A & R_{Te} are electromagnetic and temperature response functions, respectively. The above expression vanishes due to k space symmetry properties of R_A and R_T. Hence the only surviving electromagnetic flux in the ETG turbulence is due to the electromagnetic particle flux.

$$q_{em} = \frac{3}{2} T_{eo} \Gamma_e^{em} \tag{31}$$

Thus the total heat flux can be expressed as

$$Q = q_{es} + q_{em} = \frac{3}{2} n_o c_e T_{eo} \sum_k \left[\left(\eta_e - \frac{2}{3}\right) \frac{c_e \gamma_k (k_y \rho_e)^2}{L_n |\omega_k|^2} \left|\frac{e\delta\phi_k}{T_{eo}}\right|^2 \right] + \frac{5}{2} T_{eo} \Gamma_e + \frac{3}{2} T_{eo} \Gamma_e^{em} \tag{32}$$

The significant portion of heat flux comprises mainly of the electrostatic component as the electromagnetic contribution is significantly small ($\frac{\Gamma_{em}}{\Gamma_{es}} = 10^{-5}$).

We compared the experimentally measured phase angle between temperature and potential fluctuations and average values of the heat flux with the theoretically estimated values. Figure 5.9 shows the comparison of phase angle values for a fixed wave-number and frequency of maximum power. The phase angle theoretical plot is derived from Equation (27) by taking into account the ion non-adiabatic response, which can be expressed as ;

$$\widetilde{T_e} = \left[\left(\eta_e - \frac{2}{3}\right)\frac{c_e k_y \rho_e}{L_n \omega} - \frac{2}{3}\tau_e\left(1 + i\frac{\pi^{\frac{1}{2}}\omega}{k_\perp V_{thi}}\exp(-\frac{\omega^2}{k_\perp^2 V_{thi}^2}\right)\right]\tilde{\phi} \quad (33)$$

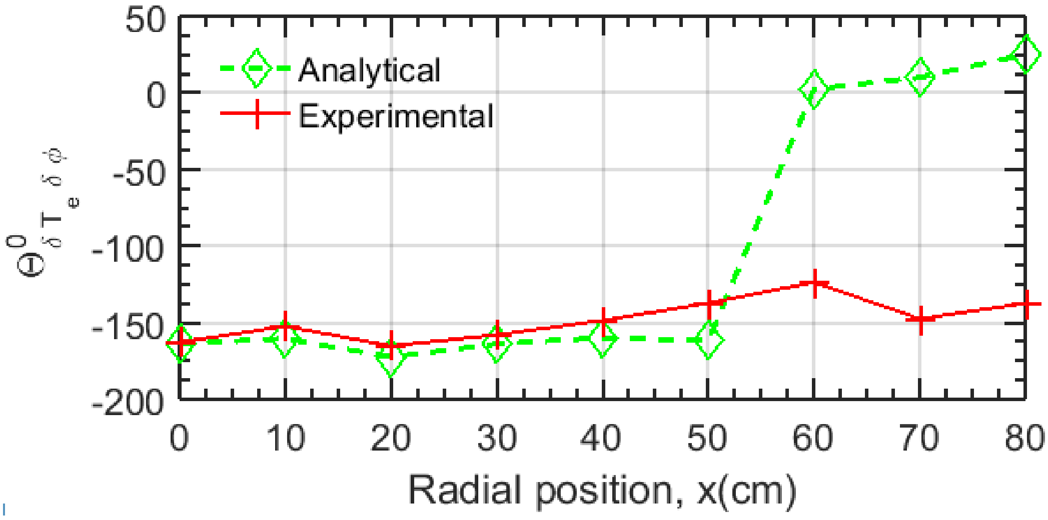

Figure 5.9. The comparison of the experimentally obtained phase angle between temperature fluctuations and potential fluctuations with analytically calculated values.

The experimentally obtained values of $k_\perp (k_\perp \approx k_y)$ and ω are chosen, corresponding to the maximum power of the observed mode in order to estimate the phase angle between the temperature fluctuations and potential fluctuations. A close agreement is observed between theoretical and experimental values in the ETG dominated region ($x \leq 50$ cm). Indirect confirmation of the validity of model equations is envisaged from the fact that in the non ETG region, where they do not hold good, a significant deviation is observed in the phase angle values.

The turbulent heat flux, $q_{cond} = \frac{3}{2} n_o < \delta T_e \delta V_r >$ has been estimated from the real time fluctuations of temperature and potential respectively. The comparison of the observed heat flux, with analytical and numerical estimates are shown in Figure

5.9. The analytical values are obtained by using Equation (28), considering the value of $k_\perp$ ($k_\perp \approx k_y$) and ω for the peak power of the mode directly from the $S(k_\perp,\omega)$. The values of L_n, η_e, ρ_e and c_e for this calculation are derived from the mean equilibrium profiles. An overestimation in the derived values for heat flux cannot be ruled out because of the finite spread in $k_\perp$ and ω values for the observed mode in $s(k_\perp,\omega)$ plot. The amplitude of potential fluctuations is directly taken from the experimental observations.

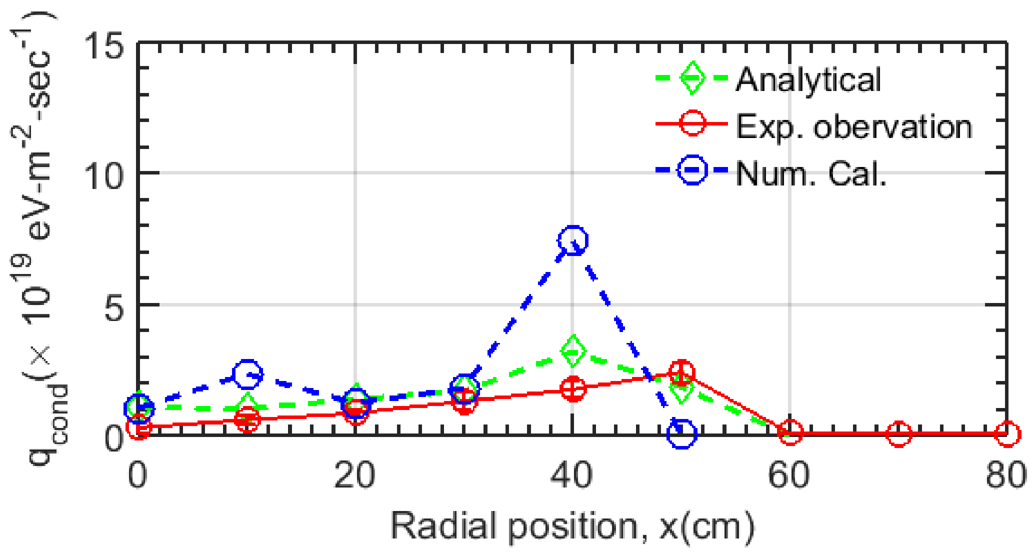

Figure 5.10. Comparison plot of conductive heat flux, q_{cond} for experimental measurement with analytical and numerically estimated values for W-ETG turbulence.

We have also obtained a numerical estimate of heat flux is obtained in the following way. Frequency and growth rates obtained from local W-ETG dispersion relation [24] for experimentally observed wave numbers and local mixing length estimate of intensity fluctuations are used i.e. $\tilde{\phi} \sim \rho_e/L_{T_e}$ to obtain numerical estimates of local flux. The comparison between the analytical and numerical estimates with the experimental observations of heat flux shows good agreement in the ETG dominated core region ($x \leq 50\ cm$) for target plasma of LVPD.

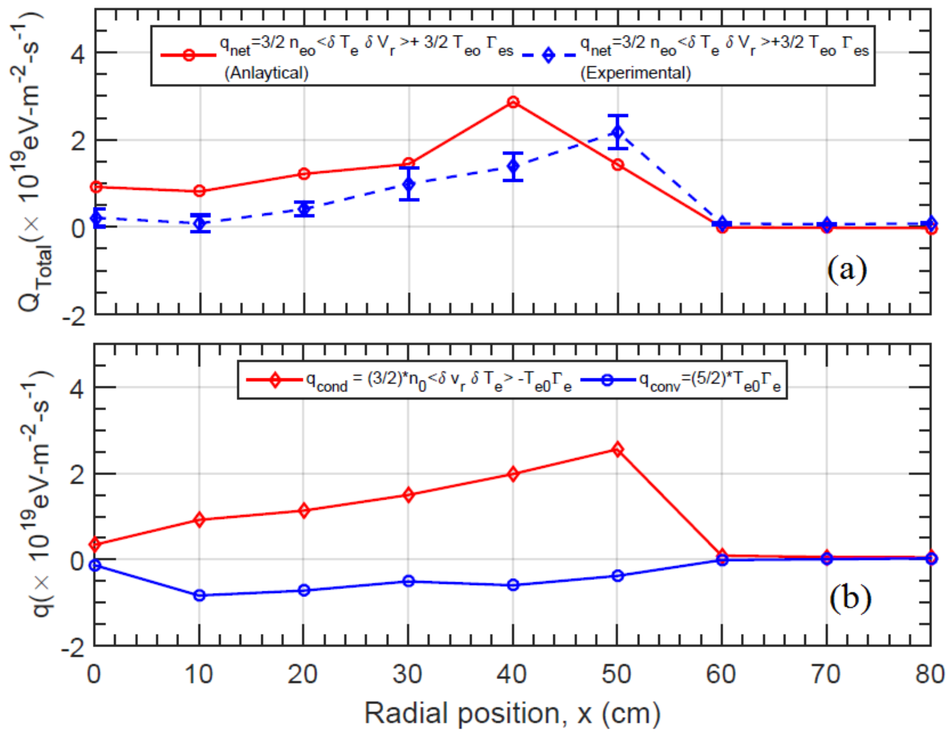

Figure 5.11. Radial variation of the comparison of (a) numerically and experimentally obtained total heat flux and (b) the conductive and convective heat fluxes.

The total heat flux which is the sum of conductive and convective heat fluxes are shown in Figure 5.11 (a). The total flux is found to be positive signifies that ETG driven turbulence can be responsible for heat loss. Figure 5.11(b) shows the conductive and convective heat flux which is estimated from the observed heat flux due to temperature and potential fluctuations and particle flux measurement. Here one can notice that conductive heat flux measured experimentally also have the convective part and which must be subtracted from the measured part so that conductive heat flux, $q_{cond} = \frac{3}{2} n_{eo} < \delta T_e \delta V_r > - T_{eo} \Gamma_e$. Similarly, the convective heat flux is determined by adding particle flux contribution in conductive part to particle flux part which is the reason, $q_{conv} = \frac{5}{2} T_{eo} < \delta n_e \delta V_r >$.

We estimate the electron thermal conductivity at different radial locations over the entire core region of ETG dominated plasma. The electron thermal conductivity is calculated directly from the estimation of the fluctuation induced electron thermal flux.

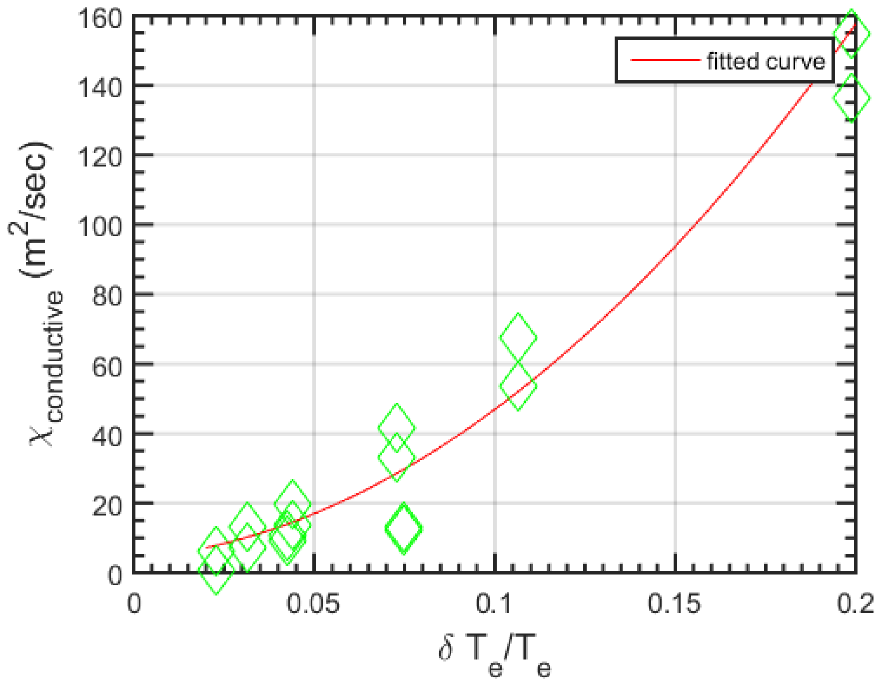

Figure 5.12. Electron thermal conductivity variation with temperature fluctuations present in the system.

The heat conductivity is thus expressed in terms of total heat flux by the expression, $\chi = -\frac{Q}{n_{eo}\frac{dT_e}{dx}}$ where χ is the heat conductivity, Q is the total heat flux and

$\frac{dT_e}{dx}$ is the electron temperature gradient which is shown in Figure 5.12. Observation shows that thermal conductivity exhibits a quadratic dependency for normalized fluctuations between$5\% - 20\%$. This is expected from quasi-linear expressions of heat flux. Here, the temperature fluctuations are considered for different radial locations in the core region. The thermal conductivity maximizes at $x = 50\ cm$ where the temperature fluctuations have a maximum amplitude as shown in Figure 5.7 .

5.5 Summary and conclusion

In summary, we carried out measurement of radial profiles of electrostatic heat flux due to ETG turbulence in LVPD. Though the fluctuations in LVPD are electromagnetic in nature, the electromagnetic particle flux is smaller than the electrostatic flux. The electromagnetic particle flux is measured to be 10^{-5} times of the electrostatic flux. Simple analytical calculations of quasi-linear electromagnetic flux show that the electromagnetic conductive flux is zero [From Equation (30)]. Hence, the measurement of electrostatic heat flux is only considered here.

Excitation of ETG turbulence is validated by measurements of power spectra, frequency scaling, cross phases between density - potential and temperature - potential. Correlation length, time and coherency are also measured to understand the broadband nature of turbulence. Theoretical estimates of frequency and cross phases are in close agreement with the respective experimental values. The cross angle between temperature and potential fluctuations differ from 180 ° resulting in radially outward total heat flux. Conductive and convective heat fluxes are measured. Conductive heat flux is found to be radially outward and is larger than convective heat flux which is radially inward due to radially inward turbulent particle flux [30]. This signifies that the total entropy of the system is always positive definite [81,94]. Thermal conductivity is found to scale quadratically with fluctuation intensity which is expected from quasi-linear estimates.

These laboratory observations may have significant implications for understanding electron transport in fusion devices. Although present-day tokamaks does not have a high beta plasma but may have significance for the alternate magnetic concepts [95–97] as well as these results may be useful during substorm activities [98] taking place in magnetospheric plasma as, during this time, plasma beta is high.

Chapter 6
Conclusion and future scope

6.1 Summary and conclusion

In summary, experimental evidence of Electron Temperature Gradient (ETG) driven plasma turbulence in the finite beta plasma of LVPD (a linear device) and its implications on plasma transport are investigated. This thesis successfully demonstrated the role of ETG turbulence for particle and heat transport induced by small scale fluctuations ($k_{\perp}\rho_e \leq 1$) in the plasma density, potential and electron temperature. The ETG turbulence is excited in the target plasma of LVPD due to the presence of large electron energy filter (EEF). The EEF field helps in making plasma of target region devoid of energetic electrons and creates a gradient in electron temperature. This makes the region of target plasma suitable for carrying out unambiguous investigations on ETG turbulence. To understand the transport due to turbulent fluctuation excited by ETG instability, particle and heat fluxes are measured. Theoretical models are developed to understand the observed fluxes. The comparison of observed particle and heat flux are found consistent with the theoretical study of ETG modes.

Each chapter is summarized as follows:

1. To address various physics problems relevant to plasma transport induced by ETG turbulence study in LVPD, we developed many diagnostics like single Langmuir probe (SLP), double Langmuir probe (DLP), triple Langmuir probe (TLP), directional probe (DP), center tap emissive probe (CTEP), B-dot probe, and microwave interferometry. The SLP is used for the measurement of mean ion-saturation current, floating potential, plasma potential and electron temperature, DLP is used to measure mean electron temperature, TLP is developed for mean electron temperature and its fluctuation measurement, DPs are used for the measurement of parallel ion and electron current fluctuations, CTEP is used for mean and fluctuating plasma potential measurement, 3-axis B-dot probe is used to measure all three components of magnetic field fluctuations and microwave-interferometry diagnostics are used to measure chord average plasma density. A 40 channel PXI based large data acquisition system with the capability of maximum sampling rate ~ 250 MS/s, and record length ~ 256 MS is configured. This data acquisition system has a multiple channel data acquisition facility in a single plasma discharge. Moreover, the manual movement of probe shafts is automatized by controlled motors interfaced by LabVIEW in LVPD for radial measurement of different diagnostics. This helped in obtaining error-free data due to positional inaccuracy introduced by a manual intervention of probe shafts.

2. The excitation conditions and characteristic features on ETG scale fluctuations are revisited and electrostatic fluctuation induced particle flux is measured. Our observations in the form of radially inward particle flux, highlights analogy to the particle pinch scenario as reported in tokamaks [80,99]. Detailed investigations are carried out for identifying the nature of electrostatic particle flux. The equilibrium

electron density and temperature profiles are also measured which show a centrally peaked density profile. Unlike in tokamaks where the particle fuelling is done at the edge (gas puffing), the plasma source in LVPD comprises of heated tungsten filaments arranged in the periphery of a rectangular arrangement located coaxially at one end of the device. Since the axial plasma diffusion is much faster than the transverse diffusion, the plasma formed at one axial end spreads rapidly along the field lines and hence the effective particle source can be thought to be axially elongated and slightly inside the radial edge. The high central density (w.r.t. near boundary) is observed which is consistent with the observation of inward turbulent particle transport i.e., a particle pinch. We noticed observation of particle transport are consistent with the theoretical predictions developed by considering the role of ion non-adiabatic response in ETG model equations [30].

3. In LVPD, strong coupling between density and magnetic field fluctuations is observed and it is predicted to be due to the existing finite plasma beta ($\beta = nkT_e/(B^2/2\mu_o)$ conditions, i.e. $0.01 \leq \beta \leq 0.4$. This suggests that the role of magnetic fluctuations in particle flux estimations need to be accounted for. For meeting this requirement, a specially designed probe array is developed, which accommodates a 3-axis B-dot probe and a pair of closely separated directional probes to measure the magnetic field fluctuation along with parallel electron and ion current fluctuations, simultaneously. We observed a finite electromagnetic (EM) flux in LVPD, in contrast to theoretical predictions of the electromagnetic particle flux in ETG background is to be zero. The reason for this contradiction arises from the assumption made in conventional ETG theory, the total current $J_{\parallel}$ is only due to the parallel electron current $J_{\parallel,e}$ and contribution from the parallel ion current $J_{\parallel,i}$ is ignored. The observation of finite electromagnetic (EM) particle

flux in LVPD has prompted us to work upon the development of a new theoretical model for ETG turbulence by taking into account the motion of ions in a parallel direction. Observed electromagnetic particle flux is found agreeing well to the estimated flux values derived from the developed theoretical model for ETG turbulence induced electromagnetic flux which is developed by considering ion parallel dynamics [82].

4. We have developed a Triple Langmuir Probe (TLP) diagnostic for electron temperature fluctuation measurement which is required to estimate energy flux produced by ETG scale fluctuation in LVPD. The development of TLP diagnostic includes the construction of a floating battery based ramp power supply and measurement circuitry. This TLP diagnostic is used for simultaneous measurement of mean values of electron temperature (T_e), floating potential (ϕ_f), plasma potential (ϕ_p) and their respective fluctuations. The TLP diagnostic offers a frequency response of $\leq$ 300 kHz at 3dB down values. We estimated the conductive and convective heat flux transport by simultaneous measurement of temperature, density, and potential fluctuations. The estimated conductive heat flux is found to be radially outward in contrast to convective heat transport (which arises due to inward particle transport). We compared experimentally estimated conductive heat flux with analytical expression derived from ETG model equations. The analytical heat flux values are obtained from the ETG model equation using both experimental and numerical plasma parameters. These are individually compared with experimental measurement of heat flux which shows a close agreement between them separately in the core plasma region where ETG conditions are satisfied.

6.2 Future scope

The thesis work can be extended for the following research work;

1. The work on plasma transport on ETG turbulence can be extended in the future towards understanding features like identifying the threshold of ETG turbulence in laboratory plasma and its effects on plasma transport by controlling the threshold conditions [100].

2. Saturation of the ETG turbulence is one of the important problems in various devices. This problem can be persuaded in LVPD plasma if ETG conditions are produced at higher confining magnetic field. In the present operating scenario, ion frequency falls within the range of instrumentation operating frequency and its harmonics hence unambiguous measurement of the same is not possible. On the other hand, in higher magnetic fields, these frequencies exceed the instrumentation frequency and thus facilitate accurate measurements. This may allow investigations possible on the coupling of ETG mode to other modes [101,102].

3. Based on the outcome of EM turbulence induced particle transport in LVPD, investigations can also be planned for exploring the interplay between the potential structures and stochastic magnetic fields [91,103].

4. The energy transport investigations have provided a domain where controlled investigations on decoupling between the potential and temperature fluctuations can be explored.
5. As envisaged in tokamaks, ETG turbulence can lead to the generation of intrinsic currents. This problem is not explored yet and can be an extremely important problem to study in current less plasma devices like LVPD.

6. Investigations can be expanded further on the measurement of long scale modes namely, zonal field (small scale dynamo or zonal current), electrostatic streamer as well as a magnetic streamer and zonal flows in the background of short scale ETG turbulence in LVPD plasma. The detailed investigations on the formation of nonlinear structures over the full cross-section of LVPD plasma may require specially designed probe drive system, which allows the least perturbation to plasma during motion of diagnostics. We believe that a rotatable probe drive system may be the best solution for this. Investigations of this nature can explain better the physics of some of these nonlinear phenomenon's. This work can be further expanded for understanding the role of magnetic shear in the formation of these structures and their effect on plasma transport.

7. Available literature suggests that sheared electric field and magnetic field shear play a crucial role in controlling particle and thermal transport in plasma. From the future perspective, this can be considered as a physics problem in LVPD where electric and magnetic shears are imposed in LVPD plasma. The electric field and magnetic shear can be generated in plasma by installing the biased poloidal rings within ETG plasma column and by current carrying wire passing through the axis of the plasma column of LVPD [104–106].

8. Understanding the physics of plasma transport behind the development of ETG suitable equilibrium profiles in target plasma by the influence of changing EEF magnetic field configurations is still remain an unexplored problem. This can be explored based on its dependency on correlation with magnetic field geometry, the role of leaking energetic electrons, etc. It would be very interesting to model such plasma using thermal balance equations along with the law of charge and mass conservations.

9. Role of open field lines and the presence of cusped anode plate at the extreme end of the device modify the configuration of open field lines locally from the perspective of sheath dynamics. Effect of the sheath on ETG turbulence in open field lines proposes to be an interesting problem to explore in a laboratory plasma. Especially its influence on the coupling of temperature and potential fluctuations may invite special attention [107].

References

[1] J. D. Lawson, Proc. Phys. Soc. Sect. B **70**, 6 (1957).

[2] J. W. Connor, Plasma Phys. Control. Fusion **37**, 119 (1995).

[3] E. J. Doyle, W. A. Houlberg, Y. Kamada, V. Mukhovatov, T. H. Osborne, A. Polevoi, G. Bateman, J. W. Connor, J. G. Cordey, T. Fujita, X. Garbet, T. S. Hahm, L. D. Horton, A. E. Hubbard, F. Imbeaux, F. Jenko, J. E. Kinsey, Y. Kishimoto, J. Li, T. C. Luce, Y. Martin, M. Ossipenko, V. Parail, A. Peeters, T. L. Rhodes, J. E. Rice, C. M. Roach, V. Rozhansky, F. Ryter, G. Saibene, R. Sartori, A. C. C. Sips, J. A. Snipes, M. Sugihara, E. J. Synakowski, H. Takenaga, T. Takizuka, K. Thomsen, M. R. Wade, and H. R. Wilson, Nucl. Fusion **47**, S18 (2007).

[4] P. C. Liewer, Nucl. Fusion **25**, 543 (1985).

[5] A. J. Wootton, B. A. Carreras, H. Matsumoto, K. McGuire, W. A. Peebles, C. P. Ritz, P. W. Terry, and S. J. Zweben, Phys. Fluids B **2**, 2879 (1990).

[6] B. A. Carreras, C. Hidalgo, E. Sánchez, M. A. Pedrosa, R. Balbín, I. García-Cortés, B. van Milligen, D. E. Newman, and V. E. Lynch, Phys. Plasmas **3**, 2664 (1996).

[7] L. G. Althaus and O. G. Benvenuto, Mon. Not. R. Astron. Soc. **278**, 981 (1996).

[8] T. J. Bogdan, F. Cattaneo, and A. Malagoli, Astrophys. J. **407**, 316 (1993).

[9] G. R. Tynan, A. Fujisawa, and G. McKee, Plasma Phys. Control. Fusion **51**, 113001 (2009).

[10] A. H. Nielsen, H. L. Pécseli, and J. J. Rasmussen, Phys. Scr. **51**, 632 (1995).

[11] A. Fasoli, B. Labit, M. McGrath, S. H. Müller, G. Plyushchev, M. Podestà, and F. M. Poli, Phys. Plasmas **13**, 055902 (2006).

[12] X. Garbet, L. Garzotti, P. Mantica, H. Nordman, M. Valovic, H. Weisen, and C. Angioni, Phys. Rev. Lett. **91**, 035001 (2003).

[13] P. Srivastav, R. Singh, L. M. Awasthi, A. K. Sanyasi, P. K. Srivastava, R. Sugandhi, R. Singh, and P. K. Kaw, Phys. Plasmas **24**, 112115 (2017).

[14] J. A. Krommes and C.-B. Kim, Phys. Fluids **31**, 869 (1988).

[15] J. D. Callen, C. C. Hegna, and A. J. Cole, Nucl. Fusion **53**, 113015 (2013).

[16] F. Castejón, D. Alegre, A. Alonso, J. Alonso, E. Ascasíbar, A. Baciero, A. de Bustos, D. Baiao, J. M. Barcala, E. Blanco, M. Borchardt, J. Botija, S. Cabrera, E. de la Cal, I. Calvo, A. Cappa, R. Carrasco, R. Castro, A. De Castro, G. Catalán, A. A. Chmyga, M. Chamorro, A. Dinklage, L. Eliseev, T. Estrada, F. Fernández-Marina, J. M. Fontdecaba, L. García, I. García-Cortés, R. García-Gómez, J. M. García-Regaña, J. Guasp, R. Hatzky, J. Hernanz, J. Hernández, J. Herranz, C. Hidalgo, E. Hollmann, A. Jiménez-Denche, I. Kirpitchev, R. Kleiber, A. D. Komarov, A. S. Kozachoek, L. Krupnik, F. Lapayese, M. Liniers, B. Liu, D. López-Bruna, A. López-Fraguas, B. López-Miranda, J. López-Razola, U. Losada, E. de la Luna, A. Martín de Aguilera, F. Martín-Díaz, M. Martínez, G. Martín-Gómez, F. Martín-Hernández, A. B. Martín-Rojo, J. Martínez-Fernández, K. J. McCarthy, F. Medina, M. Medrano, L. Melón, A. V. Melnikov, P. Méndez, R. Merino, F. J. Miguel, B. van Milligen, A. Molinero, B. Momo, P. Monreal, R. Moreno, M. Navarro, Y. Narushima, I.

S. Nedzelskiy, M. A. Ochando, J. Olivares, E. Oyarzábal, J. L. de Pablos, L. Pacios, N. Panadero, I. Pastor, M. A. Pedrosa, A. de la Peña, A. Pereira, A. Petrov, S. Petrov, A. B. Portas, E. Poveda, G. A. Rattá, E. Rincón, L. Ríos, C. Rodríguez, B. Rojo, A. Ros, J. Sánchez, M. Sánchez, E. Sánchez, E. Sánchez-Sarabia, K. Sarksian, S. Satake, J. A. Sebastián, C. Silva, E. R. Solano, A. Soleto, B. J. Sun, F. L. Tabarés, D. Tafalla, S. Tallents, A. Tolkachev, J. Vega, G. Velasco, J. L. Velasco, G. Wolfers, M. Yokoyama, and B. Zurro, Nucl. Fusion **57**, 102022 (2017).

[17] W. X. Ding, D. L. Brower, G. Fiksel, D. J. Den Hartog, S. C. Prager, and J. S. Sarff, Phys. Rev. Lett. **103**, 025001 (2009).

[18] W. Horton, H. V. Wong, P. J. Morrison, A. Wurm, J. H. Kim, J. C. Perez, J. Pratt, G. T. Hoang, B. P. LeBlanc, and R. Ball, Nucl. Fusion **45**, 976 (2005).

[19] S. M. Kaye, F. M. Levinton, D. Stutman, K. Tritz, H. Yuh, M. G. Bell, R. E. Bell, C. W. Domier, D. Gates, W. Horton, J. Kim, B. P. LeBlanc, N. C. Luhmann, R. Maingi, E. Mazzucato, J. E. Menard, D. Mikkelsen, D. Mueller, H. Park, G. Rewoldt, S. A. Sabbagh, D. R. Smith, and W. Wang, Nucl. Fusion **47**, 499 (2007).

[20] G. T. Hoang, C. Bourdelle, X. Garbet, G. Giruzzi, T. Aniel, M. Ottaviani, W. Horton, P. Zhu, and R. V. Budny, Phys. Rev. Lett. **87**, 125001 (2001).

[21] R. Singh, V. Tangri, H. Nordman, and J. Weiland, Phys. Plasmas **8**, 4340 (2001).

[22] S. K. Singh, L. M. Awasthi, R. Singh, P. K. Kaw, R. Jha, and S. K. Mattoo, Phys. Plasmas **18**, 102109 (2011).

[23] E. Mazzucato, D. R. Smith, R. E. Bell, S. M. Kaye, J. C. Hosea, B. P. LeBlanc, J. R. Wilson, P. M. Ryan, C. W. Domier, N. C. Luhmann, H. Yuh, W. Lee, and H. Park, Phys. Rev. Lett. **101**, 075001 (2008).

[24] S. K. Mattoo, S. K. Singh, L. M. Awasthi, R. Singh, and P. K. Kaw, Phys. Rev. Lett. **108**, 255007 (2012).

[25] C. Moon, T. Kaneko, and R. Hatakeyama, Phys. Rev. Lett. **111**, 115001 (2013).

[26] S. K. Mattoo, V. P. Anitha, L. M. Awasthi, and G. Ravi, Rev. Sci. Instrum. **72**, 3864 (2001).

[27] S. K. Singh, P. K. Srivastava, L. M. Awasthi, S. K. Mattoo, A. K. Sanyasi, R. Singh, and P. K. Kaw, Rev. Sci. Instrum. **85**, 033507 (2014).

[28] S. K. Singh, L. M. Awasthi, S. K. Mattoo, P. K. Srivastava, R. Singh, and P. K. Kaw, Plasma Phys. Control. Fusion **54**, 124015 (2012).

[29] A. Fasoli, A. Burckel, L. Federspiel, I. Furno, K. Gustafson, D. Iraji, B. Labit, J. Loizu, G. Plyushchev, P. Ricci, C. Theiler, A. Diallo, S. H. Mueller, M. Podestà, and F. Poli, Plasma Phys. Control. Fusion **52**, 124020 (2010).

[30] P. Srivastav, R. Singh, L. M. Awasthi, A. K. Sanyasi, P. K. Srivastava, R. Sugandhi, R. Singh, and P. K. Kaw, Phys. Plasmas **24**, 112115 (2017).

[31] J. Y. Kim and W. Horton, Phys. Fluids B **3**, 1167 (1991).

[32] J. D. Callen, R. J. Groebner, T. H. Osborne, J. M. Canik, L. W. Owen., A. Y. Pankin, T. Rafiq, T. D. Rognlien, and W. M. Stacey, Nucl. Fusion **50**, 064004 (2010).

[33] W. X. Ding, D. L. Brower, D. Craig, B. H. Deng, S. C. Prager, J. S. Sarff, and

V. Svidzinski, Phys. Rev. Lett. **99**, 055004 (2007).

[34] T. D. Rempel, A. F. Almagri, S. Assadi, D. J. Den Hartog, S. A. Hokin, S. C. Prager, J. S. Sarff, W. Shen, K. L. Sidikman, C. W. Spragins, J. C. Sprott, M. R. Stoneking, and E. J. Zita, Phys. Fluids B Plasma Phys. **4**, 2136 (1992).

[35] M. R. Stoneking, S. A. Hokin, S. C. Prager, G. Fiksel, H. Ji, and D. J. Den Hartog, Phys. Rev. Lett. **73**, 549 (1994).

[36] J. D. Callen, Phys. Rev. Lett. **39**, 1540 (1977).

[37] A. B. Rechester and M. N. Rosenbluth, Phys. Rev. Lett. **40**, 38 (1978).

[38] I. H. Hutchinson, M. Malacarne, P. Noonan, and D. Brotherton-Ratcliffe, Nucl. Fusion **24**, 59 (1984).

[39] B. A. Carreras, P. H. Diamond, M. Murakami, J. L. Dunlap, J. D. Bell, H. R. Hicks, J. A. Holmes, E. A. Lazarus, V. K. Paré, P. Similon, C. E. Thomas, and R. M. Wieland, Phys. Rev. Lett. **50**, 503 (1983).

[40] N. Ohyabu, G. L. Jahns, R. D. Stambaugh, and E. J. Strait, Phys. Rev. Lett. **58**, 120 (1987).

[41] M. García-Muñoz, N. Hicks, R. van Voornveld, I. G. J. Classen, R. Bilato, V. Bobkov, M. Bruedgam, H.-U. Fahrbach, V. Igochine, S. Jaemsae, M. Maraschek, and K. Sassenberg, Phys. Rev. Lett. **104**, 185002 (2010).

[42] W. Shen, R. N. Dexter, and S. C. Prager, Phys. Rev. Lett. **68**, 1319 (1992).

[43] C. Holland and P. H. Diamond, Phys. Plasmas **9**, 3857 (2002).

[44] K. H. Burrell, T. N. Carlstrom, E. J. Doyle, D. Finkenthal, P. Gohil, R. J.

Groebner, D. L. Hillis, J. Kim, H. Matsumoto, R. A. Moyer, T. H. Osborne, C. L. Rettig, W. A. Peebles, T. L. Rhodes, H. StJohn, R. D. Stambaugh, M. R. Wade, and J. G. Watkins, Plasma Phys. Control. Fusion **34**, 1859 (1992).

[45] R. R. Parker, M. Greenwald, S. C. Luckhardt, E. S. Marmar, M. Porkolab, and S. M. Wolfe, Nucl. Fusion **25**, 1127 (1985).

[46] P. Guzdar, C. Liu, J. Dong, and Y. Lee, Phys. Rev. Lett. **57**, 2818 (1986).

[47] F. L. Hinton and R. D. Hazeltine, Rev. Mod. Phys. **48**, 239 (1976).

[48] B. Coppi and N. Sharky, Nucl. Fusion **21**, 1363 (1981).

[49] R. Jha, P. . Kaw, S. . Mattoo, C. V. . Rao, Y. . Saxena, and R. Singh, Nucl. Fusion **33**, 1201 (1993).

[50] K. Tanaka, C. Michael, A. L. Sanin, L. N. Vyacheslavov, K. Kawahata, S. Murakami, A. Wakasa, S. Okajima, H. Yamada, M. Shoji, J. Miyazawa, S. Morita, T. Tokuzawa, T. Akiyama, M. Goto, K. Ida, M. Yoshinuma, I. Yamada, M. Yokoyama, S. Masuzaki, T. Morisaki, R. Sakamoto, H. Funaba, S. Inagaki, M. Kobayashi, and A. Komori, Nucl. Fusion **46**, 110 (2006).

[51] S. K. Mattoo, IPR/TR-53 **84**, (1994).

[52] P. K. Srivastava, S. K. Singh, A. K. Sanyasi, L. M. Awasthi, and S. K. Mattoo, Rev. Sci. Instrum. **87**, 073501 (2016).

[53] L. M. Awasthi, G. Ravi, V. P. Anitha, P. K. Srivastava, and S. K. Mattoo, Plasma Sources Sci. Technol. **12**, 158 (2003).

[54] R. Sugandhi, P. K. Srivastava, A. K. Sanyasi, P. Srivastav, L. M. Awasthi, and S. K. Mattoo, Fusion Eng. Des. **115**, 49 (2017).

[55] W. L. Stirling, P. M. Ryan, C. C. Tsai, and K. N. Leung, Rev. Sci. Instrum. **50**, 102 (1979).

[56] K. N. Leung, N. Hershkowitz, and T. Romesser, Phys. Lett. A **53**, 264 (1975).

[57] N. Hershkowitz and T. Intrator, Rev. Sci. Instrum. **52**, 1629 (1981).

[58] R. Limpaecher and K. R. MacKenzie, Rev. Sci. Instrum. **44**, 726 (1973).

[59] S. K. Singh, P. K. Srivastava, L. M. Awasthi, S. K. Mattoo, A. K. Sanyasi, R. Singh, and P. K. Kaw, Rev. Sci. Instrum. **85**, 033507 (2014).

[60] M. Misakian, J. Res. Natl. Inst. Stand. Technol. **105**, 557 (2000).

[61] D. C. Robinson and M. G. Rusbridge, Plasma Phys. **11**, 73 (1969).

[62] E. O. Johnson and L. Malter, Phys. Rev. **80**, 58 (1950).

[63] S. L. Chen and T. Sekiguchi, J. Appl. Phys. **36**, 2363 (1965).

[64] S. Ghosh, K. K. Barada, P. K. Chattopadhyay, J. Ghosh, and D. Bora, Plasma Sources Sci. Technol. **24**, 015017 (2014).

[65] E. T. Everson, P. Pribyl, C. G. Constantin, A. Zylstra, D. Schaeffer, N. L. Kugland, and C. Niemann, Rev. Sci. Instrum. **80**, 113505 (2009).

[66] M. Hudis and L. M. Lidsky, J. Appl. Phys. **41**, 5011 (1970).

[67] B. J. Peterson, J. N. Talmadge, D. T. Anderson, F. S. B. Anderson, and J. L. Shohet, Rev. Sci. Instrum. **65**, 2599 (1994).

[68] P. Balan, R. Schrittwieser, C. Ioniţă, J. A. Cabral, H. F. C. Figueiredo, H. Fernandes, C. Varandas, J. Adámek, M. Hron, J. Stöckel, E. Martines, M. Tichý, and G. Van Oost, Rev. Sci. Instrum. **74**, 1583 (2003).

[69] I. H. Hutchinson, *Principles of Plasma Diagnostics* (Cambridge University Press, Cambridge, 2002).

[70] A. K. Sanyasi, R. Sugandhi, P. K. Srivastava, P. Srivastav, and L. M. Awasthi, Rev. Sci. Instrum. **89**, 055113 (2018).

[71] J. M. Beall, Y. C. Kim, and E. J. Powers, J. Appl. Phys. **53**, 3933 (1982).

[72] K. W. Ehlers and K. N. Leung, Rev. Sci. Instrum. **52**, 1452 (1981).

[73] A. J. T. Holmes, Rev. Sci. Instrum. **53**, 1517 (1982).

[74] A. K. Sanyasi, P. K. Srivastava, and L. M. Awasthi, Meas. Sci. Technol. **28**, 045904 (2017).

[75] A. K. Sanyasi, L. M. Awasthi, S. K. Mattoo, P. K. Srivastava, S. K. Singh, R. Singh, and P. K. Kaw, Phys. Plasmas **20**, 122113 (2013).

[76] M. Endler, H. Niedermeyer, L. Giannone, E. Kolzhauer, A. Rudyj, G. Theimer, and N. Tsois, Nucl. Fusion **35**, 1307 (1995).

[77] R. Jha, A. Das, N. Bisai, P. Kaw, A. Sen, S. Sharma, and P. N. Guzdar, in *AIP Conf. Proc.* (2010), pp. 13–24.

[78] X. Wei, V. Sokolov, and A. K. Sen, Phys. Plasmas **17**, 042108 (2010).

[79] H. Lin, R. D. Bengtson, and C. P. Ritz, Phys. Fluids B Plasma Phys. **1**, 2027 (1989).

[80] R. Singh, H. Jhang, and P. H. Diamond, Phys. Plasmas **20**, 112506 (2013).

[81] W. Horton, Phys. Lett. A **67**, 129 (1978).

[82] P. Srivastav, R. Singh, L. M. Awasthi, A. K. Sanyasi, P. K. Srivastava, R.

Sugandhi, and R. Singh, Plasma Phys. Control. Fusion **61**, 055010 (2019).

[83] R. Dejarnac, J. P. Gunn, J. Stöckel, J. Adámek, J. Brotánková, and C. Ioniþã, Plasma Phys. Control. Fusion **49**, 1791 (2007).

[84] L. M. Awasthi, S. K. Mattoo, R. Jha, R. Singh, and P. K. Kaw, Phys. Plasmas **17**, 042109 (2010).

[85] P. K. Loewenhardt, B. D. Blackwell, and B. Zhang, Rev. Sci. Instrum. **64**, 3334 (1993).

[86] K. Nagaoka, A. Okamoto, S. Yoshimura, and M. Y. Tanaka, J. Phys. Soc. Japan **70**, 131 (2001).

[87] K. S. Chung, Plasma Sources Sci. Technol. **21**, 63001 (2012).

[88] P. K. Srivastava, S. K. Singh, L. M. Awasthi, and S. K. Mattoo, Rev. Sci. Instrum. **83**, 093504 (2012).

[89] R. L. Merlino, Am. J. Phys. **75**, 1078 (2007).

[90] C. A. Biltoft and E. R. Pardyjak, J. Atmos. Ocean. Technol. **26**, 403 (2009).

[91] C. Holland and P. H. Diamond, Phys. Plasmas **9**, 3857 (2002).

[92] R. Singh, H. Nordman, J. Anderson, and J. Weiland, Phys. Plasmas **5**, 3669 (1998).

[93] D. E. Smith, Phys. Fluids **16**, 1373 (1973).

[94] W. Horton, Plasma Phys. **22**, 345 (1980).

[95] S. C. Cowley, P. K. Kaw, R. S. Kelly, and R. M. Kulsrud, Phys. Fluids B **3**, 2066 (1991).

[96] H. A. B. Bodin and A. A. Newton, Nucl. Fusion **20**, 1255 (1980).

[97] O. Motojima, H. Yamada, A. Komori, N. Ohyabu, T. Mutoh, O. Kaneko, K. Kawahata, T. Mito, K. Ida, S. Imagawa, Y. Nagayama, T. Shimozuma, K. Y. Watanabe, S. Masuzaki, J. Miyazawa, T. Morisaki, S. Morita, S. Ohdachi, N. Ohno, K. Saito, S. Sakakibara, Y. Takeiri, N. Tamura, K. Toi, M. Tokitani, M. Yokoyama, M. Yoshinuma, K. Ikeda, A. Isayama, K. Ishii, S. Kubo, S. Murakami, K. Nagasaki, T. Seki, K. Takahata, and H. Takenaga, Nucl. Fusion **47**, S668 (2007).

[98] R. A. Treumann, L. Brostrom, J. LaBelle, and N. Sckopke, J. Geophys. Res. **95**, 19099 (1990).

[99] J. R. Roth, W. M. Krawczonek, E. J. Powers, J. Y. Hong, and Y. C. Kim, Phys. Rev. Lett. **40**, 1450 (1978).

[100] Ö. D. Gürcan and P. H. Diamond, Phys. Plasmas **11**, 4973 (2004).

[101] F. Merz and F. Jenko, Phys. Rev. Lett. **100**, 2 (2008).

[102] V. Sokolov and A. K. Sen, Phys. Rev. Lett. **113**, 095001 (2014).

[103] R. Singh, R. Ganesh, R. Singh, P. Kaw, and A. Sen, Nucl. Fusion **51**, 013002 (2011).

[104] C. P. Ritz, H. Lin, T. L. Rhodes, and A. J. Wootton, Phys. Rev. Lett. **65**, 2543 (1990).

[105] H. Y. Yuh, S. M. Kaye, F. M. Levinton, E. Mazzucato, D. R. Mikkelsen, D. R. Smith, R. E. Bell, J. C. Hosea, B. P. LeBlanc, J. L. Peterson, H. K. Park, and W. Lee, Phys. Rev. Lett. **106**, 055003 (2011).

[106] D. R. Smith, S. M. Kaye, W. Lee, E. Mazzucato, H. K. Park, R. E. Bell, C. W. Domier, B. P. LeBlanc, F. M. Levinton, N. C. Luhmann, J. E. Menard, and H. Yuh, Phys. Rev. Lett. **102**, 225005 (2009).

[107] N. BISAI, R. SINGH, and R. SINGH, J. Plasma Phys. **77**, 733 (2011).